


5-2017

FRET-Based Investigations of the Structure-Function Relationships in the NMDA Receptor

Drew M. Dolino

Follow this and additional works at: https://digitalcommons.library.tmc.edu/utgsbs_dissertations

 Part of the [Biochemistry Commons](#), [Biophysics Commons](#), [Medicine and Health Sciences Commons](#), [Molecular Biology Commons](#), and the [Structural Biology Commons](#)

Recommended Citation

Dolino, Drew M., "FRET-Based Investigations of the Structure-Function Relationships in the NMDA Receptor" (2017). *The University of Texas MD Anderson Cancer Center UTHealth Graduate School of Biomedical Sciences Dissertations and Theses (Open Access)*. 745.
https://digitalcommons.library.tmc.edu/utgsbs_dissertations/745

This Dissertation (PhD) is brought to you for free and open access by the The University of Texas MD Anderson Cancer Center UTHealth Graduate School of Biomedical Sciences at DigitalCommons@TMC. It has been accepted for inclusion in The University of Texas MD Anderson Cancer Center UTHealth Graduate School of Biomedical Sciences Dissertations and Theses (Open Access) by an authorized administrator of DigitalCommons@TMC. For more information, please contact digitalcommons@library.tmc.edu.

FRET-BASED INVESTIGATIONS OF THE STRUCTURE-FUNCTION
RELATIONSHIPS IN THE NMDA RECEPTOR

by

Drew Matthias Dolino, B.S.

APPROVED:

Vasanthi Jayaraman, Ph.D.
Advisory Professor

Jaroslaw Aronowski, M.D, Ph.D.

Alemayehu Gorfe, Ph.D.

Ruth Heidelberger, M.D., Ph.D.

John Spudich, Ph.D.

APPROVED:

Dean, The University of Texas
MD Anderson Cancer Center UTHealth Graduate School of Biomedical Sciences

FRET-BASED INVESTIGATIONS OF THE STRUCTURE-FUNCTION
RELATIONSHIPS IN THE NMDA RECEPTOR

A

DISSERTATION

Presented to the Faculty of

The University of Texas

MD Anderson Cancer Center UTHealth

Graduate School of Biomedical Sciences

in Partial Fulfillment

of the Requirements

for the Degree of

DOCTOR OF PHILOSOPHY

by

Drew Matthias Dolino, B.S.

Houston, Texas

May, 2017

Copyright

Sections of this dissertation were based on previously published research.

- Dolino, D. M., S. S. Ramaswamy, and V. Jayaraman. 2014. Luminescence Resonance Energy Transfer to Study Conformational Changes in Membrane Proteins Expressed in Mammalian Cells. e51895.
 - Copyrights for the written article remain with the authors, but JoVE has been granted the exclusive, royalty-free, perpetual use of the article, regardless of access type.
- Dolino, D. M., D. Cooper, S. Ramaswamy, H. Jaurich, C. F. Landes, and V. Jayaraman. Structural Dynamics of the Glycine-binding Domain of the *N*-Methyl-D-Aspartate Receptor. *Journal of Biological Chemistry*. 2015; 290: 797-804. © the American Society for Biochemistry and Molecular Biology.
 - Permission is automatically granted for authors to reuse their work for a dissertation.
- Dolino, D. M., S. Rezaei Adariani, S. A. Shaikh, V. Jayaraman, and H. Sanabria. Conformational Selection and Submillisecond Dynamics of the Ligand-binding Domain of the *N*-Methyl-D-Aspartate Receptor. *Journal of Biological Chemistry*. 2016; 291: 16175-16185. © the American Society for Biochemistry and Molecular Biology.
 - Permission is automatically granted for authors to reuse their work for a dissertation.

Dedication

For my family, who sacrificed so much, so that I would never want for anything; and who never gave up on me, despite my circuitous path through life.

For my mentor, Vasanthi Jayaraman, who believed in me for some unknown reason, and who pushed me into achieving goals that I otherwise would never have reached.

For the labmates who took me in as a lowly rotation student and taught me how to become a scientist: Swarna Ramaswamy, who showed me the ropes in the lab and gave me the tools to become an independent researcher; Rita Sirrieh, who showed me that one could still have a good time even while spending long hours at the bench; David MacLean, who was a perpetual fount of information and my inspiration as a model scientist; and Garam Lee, who acted as my lab mother, with whom I could joke around but also to whom I could go with scientific questions.

And for the BMB senior students Natoya Peart, Tré O'Brien, and Nick Parchim, who served not only as my student role models, but also as dear friends who kept me sane throughout my early years as a graduate student, who gave a helping hand whenever I had problems both in and out of science, who lent an ear whenever I needed to vent, and who provided a shoulder to cry on whenever things felt too tough.

To all my dedicatees: you have influenced my journey and my formation during my PhD work more than most, and for that I am eternally grateful and dedicate this dissertation to you.

Acknowledgements

In addition to my dedicatees, my progress toward the completion of this dissertation could not have been done without the support of numerous other individuals. Though there are many more people worth acknowledgement than I have space for, those of especial importance are recognized below.

First, I must thank my labmates and fellow students not yet mentioned. Catie, Doug, Sana, and Vlado contributed to the environment that convinced me to join the lab in the first place and continued to make the lab as enjoyable as it has been these past few years. Thuy, Jiandong, Serena, Lihe, Frank, Nandini, and Anupama served as great role models when I first joined the program. Iveth, Kemly, Kaiqi, Hong, and Scott journeyed with me through my PhD with, and I can think of no better group of people to have done so with. For all the younger students and past rotation students who have come through BMB: Morayo, Gabby, Josh, Jessica, Jeanne, Runze, Vinay, Albert, Margo, Stephen, Luisa, Bob, Laurel, Ryan, Tristen, Elia, Xingtong, Daisy, and Erin—I have learned as much from you as I have from anyone, and I can only hope that I was half as good a role model to you as the aforementioned were to me.

I must also thank the rest of the BMB program family, from the faculty and fellow researchers, especially Heidi Vitrac, as well as the administrative staff, particularly Cynthia, Bonnie, and Leticia. Thank you for the thoughtful questions, the illuminating insight, the exchange of ideas, supplies, and equipment, and for the assistance in all the behind-the-scenes work that allowed me to focus on my science.

Of notable importance among the faculty are my committee members, both Advisory/Supervisory and Exam, past and present: Jarek Aronowski, Ruth

Heidelberger, John Spudich, John Putkey, Eric Wagner, Darren Boehning, Jake Chen, and Shane Cunha, as well as Alex Gorfe in particular, who served not only on my committee but also as a collaborator and co-mentor. Thank you all for pushing me and probing me, for testing my limits as a scientist and for making sure I never veered off track.

Outside of GSBS, the faculty of my alma mater, the University of St. Thomas, also require thanks and acknowledgement. Drs. Steiger, Tinnerman, Palasota, Gries, Malloy, Crawford, Galloway, Rosell, Bagnall, Frohlich, and Romagni, as well as the rest of natural sciences faculty, all served to instill upon me the love of science for science's sake, and ensured I had the foundation necessary to grow into a real scientist.

Of course, I could not have performed the work in this dissertation without the help of our collaborators in the Landes and Sanabria labs. I would like to extend a particular thanks to David Cooper and Sudeshna Chatterjee—our experiments weren't always easy, but together we made it work and assembled something quite remarkable.

Finally, none of this work would have been possible without our funding. Vasanthi's ROIs, as well as my own funding from the Training in Pharmacological Sciences Training Grant and the Schissler Foundation Fellowship in Translational Studies of Common Human Disease, allowed us to always have the resources we needed to put forward the best science we could.

Thank you all for your contributions to my scientific development. The work presented here is truly the culmination of not only my efforts, but of yours as well.

FRET-BASED INVESTIGATIONS OF THE STRUCTURE-FUNCTION
RELATIONSHIPS IN THE NMDA RECEPTOR

Drew Matthias Dolino, B.S.

Advisory Professor: Vasanthi Jayaraman, Ph.D.

The *N*-methyl-D-aspartate (NMDA) receptor is one member of a class of proteins known as the ionotropic glutamate receptors. Ionotropic glutamate receptors mediate the majority of excitatory neurotransmission in the central nervous system, with the NMDA receptor standing out among these receptors for its requirement of a co-agonist, its magnesium-block-based coincidence detection, its slow kinetics, its calcium permeability, its allosteric modulation, and its especially important functional roles in synaptic plasticity, excitotoxicity, and more. In recent years, a wealth of structural information has come about describing endpoint structures to high resolution, but such structures are unable to fully resolve the movements and dynamics necessary for appropriate function. The work in this dissertation uses single molecule Förster Resonance Energy Transfer (smFRET) as a means to address that gap. We have examined the question of partial agonism of the NMDA receptor, noting a mechanism of a dynamically graded cleft closure. We have pushed the bounds of the temporal resolution

of such methods and been able to resolve fast dynamics of the ligand-binding domain, noting the adherence of the domain to the conformational selection model, and the revelation of a novel conformation leading to activation hitherto unknown. Finally, we have also directly examined the conformational dynamics of the transmembrane domain of the NMDA receptor with regards to its gating motions, granting unprecedented insight into the movements of the ion channel domain and elucidating a novel mechanism of allosteric inhibition. Such biophysical characterization of the NMDA receptor is essential, not only simply to know how the receptor works, but also to develop effective therapeutics that do not impair the receptor's important physiological roles.

Table of Contents

Approval Page	i
Title Page	ii
Copyright.....	iii
Dedication	iv
Acknowledgements.....	v
Abstract.....	vii
Table of Contents.....	ix
List of Illustrations.....	xiii
List of Tables	xv
Abbreviations	xvi
Chapter 1: Introduction to NMDA Receptors and post-synaptic function.....	1
Summary of NMDA receptor functional significance	2
Chapter 2: Structure of NMDA Receptors	6
Amino-Terminal Domain	8
Ligand-Binding Domain	10
Transmembrane Domain	12
Carboxyl-Terminal Domain	14
Chapter 3: Single-molecule Förster Resonance Energy Transfer	16

Chapter 4: Elucidating the Structural Mechanism of Partial Agonism of the NMDA	
Receptor.....	24
Results.....	26
Cysteine labeling versus unnatural amino acid labeling.....	26
smFRET investigations of the GluN1 LBD with full agonists, with partial agonists, and with antagonist.....	30
Discussion.....	35
Chapter 5: Probing NMDA Receptor Dynamics with Submillisecond Resolution	38
Results.....	41
smFRET experimental design and construct validation.....	41
Construction of smFRET histograms.....	41
Probability Distribution Analysis reveals three distinct conformations.....	45
Time window analysis reveals submillisecond dynamics.....	49
Discussion.....	58
Chapter 6: Investigation of the Gating Movements of the NMDA Receptor	61
Results and Discussion	63
Functional characterization of the smFRET construct.	63
smFRET identified distinct and stable states.	66
The conformational landscape associated with open and closed channel states. .	72
Comparison of desensitized and inhibited NMDA Receptor.	76

Dynamics of the NMDA receptor.	78
Transitions among the open and closed states.	84
Energetics of the NMDA receptor.	88
Concluding remarks.	88
Chapter 7: Conclusions and Future Directions	90
Future Directions	91
Further investigations into the LBD	91
Dynamics of the Amino-Terminal Domain.....	92
A closer look at the pore	92
The Carboxyl-Terminal Domain	94
Better technologies to study membrane proteins.....	94
Final Thoughts	95
Appendix: Materials and Methods	96
Generation of site-directed isolated GluN1 LBD mutants	96
LBD protein expression	96
LBD Protein purification	97
Labeling of LBD for FRET	101
Isothermal calorimetry	102
Attached-smFRET LBD sample preparation (132).....	102
Measurements of attached-FRET LBD data.....	103

Data analysis of attached-FRET LBD	104
Electrophysiology for testing the LBD mutants	105
Accessible Volume (AV) simulations to estimate measured distance	106
MFD for smFRET experiments.....	107
MFD histograms and FRET lines	108
Quantum yields	109
$\kappa^2 = 2/3$ Assumption, $\langle \kappa^2 \rangle$, and κ^2 Distributions	110
Probability distribution analysis (PDA)	112
Generation of smFRET constructs for TMD measurements.....	113
Electrophysiology for TMD measurements	114
Single molecule FRET sample preparation for TMD measurements.....	114
Flow chamber preparation for TMD measurements.....	115
Protein preparation and attachment to coverslips for TMD measurements	116
smFRET data acquisition for TMD measurements	117
Free energy calculations	117
Bibliography	119
Vita	145

List of Illustrations

Figure 1. Overview of NMDA Receptor structure	7
Figure 2. Excitation and Emission spectra of a typical FRET fluorophore pair	18
Figure 3. Crystal structure of the GluN1 ligand-binding domain.....	27
Figure 4. Labeling of wild-type proteins and mutant protein.....	28
Figure 5. Unnatural amino acids for use with single molecule FRET.....	29
Figure 6. Denoised smFRET histograms showing the population distribution of the GluN1 ligand-binding domain in various liganded states	31
Figure 7. Comparison of the smFRET histograms.....	33
Figure 8. Cleft closure versus activation	36
Figure 9. Experimental smFRET design and construct validation.....	40
Figure 10. MFD histograms of labeled GluN1 LBD with multiple ligands.....	43
Figure 11. Photobleaching and description of F_D/F_A histograms as modeled by PDA ...	47
Figure 12. Time window and PDA comparison of F_D/F_A histograms of the LBD with the various ligands	51
Figure 13. κ^2 distribution for LBD bound to: A, DCKA; B, Gly; C, D-Ser; D, L-Ala; and E, ACBC.....	54
Figure 14. Redistribution of population fractions	57
Figure 15. TMD smFRET constructs and characterization	65
Figure 16. Attached-FRET of full-length NMDA receptors shows specific pulldown ...	67
Figure 17. Denoised smFRET histograms of the NMDA receptor.....	69
Figure 18. Observed smFRET histograms of the NMDA receptor	71

Figure 19. Difference histograms clarify the changing conformational landscape of the NMDA receptor as it shifts between inactive and active conditions.....	75
Figure 20. Dynamics of the NMDA receptor show differences in transitional behavior under different ligand conditions.....	80
Figure 21. The coefficient of variation (CV) of each smFRET efficiency trajectory versus that trajectory's length	81
Figure 22. Transition maps and free energy diagrams of the NMDA receptor smFRET data	87
Figure 23. Characterization of the GluN1 agonist-binding domain after incorporation of <i>p</i> -acetyl-L-phenylalanine.....	100

List of Tables

Table 1. FRET Lines	44
Table 2. $\langle R_{DA} \rangle_E$ determined by PDA analysis	52
Table 3. F_D/F_A ratio for each given mean FRET distance	53
Table 4. Average steady state anisotropy (r_{ss}) per burst for the dyes on the ligand- binding domain at the conditions	54
Table 5. Mean κ^2 and estimated error ($(R_{DA}^{(\kappa^2)} / R_{DA}^{(\kappa^2=2/3)})\%$) on distances by using the assumption of $\kappa^2 = 2/3$	55
Table 6. Fastest relaxation time observed with PDA	55
Table 7. Overall fractions of PDA analysis including the donor only (bleached fraction)	58
Table 8. Conformational states sampled by the NMDA receptor under various liganded conditions.	70
Table 9. Autocorrelation data under the various ligated conditions.....	83
Table 10. Quantum Yields were estimated as described in Appendix	110

Abbreviations

ABD	Agonist-Binding Domain
ACBC	l-Amino-l-CycloButyl Carboxylic Acid
AcF	<i>p</i> -Acetyl-L-Phenylalanine
AMPA	α -amino-5-methyl-3-hydroxy-4-isoxazole propionate
ATD	Amino-Terminal Domain
AV	Accessible Volume
bAP	Back-propagating Action Potential
CaMKII	Calcium/Calmodulin-dependent Kinase II
CHS	Cholesteryl HemiSuccinate
CNS	Central Nervous System
CTD	Carboxyl-Terminal Domain
CV	Coefficient of Variation
D1	Upper lobe of the LBD
D2	Lower lobe of the LBD
DCKA	5,7-DiChloroKynurenic Acid
DDM	<i>n</i> -dodecyl- β -D-maltoside
EM	Electron Microscopy
FLIM-FRET	Fluorescence Lifetime Imaging Microscopy-Förster Resonance Energy Transfer
FRET	Förster Resonance Energy Transfer
HF	High FRET
iGluR	ionotropic Glutamate Receptor

LBD	Ligand-Binding Domain
LF	Low FRET
LRET	Luminescence Resonance Energy Transfer
LTD	Long-Term Depression
LTP	Long-Term Potentiation
M1	First Membrane-spanning helix of the NMDA receptor
M2	Re-entrant Membrane loop between M1 and M3 of the NMDA receptor
M3	Second Membrane-spanning helix of the NMDA receptor
M4	Third Membrane-spanning helix of the NMDA receptor
MD	Molecular Dynamics
MF	Medium FRET
MFD	Multi-parameter Fluorescence Detection
MK-801	Dizocilpine maleate
MNG-3	Lauryl Maltose Neopentyl Glycol
MSP	Membrane Scaffold Protein
NMDA	<i>N</i> -Methyl-D-Aspartate
NMR	Nuclear Magnetic Resonance
PBS	Phosphate-Buffered Saline
PEG	Poly-Ethylene Glycol
PIE	Pulsed Interleaved Excitation
R_0	Förster Radius, the distance at which FRET is half-maximal
R1	Regulatory Domain 1 (the upper lobe of the ATD)
R2	Regulatory Domain 2 (the lower lobe of the ATD)

SI	Sequence of the LBD prior to M1
S2	Sequence of the LBD after M3
SiMPull	Single-Molecule Pulldown
SMA	Styrene-Maleic Acid
smFRET	single molecule Förster Resonance Energy Transfer
STaSI	Step Transition and State Identification
STDP	Spike Timing-Dependent Plasticity
TCSPC	Time-Correlated Single Photon Counting
TIRF	Total Internal Reflection Fluorescence
TMD	TransMembrane Domain
VDCC	Voltage-Dependent Calcium Channel
w.res	Weighted Residuals

Chapter I: Introduction to NMDA Receptors and post-synaptic function

N-methyl-D-aspartate (NMDA) receptors are one member of a family of proteins known as the ionotropic glutamate receptors (iGluRs). These iGluRs, which also consist of the α -amino-3-hydroxy-5-methyl-4-isoxazole propionate (AMPA) and kainate receptors, are ligand-gated ion channels that mediate the majority of fast excitatory neurotransmission in the central nervous system (1). Because of this important role, NMDA receptors are implicated in behavior, cognition, and neural development, as well as in learning and memory. Conversely, dysfunction of NMDA receptors is similarly implicated in various neurological disorders such as depression, stroke, schizophrenia, epilepsy, and Alzheimer's disease (1-3).

Over the last decade and a half, a number of high-resolution crystal and cryo-EM structures have been published on the NMDA receptor, starting from the original studies of isolated domains (4-8) and eventually culminating in the structures of the 'full-length' NMDA receptor (9-12). However, these structures, though they have verified and expanded upon decades of previous structure-function studies, still leave many questions unanswered, especially with regard to the dynamic motions of the proteins. To address this gap, the work presented in this dissertation aims to examine the dynamic movements and conformational changes undergone by functional NMDA receptors and to synthesize the spectroscopic, structural, functional, and biochemical data available to clarify the mechanisms by which NMDA receptors activate and gate.

Summary of NMDA receptor functional significance

As mentioned above, the iGluRs are the main mediators of fast excitatory neurotransmission in the central nervous system (CNS). Briefly, when an excited neuron releases the neurotransmitter glutamate and the glutamate subsequently binds an iGluR, this binding event leads to a conformational change that results in the formation of a cation-permeable pore within the iGluR. Cations—typically sodium, potassium, and sometimes calcium (depending on the particular receptor)—flow down their electrochemical gradient through that pore, generating a net inward current (inward movement of cations, measured as negative amperes), a depolarization of the resting negative membrane potential toward zero and even toward positive millivolts, and the propagation of the excitatory signal (13). Other neurotransmitters exist, both excitatory and inhibitory, but glutamate remains the major excitatory receptor in the CNS, and thus glutamate's importance, as well as the importance of the iGluRs, to neurophysiology and neuropathology remains paramount.

Among the iGluRs, NMDA receptors hold a special role, such that the iGluR family is often divided into two classes: NMDA receptors and non-NMDA receptors (1). The features that distinguish NMDA receptors are myriad and include (i) voltage-dependent pore-block by magnesium (14, 15), (ii) a much higher calcium permeability relative to other iGluRs (16), (iii) slower gating kinetics (17-19), and (iv) the requirement of a co-agonist such as glycine (20) or D-serine (21) in order to activate the channel. These special features speak to the particularly important role of NMDA receptors to several cellular models of learning and memory (1).

NMDA receptor-dependent long-term potentiation (LTP) and long-term depression (LTD) are two such examples of NMDA-receptor mediated synaptic plasticity as a means to describe memory (22). LTP is a phenomenon by which neurons remodel a specific synapse to strengthen the effect of a future stimulus. The release of neurotransmitters from a single action potential alone is unlikely to elicit a robust NMDA-mediated response. Though glutamate and its co-agonist bind to the NMDA receptor, ion permeation through the receptor is inhibited by magnesium ions held in the pore by negative membrane potentials (14, 15). Instead, non-NMDA receptors such as the AMPA receptor provide the bulk of the initial spike of depolarization. With strong or frequent stimulation, though, the depolarization from non-NMDA-receptor sources can build up, allowing for the ejection of magnesium from the NMDA receptor pore and the ability of the NMDA receptor to experience a robust opening upon binding of its agonists (14, 15). This requirement of concurrent depolarization and agonist binding has led to NMDA receptors being described as coincidence detectors (1). Subsequent entry of calcium through activated NMDA receptors can then signal a series of downstream processes that lead to synaptic remodeling. In one example pathway of NMDA-receptor-mediated LTP, the calcium-triggered activation of kinases such as calcium/calmodulin-dependent kinase II (CaMKII) (23), among others (24-27), leads to phosphorylation of AMPA receptors, resulting in increased conductance and in increased transport to the synaptic membrane (28-30) in the early phase of LTP expression. Later phases, more dependent on downstream protein expression, manifest in such ways as spinal enlargement and increased spinal density (22). Conversely, weak or slow-frequency

stimulation of NMDA receptors leads to LTD and the weakening of the synapse. As LTP was largely kinase-mediated, LTD seems to prefer the activation of protein phosphatases such calcineurin and protein phosphatase 1, which have higher calcium/calmodulin affinity than CaMKII to allow for their activation despite the weaker calcium signal (22, 31-34).

Experimentally, LTP and LTD can be reliably induced by tetanic high-frequency stimulation (*e.g.* 100 Hz for 1 sec) and slow-frequency stimulation (*e.g.* 1 Hz for 10 min), respectively (22). Physiologically, spike timing-dependent plasticity (STDP) has gained ground as a more plausible model for LTP and LTD induction. With STDP, the synchrony of the synaptic input and post-synaptic action potential generation determine the propensity of the synapse to undergo either LTP or LTD, with pre-synaptic stimulation about 5-20 ms prior to post-synaptic action potential generation tending toward induction of LTP (35-37). Mechanistically, this pre-leading-post spike order allows for calcium-entry from back-propagating action potential (bAP)-activated voltage-dependent calcium channels (VDCCs) to combine supralinearly with NMDA receptor-mediated calcium entry, whose peak is delayed from the pre-synaptic signal due to the slow kinetics of magnesium unbinding (38) and the aforementioned slow kinetics of activation and deactivation (1). A post-leading-pre spike order, conversely, will lack this synergistic calcium response and may even result in a lower-than-baseline calcium signal due to calcium-dependent inactivation (see below) of the NMDA receptors from bAP-mediated VDCC activation (39). Consistent stimulation of the postsynaptic neurons in this order thus tends to lead to NMDA-receptor dependent LTD (35-37).

Though the above introduction focuses mainly on their post-synaptic effects, NMDA receptors are also located pre-synaptically (40, 41), extra-synaptically (42-45), and non-neuronally (46), where they serve a variety of roles, from pre-synaptic expression of plasticity (47), neuronal synchrony (48), and excitotoxicity (44, 49), to vasodilation (50, 51), glomerular filtration (52, 53), gustatory sensation (54, 55), and more (46). These roles underlie the importance of understanding the structural and biophysical mechanisms of NMDA receptor function as from this understanding, better treatments targeting pathologically aberrant dysfunction whilst maintaining NMDA receptor physiological roles can be developed (56).

Chapter 2: Structure of NMDA Receptors

NMDA receptors are obligate hetero-tetramers consisting of two glycine- (or D-serine-) binding GluN1 subunits and two other subunits, typically either glutamate-binding GluN2 (spanning GluN2A through GluN2D) or, less often, glycine- (or D-serine-) binding GluN3 (GluN3A and GluN3B) (17, 57). Though tetrameric, NMDA receptors and other iGluRs arrange in a 1-2-1-2 organization as a dimer of heterodimers and thus show pseudo-two-fold symmetry (58) (**Figure 1**). Each individual subunit has a modular architecture with distinct structural and functional domains: the extracellular amino-terminal domain (ATD), the extracellular ligand-binding domain (LBD) (also called the agonist-binding domain, ABD), the transmembrane domain (TMD), and the intracellular carboxyl-terminal domain (CTD) (1). Interestingly, subunit dimer pairing is not consistent throughout the length of the protein—the NMDA receptor and the other iGluRs undergo domain swapping, wherein a subunit will dimerize with one neighbor at the level of the LBD, and the opposite neighbor at level of the ATD (9, 10). Between each domain within a subunit, there are linkers connecting the distal and proximal domains, which seem to serve as sites through which tension induced from conformational changes in one domain is transmitted to the others (59-63). The structure and function of each domain will be further discussed below.

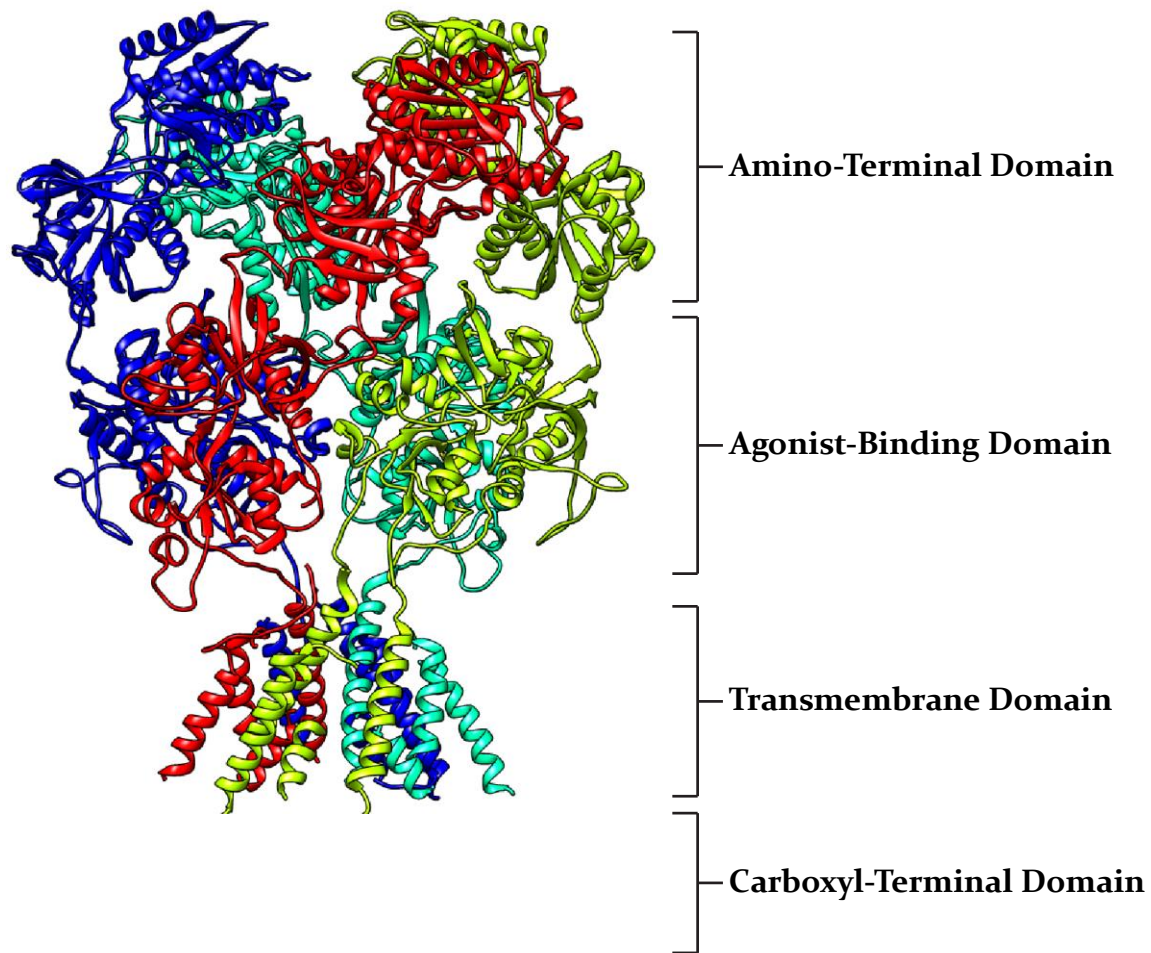


Figure 1. Overview of NMDA Receptor structure

The NMDA receptor is an obligate heterotetramer, typically consisting of two GluN1 (yellow and blue) and two GluN2 (red and green) subunits. Each subunit has a modular arrangement, with distinct functional and structural domains (labeled). The carboxyl-terminal domain has yet to be structurally elucidated.

Amino-Terminal Domain

The ATD layer of the NMDA receptor is the more distal of the two extracellular domain layers (**Figure 1**). It is typically the largest domain of each subtype and among the most diverse (1). Further, the ATD confers many of the subunit-specific properties among different NMDA receptor subunits. Chimera-swapping experiments in which individual domains of GluN2 subtypes were switched for the equivalent domain in a different subtype largely exhibit the property of the subtype to which the ATD, and especially the ATD-LBD linker, belonged (64, 65). However, these same studies also use GluN2 ATD-deletion mutations to show that the GluN2 ATD is not essential to form functional receptors in recombinant systems (64, 65). Conversely, the GluN1 ATD does seem to be essential to tetramer assembly (66) and function. ATDs from all subunits, though, do participate in regulation and allosteric modulation of the NMDA receptor and may also participate in the binding of extracellular proteins (67, 68).

Overall, the NMDA receptor ATD is organized into a bi-lobed clamshell-like structure (7), similar to the LBDs (discussed below). When describing the domain, it is often subdivided into the two lobes that comprise it: the upper lobe, known as regulatory domain 1 (R1); and the lower lobe, known as regulatory domain 2 (R2) (69). As these names imply, these domains play important roles in regulation and allosteric modulation of the NMDA receptor. This is in stark contrast to the AMPA receptor, in which the ATD seems to play mainly a structural and organizational role (1). This ability of the ATD to affect function may be a result of increased interaction and interdigitation seen between the ATD and LBD layers of the NMDA receptor as compared to that of the AMPA receptor (9, 10, 70). Both positive and negative allosteric

modulation of the NMDA receptor is facilitated by ATD interactions and, as will be discussed below with the LBD, this modulation is intimately tied to the closure or opening of the ATD clamshell cleft (71-73).

As mentioned previously, the GluN2 ATD plays a large role in the properties of the receptor as a whole, with chimeras swapping the ATD and its linker also swapping receptor open probability (P_o), response time course, and agonist potency (64, 65, 74). The differing effects of the ATDs on receptor function may be partially explained by the resting conformations of the ATDs: GluN2A, which has a more open ATD, allows for a larger open probability (around 0.5) than GluN2B, which has a more closed ATD (open probability around 0.1) (71, 73, 74). Such a relationship occurs because closure of the ATD cleft, via a raising of the lower lobe R2, results in an increase in tension in the linker connecting it to the LBD, destabilizing the LBD dimer interface that maintains an open channel (see below). Different allosteric modulators of the NMDA receptor also exploit this relationship by inducing or reducing ATD cleft closure to regulate channel activity. Zinc cations are endogenous modulators (75) that bind to a series of histidine residues between the upper and lower lobes of the ATD (76-78). Two additional histidine residues in particular play an important role in coordinating the high-affinity nanomolar binding of zinc to GluN2A, which may explain why the other GluN2 subunits show lower affinity micromolar binding (76, 77, 79, 80). The positioning of these coordinating histidines within and toward the outer end of the ATD domain cleft (7) was expected, given the ability of zinc to induce ATD cleft closure (71), but interestingly, the synthetic antagonist ifenprodil, which *via* homology to bacterial periplasmic binding proteins as well as by functional studies

(81) was predicted to also bind within the GluN2B ATD cleft, instead binds to the interface of the GluN1 and GluN2B ATD subunits (8). Despite this surprising localization, ifenprodil also induces ATD cleft closure, as first shown by Luminescence Resonance Energy Transfer (LRET) experiments (73), and subsequently confirmed by cryo-EM microscopy (11).

As ATD-mediated inhibition proceeds *via* a closure of the ATD cleft, ATD-mediated potentiation of NMDA receptors was hypothesized to proceed by an ATD cleft opening. Indeed, spermine is an endogenous polyamine that potentiates GluN2B-containing NMDA receptors (82, 83). Similar to ifenprodil, spermine binds at the interface between GluN1 and GluN2B ATD subunits (84), but in this case induces an opening of the ATD cleft (72). This potentiation by spermine and other polyamines is absent in NMDA receptors with GluN1 splice variants containing the polybasic exon 5, indicating that it is an electrostatic interaction between the polycationic spermine or exon 5 with the anionic lower R2 lobes of the NMDA receptor ATDs that pulls those lower lobes together to potentiate the channel.

Ligand-Binding Domain

The ligand-binding domain layer is the more proximal of the two extracellular domain layers of the NMDA receptor (**Figure 1**). As the name suggests, the LBD binds ligands, more specifically the agonists required to activate the channel (hence the LBD's other name—the agonist-binding domain). The GluN2 subunits bind glutamate, meriting the NMDA receptor's place among the glutamate receptors. The GluN1 and GluN3 subunits, however, bind a different co-agonist that is also required

for channel activation. The first full agonist known to activate these subunits was glycine (20), but since then D-serine has also been identified as another physiologically relevant full agonist (85, 86). The physiological relevance and distinction between the two full agonists has been debated, but it is now generally believed that D-serine is the main synaptic co-agonist while glycine acts more as an extrasynaptic agonist for NMDA receptors (87). This distinction is not universal, however, and glycine does remain the synaptic neurotransmitter at certain synapses (88). With this in mind, glycine, as the first identified co-agonist as well as the cheaper of the two GluN1 full agonists, has been the preferred co-agonist of choice for the GluN1 subunit for biophysical characterization, and GluN1 and its binding site will be hereafter described as glycine-binding.

As with the ATD, the LBD also folds as a bi-lobed clamshell-like structure (4-6). Unlike the ATD, the sequence encoding the NMDA receptor LBD is interrupted by two membrane-spanning helices (M1 and M3), as well as a re-entrant membrane loop (M2) (1, 9, 10). Thus, the LBD has been subdivided in two ways: by primary sequence (S1 and S2—sequence before and after the transmembrane sequences, respectively), and by tertiary folding (D1 and D2—upper and lower lobe, respectively). Much of the early work on the NMDA receptor LBDs has been performed on the isolated LBD, where S1 and S2 have been joined by a short glycine-threonine dipeptide linker (4-6, 89-91). These studies, as well as LRET studies on full-length receptors (92) have confirmed that the LBDs undergo a cleft-closure conformational change upon introduction of full agonists. Similarly, locking the LBD cleft closed via formation of disulfide bridges can also activate the channel in the absence of agonist (93). Cleft

closure is mediated by the raising of the D2 lobes, inducing a tension on the linkers between the LBD and TMD, which eventually pulls the channel open (59). During this process, the LBD heterodimers stay intact through the DI lobes, but under prolonged tension, the heterodimeric interface breaks, the dimer ruptures, and the receptor desensitizes (94).

Though full agonists have been shown to activate NMDA receptors by fully closing the LBD cleft, until the work of this dissertation the mechanism of how partial agonists partially activate the NMDA receptor has been unclear. Studies on the AMPA receptor produced a strong correlation between the degree of AMPA receptor LBD cleft closure and extent of AMPA receptor activation with the structures of partial agonists showing the cleft in an intermediate conformation of partial cleft closure (95-97). With the NMDA receptor, especially with the GluN1 glycine-binding domain, this relationship was not seen. Crystal structures of both full and partial agonists crystallized in the same conformation (4, 6). Experiments using ensemble LRET measurements were able to identify a state of partial cleft closure at the glutamate-binding GluN2 LBD, but again no resolvable difference in the GluN1 LBD could be distinguished (92). The exploration of this question and the mechanism of partial agonism at the GluN1 subunit will be the subject of Chapters 4 and 5.

Transmembrane Domain

Though the ATD and LBD control the timing of channel activation, it is through the transmembrane domain of the NMDA receptor that the ions actually flow in order to give the receptor most of its functional significance. The overall structure

of the TMD shows pseudo-fourfold symmetry and is arranged similar to an inverted potassium channel (98), although NMDA receptors have an extra M4 membrane-spanning helix which interacts with the neighboring M1 (9, 10). At the extracellular entrance to the pore, forming the linker between the C-terminal end of the pore-lining M3 helix of the GluN1 subunit and the LBD, is a DRPEER motif (63), which seems to confer an electronegative patch that facilitates calcium influx and conductance by attracting calcium to the area. Just proximal to the DRPEER motif is the Lurcher motif SYTANLAAF, forming the extracellular side of the M3 helix. Mutations in this helix have been shown to produce constitutively active channels; correspondingly, the elucidation of full-length structures has shown this motif to form the first and narrowest constriction in the ion channel (9, 10). Below this constriction is a water-filled central vestibule, followed by another constriction formed by the apex of the M2 pore loop (9, 10). This apex, which in GluA2 AMPA receptors harbors the Q/R editing site in GluA2 AMPA receptors that is responsible for calcium impermeability (99, 100), contains an asparagine in NMDA receptors whose identity is crucial for maintaining calcium permeability as well as magnesium block (101).

Importantly, the structural studies of the transmembrane domain have revealed only closed-pore conformations (9-12). Single channel electrophysiology data has indicated that there seem to be five closed and up to four open components, based on dwell times (102), but how those components relate to structural changes is unknown. Using cryo-EM microscopy, Tajima, *et al.* were able to identify a class of conformations that, based on the extracellular domains, they suggested to be the active conformation of the NMDA receptor (11). However, these data comprised only

17% of the identified particles, and their reconstruction was unable to resolve the TMD to any high degree. Nevertheless, the low resolution map that can be seen indicates that there are some large, backbone-changing conformational movements in the TMD present during channel activation. The mapping of the conformational changes of the NMDA receptor TMD is the subject of Chapter 6.

Carboxyl-Terminal Domain

The carboxyl-terminal domain is the least structurally clarified domain of the NMDA receptor. Believed to be intrinsically disordered, the CTD is not essential to function and has been removed from all the constructs used for high-resolution structural determination (9-12). Nevertheless, the CTD plays a number of roles, including membrane targeting, stabilization, and degradation (1). It contains a number of phosphorylation sites that control use-dependent desensitization (103) and trafficking (104, 105). Moreover, the CTD undergoes palmitoylation (106), and also, through interaction with calcium/calmodulin, mediates calcium-dependent inactivation (107-109).

Perhaps most interestingly, as well as controversially, the CTD is also responsible for metabotropic function of the NMDA receptor (110, 111). While NMDA receptors, as well as calcium, are necessary for induction of both LTP and LTD, blocking of NMDA receptor ion flux by either a pore blocker or by a GluN1 competitive antagonist does not prevent LTD induction (112). This finding was both refuted (113) and confirmed (114), by independent groups, highlighting the controversy in the area. Given the length of the NMDA receptor CTD, there would be precedent

for a non-ionotropic mechanism mediated by intracellular conformational changes, and indeed FLIM-FRET experiments with GluN1 subunits tagged with GFP and mCherry show conformational changes even when ion flux is blocked (115). To date, the CTD has been the least studied domain of the NMDA receptor, but these studies show that there is still a wealth of information to be discovered about its functions.

Chapter 3: Single-molecule Förster Resonance Energy Transfer

This chapter is based in part upon Dolino, D. M., S. S. Ramaswamy, and V. Jayaraman. 2014. Luminescence Resonance Energy Transfer to Study Conformational Changes in Membrane Proteins Expressed in Mammalian Cells. e51895. The full article may be found at <http://www.jove.com/video/51895/luminescence-resonance-energy-transfer-to-study-conformational>.

The preceding two chapters have highlighted the importance of NMDA receptor function and have illustrated some of the gaps present in the literature regarding the structure-function relationships that govern NMDA receptor activity. The high-resolution structural information of the outermost three domains has provided great insight into the endpoints of conformational activity, but information about the movements and dynamics of the receptor in between those endpoints is lacking. In order to address this gap, we have used single-molecule Förster Resonance Energy Transfer as a means to directly assess conformational changes during changes in NMDA receptor function.

Förster Resonance Energy Transfer, or FRET, is a technique that can be used as a molecular ruler to measure distances and distance changes between donor and acceptor fluorophores within the range of 10-100 Å (116, 117). In this range, if the emission spectrum of the directly-excited, donor fluorophore overlaps with the absorption spectrum of the acceptor fluorophore (**Figure 2**), resonance energy transfer can occur where the donor transfers its energy non-radiatively to the acceptor. The efficiency of this transfer is highly distance-dependent and can be described by the following equation:

$$E = \frac{R_0^6}{R^6 + R_0^6} \quad (1)$$

where R is the distance between the two fluorophores, E is the efficiency of transfer, and R_0 , defined below, is the Förster radius for the fluorophore pair, *i.e.* the distance at which efficiency of transfer is half-maximal. From this equation, one can see that efficiency is related to the magnitude of the distance raised to the sixth power, and it is this sixth power dependence that allows for FRET measurements to be exquisitely sensitive to even small distance changes when near the R_0 of the FRET pair.

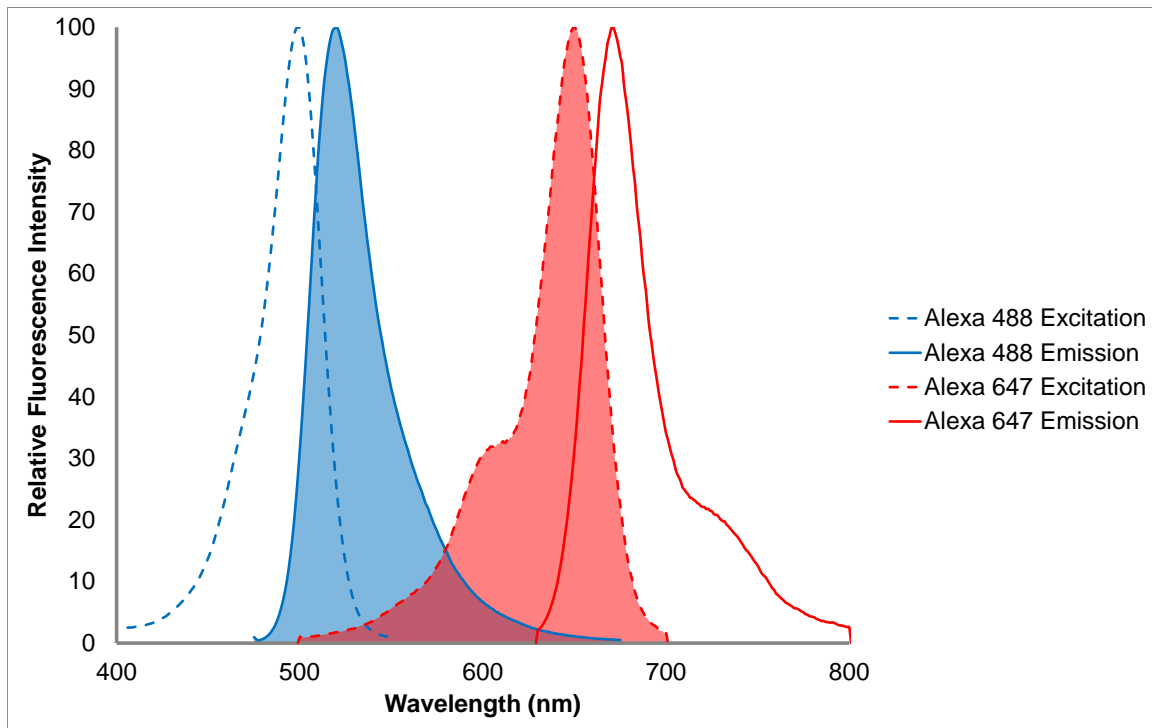


Figure 2. Excitation and Emission spectra of a typical FRET fluorophore pair

Excitation spectra are shown in dashed lines, and emission spectra are shown in solid lines. Donor spectra are shown in blue, and acceptor spectra are shown in red. FRET can occur when the emission spectrum of the donor overlaps with the excitation spectrum of the acceptor (highlighted), and results in a highly distance-dependent non-radiative energy transfer. The area of overlap is known as the overlap integral, and is an important factor in characterizing the R_0 for a fluorophore pair.

FRET efficiency E is defined as the ratio of the rate of energy transfer, k_{FRET} , divided by the total rate of decay, $k_{\text{FRET}} + \sum k_{\text{other}}$ for the donor fluorophore:

$$E \equiv \frac{k_{\text{FRET}}}{k_{\text{FRET}} + \sum k_{\text{other}}} \quad (2)$$

Taking the relationship of lifetime being the inverse of the rate, this equation can be rewritten:

$$E = \frac{\tau_D - \tau_{DA}}{\tau_D} \quad (3)$$

where τ_D is the lifetime of the donor fluorophore alone (representative of the rate of decay for all other processes), and τ_{DA} is the lifetime of the donor when participating in energy transfer with the acceptor (representative of the sum of $k_{\text{FRET}} + \sum k_{\text{other}}$) (118).

When measuring donor lifetime, care must be taken to account for background donor-only lifetimes in cases where there is incomplete labeling or photobleaching of the acceptor. To circumvent this complication, LRET experiments using lanthanide cations acting as donor fluorophores measure the lifetime of sensitized acceptor emission, *i.e.* acceptor emission resulting from excitation *via* donor energy transfer rather than direct acceptor excitation. Because the lifetime of the organic acceptor fluorophore is so short compared to the lifetime of even a FRETting lanthanide (nsec vs μsec), the acceptor lifetime can be considered instantaneous and thus be used as a good reporter of FRET donor lifetime (119).

Fluorophore lifetime measurements of single molecules can also be achieved using time-correlated single photon counting (TCSPC) technology or by frequency modulation; however, given the expense of the equipment needed for these techniques, intensity-based FRET measurements can be taken, integrating the

fluorescence over the course of 10 - 100 msec. In this case, a proximity ratio, PR, can be taken as the ratio of acceptor fluorescence to total fluorescence:

$$PR = \frac{I_A}{I_D + I_A} = \left(1 + \frac{I_D}{I_A}\right)^{-1} \quad (4)$$

where I_A is the intensity of acceptor emission and I_D is the intensity of donor emission.

To relate this proximity ratio to actual FRET efficiency, background signal, spectral cross-talk, and direct acceptor excitation must be subtracted from the raw signal, such that

$$\begin{aligned} I_D &= S_D - \langle B_D \rangle - \beta(I_A + f_{dir}) \\ I_A &= S_A - \langle B_A \rangle - \alpha I_D - f_{dir} \end{aligned} \quad (5)$$

where S_i is the raw signal from either donor (D) or acceptor (A) prior to any correction; $\langle B_i \rangle$ is the mean background signal, taken either between bursts or from each spot after photobleaching; β is the spectral cross-talk parameter of acceptor emission detected in the donor channel; α is the spectral cross-talk parameter of donor emission detected in the acceptor channel, and f_{dir} is direct excitation of the acceptor by the donor laser. The spectral cross-talk parameters can be obtained by directly exciting singly-labeled samples and taking the appropriate ratio of background-corrected signal; whereas f_{dir} is simply measured as the background-corrected acceptor signal upon excitation with the donor laser.

Furthermore, the signal detected from a given quantity of excited molecules will be dependent on the detection efficiency at that wavelength and the molecule's quantum yield, and so the differences in those values between the donor and acceptor must be accounted for in accurate efficiency determination. These two factors are combined into the single correction factor γ , where

$$E = \left(1 + \gamma \frac{I_D}{I_A}\right)^{-1} \quad (6)$$

And

$$\gamma = \frac{\eta_A \Phi_A}{\eta_D \Phi_D} \quad (7)$$

with η_A and η_D being the detector efficiency of acceptor and donor emission, respectively, and Φ_A and Φ_D being the quantum yield of the acceptor and donor fluorophores, respectively. These values can be measured empirically, or γ can also be measured as the magnitude of the ratio of the change in signal after acceptor photobleaching (120) as a means to normalize the change in measured signal to the same corrected emission:

$$\gamma = \left| \frac{\Delta I_A}{\Delta I_D} \right| \quad (8)$$

where ΔI_A is the change in measured acceptor signal after acceptor photobleaching, and ΔI_D is the change in measured donor signal after acceptor photobleaching.

After calculating the FRET efficiency, the distance between the fluorophores can then be calculated with equation 1, given the R_0 value of the FRET pair. If the R_0 value is unknown for the pair of fluorophores, it can be calculated via the following equation:

$$R_0 = \left(\frac{8.785 \times 10^5 \times \kappa^2 \times \Phi_D \times J}{n^4} \right)^{1/6} \quad (9)$$

where, R_0 is the Förster radius in angstroms, κ^2 is the orientation factor between the two dyes usually assumed to be $2/3$, Φ_D is the quantum yield of the donor, n is the refractive index of the medium, and J is the spectral overlap integral between the donor's emission spectrum and the acceptor's absorbance spectrum in $M^{-1}cm^{-1}nm^4$

(Figure 2). J is defined in equation 10

$$J = \int \overline{f_D}(\lambda) \epsilon_A(\lambda) \lambda^4 d\lambda \quad (10)$$

where $\overline{f_D}$ is the donor emission spectrum normalized to an area of 1, ϵ_A is the molar absorbance coefficient of the acceptor at the given wavelength in $\text{M}^{-1}\text{cm}^{-1}$, and λ is the wavelength in nm (116-118).

The κ^2 value given in equation 9 is the orientation factor. Fluorescence and energy transfer, being dipole interactions, are dependent on the relative orientation of those dipoles. If the dipoles are oriented in parallel, the orientation factor will be at its maximum of 4. If the dipoles are orthogonal to each other, they will be at a minimum value of 0. In practice, the long linkers attached to the fluorophore dyes allow for free rotation of the dyes and an average κ^2 value of experimental measurements to be close to the theoretical average of 2/3 (121). An uncertainty of 10% in the R_0 can be assumed with confidence, while gathering anisotropy data directly can lower this uncertainty to 2.5% or lower (91). Keeping this in mind, by affixing FRET fluorophore pairs onto proteins via site-directed labeling, single molecule and even ensemble FRET can be used to make high-precision measurements of protein conformational changes and structure (121, 122).

Isolation of single molecules for smFRET can be done in two main ways. In the first, very dilute and highly pure FRET-labeled samples are simply dropped onto a clean glass slide, with the labeled samples allowed to diffuse around. Using a confocal microscope, the experimenter can focus onto a small, femtoliter-size confocal volume in the middle of the sample solution. As labeled sample diffuses into and out of the confocal volume, they will give off bursts of fluorescence emission that will then be

detected as single molecule FRET data (91, 123). In the second method of isolation, labeled samples are physically attached to microscope slides. These slides must be extremely clean and passivated, typically using PEG, to prevent any non-specific binding of proteins or other contaminants. To capture protein, the layer of PEG can be doped with biotinylated PEG, which will then irreversibly bind streptavidin. Biotinylated antibodies can then pull down proteins or other samples of interest (89, 90, 120).

Each method of single molecule isolation has its pros and cons. With diffusing-FRET, the sample must be very pure—many contaminants fluoresce and thus it may be difficult to distinguish contaminant signal from actual sample signal. Assuming that the slide is clean and the antibodies specific, attached-FRET allows for the washing away of contaminants, but the assumption of clean slides and specific antibodies is not always a safe one. Attached-FRET allows for the tracking of single molecules over a period of seconds, limited only by photobleaching times. Diffusing-FRET can only capture FRET traces for as long as a molecule stays within the confocal volume, though efforts have been made to capture proteins within lipid vesicles to lengthen the dwell time. Finally, the confocal-based microscopy combined with time-correlated single photon counting (TCSPC) measurements can allow for the capture of fast dynamics, even faster than the up-to-80 MHz pulse rate of the laser (see Chapter 5), whereas the best cameras for TIRF-based attached FRET go to around 30 msec resolution. Confocal microscopy and TCSPC data collection can also be used with attached-FRET, but this comes at a cost of throughput (120, 123). Analysis of the smFRET data is similar and will be discussed in the relevant chapters below.

Chapter 4: Elucidating the Structural Mechanism of Partial Agonism of the NMDA Receptor

This chapter is based upon research originally published in *The Journal of Biological Chemistry*. Dolino, D. M., D. Cooper, S. Ramaswamy, H. Jaurich, C. F. Landes, and V. Jayaraman. Structural Dynamics of the Glycine-binding Domain of the N-Methyl-D-Aspartate Receptor. *Journal of Biological Chemistry*. 2015; 290: 797-804. © the American Society for Biochemistry and Molecular Biology.

As discussed in Chapter 2, one of the central questions concerning the NMDA receptor prior to the work of this dissertation was how agonist binding leads to channel activation. Insight into iGluR structure and function had previously been dominated by studies on the AMPA receptor and has shown that the LBD folds into a clamshell-like shape that can close upon its ligands, inducing conformational changes that result in channel opening. Crystal structures of the AMPA receptor LBD showed that the extent of this cleft closure correlates with the efficacy of the ligand, with weak agonists inducing partial closure, and full agonists inducing full cleft closure and full channel activation (95-97, 124-126). Such a relationship between LBD cleft closure and ion channel activation provided an elegant means of explaining the link between conformational changes at the LBD and opening of the channel pore (127). Moreover, smFRET experiments as well as NMR experiments on the AMPA receptor showed that, in addition to the inherent ability of a ligand to induce cleft closure, the dynamics of the LBD also play an important role in dictating activation (128-133).

With the NMDA receptor, while at the glutamate-binding site of the NMDA receptor the extent of cleft closure at the LBD does appear to correlate to activation,

such a graded cleft closure was not observed, either by crystal structures or by ensemble LRET measurements, for the glycine-binding domain (4, 6, 92, 134). Based on the crystal structures of the isolated LBDs, it has been suggested that the glycine-binding GluN1 subunit could follow a mechanism of conformational selection wherein the apo state probes both the closed- and open-cleft conformations. In this mechanism, agonist efficacy is governed by the stabilization of the closed conformation rather than the formation of intermediate states as was noted with the AMPA receptor LBD. Consistent with this hypothesis and with the distinction from AMPA receptors, theoretical investigations of the apo state of GluN1 revealed a narrowly distributed closed-cleft population in addition to an expected broad open-cleft population (135). While the theoretical studies shed light on the apo- and glycine-bound states of the NMDA receptor, experimental evidence for the mechanism of partial agonism at the LBD still remained largely unknown.

To address this question, we used smFRET to allow us to examine the conformational landscape that the isolated glycine-binding GluN1 LBD (GluN1 SIS2) probes in the presence of full agonists, partial agonists, or an antagonist. Additionally, in order to specifically label the protein at desired sites, we incorporated the unnatural amino acid *p*-acetyl-L-phenylalanine into the protein (136). The unique ketone group of *p*-acetyl-L-phenylalanine can be coupled to hydrazide-conjugated fluorescent dyes for the smFRET studies. Although smFRET on glutamate receptors has been done before through the labeling of cysteine residues (132, 133), this new procedure allows us to investigate the protein without concern of labeling or mutating out native cysteine residues. We found that there is significant overlap between the different

liganded states with the antagonist-bound protein samples exhibiting both the closed- and open-cleft conformations, similar to what has been predicted with the molecular dynamics simulations (135). Interestingly, we also found that the partial agonist-bound proteins show greater rigidity in its population distribution, which was different from what has previously been observed in the AMPA receptors (133).

Results

Cysteine labeling versus unnatural amino acid labeling

Previous protocols to study single molecule dynamics typically make use of cysteine residues to enable site-specific labeling (132, 133). An important first step for such approaches is to remove endogenous cysteines that may be undesirably labeled. In the GluN1 LBD there is one non-disulfide-bonded cysteine at position 459 (**Figure 3**). The C459S mutant S1S2 protein could not be expressed well in *Escherichia coli*. Further, smFRET investigations of wild-type protein labeled with thiol-reactive dyes shows signal at the donor emission frequency but not at the acceptor frequency (FRET signal) relative to the blank slide studied under the same conditions (**Figure 4a and Figure 4b**). This result indicates that the single cysteine is accessible under these labeling conditions, while the disulfide bonded cysteines are not labeled. This is further confirmed by the double cysteine mutant at positions S507 and T701 which shows signal in both the donor and acceptor frequencies (**Figure 4c**).

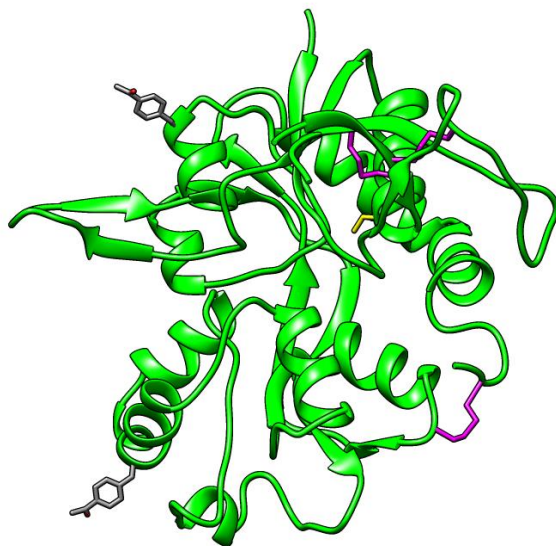


Figure 3. Crystal structure of the GluN1 ligand-binding domain

Sites 507 and 701 were chosen to probe the dynamics of the GluN1 LBD and are shown here in stick form with AcF side chains. Native cysteines involved in disulfide bridges are shown in magenta, with the free cysteine shown in yellow.

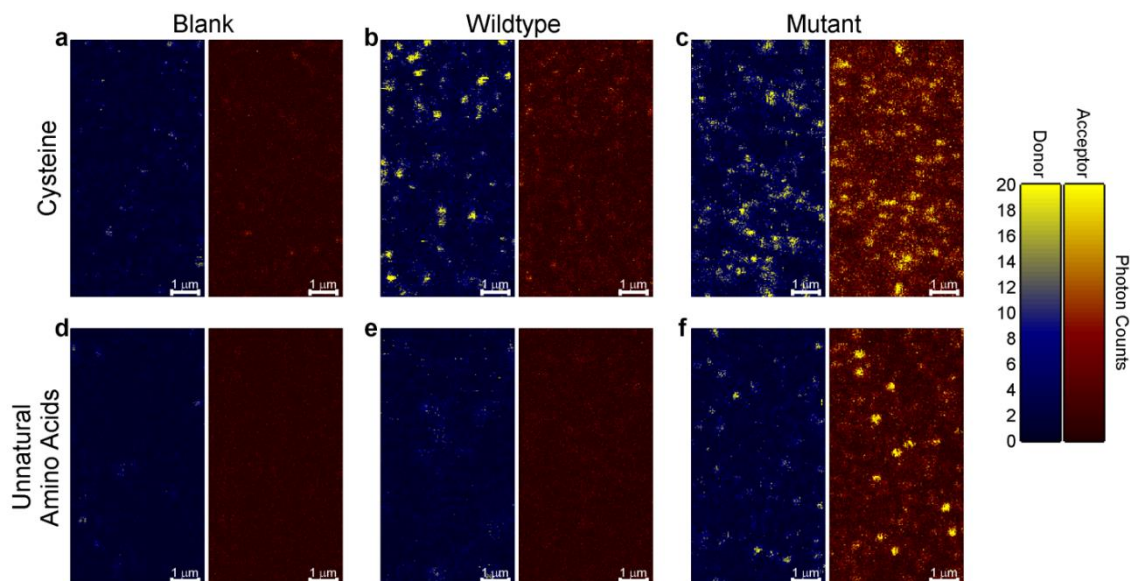


Figure 4. Labeling of wild-type proteins and mutant protein

Blue and red images show the donor and the acceptor channel response, respectively, for the same areas. *A, D*, Blank slides without any protein bound. *B*, Purified wild-type protein labeled with 1:1 ratio of maleimide derivatives of Alexa 555 and Alexa 647 showing labeling of the C459. *C*, Purified protein with cysteines at positions 507 and 701, labeled with 1:1 ratio of maleimide derivatives of Alexa 555 and Alexa 647. *E*, Purified wild-type protein labeled with 1:1 ratio of hydrazide derivatives of Alexa 555 and Alexa 647. *F*, Purified protein with AcF inserted at positions 507 and 701 labeled with 1:1 ratio of hydrazide derivatives of Alexa 555 and Alexa 647.

These considerations made it difficult to use cysteines for analyzing dynamic data. To address this issue, we introduced the unnatural amino acid *p*-acetyl-L-phenylalanine (AcF) by mutating to an amber stop codon at site 507 in Domain 1 and at site 701 in Domain 2 (**Figure 3**, **Figure 5**).

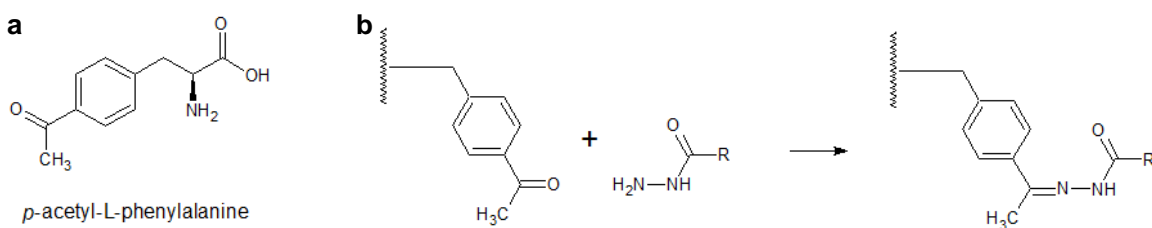


Figure 5. Unnatural amino acids for use with single molecule FRET

A, The unnatural amino acid used for these experiments was *p*-acetyl-L-phenylalanine (AcF). *B*, Overview of the reaction between the AcF side chain and the hydrazide functional group. The ketone of AcF reacts with the hydrazide to form a covalent hydrazone bond.

In contrast to the experiments with the thiol reactive fluorophores, the wild-type protein shows no signal even after overnight treatment with ketone-reactive dyes, similar to the blank control (**Figure 4d** and **Figure 4e**), indicating that none of the

natural amino acids are reactive to the ketone-reactive dyes. Additionally, the mutant protein with AcF at positions 507 and 701 showed signal at both the donor and acceptor frequencies showing that the dyes specifically label only the introduced AcF (Figure 4f).

smFRET investigations of the GluNI LBD with full agonists, with partial agonists, and with antagonist

The GluNI LBD was examined by smFRET in the presence of the full agonists glycine and D-serine, the partial agonists L-alanine and 1-amino-1-cyclobutane carboxylic acid (ACBC), and the antagonist 5,7-dichlorokynurenic acid (DCKA) (Figure 6a-e). Donor and acceptor photon counts of excited proteins were measured with millisecond resolution, collected into 10 ms bins for efficiency determination, denoised using wavelet decomposition, and then plotted as separate histograms as described previously (132, 133, 137).

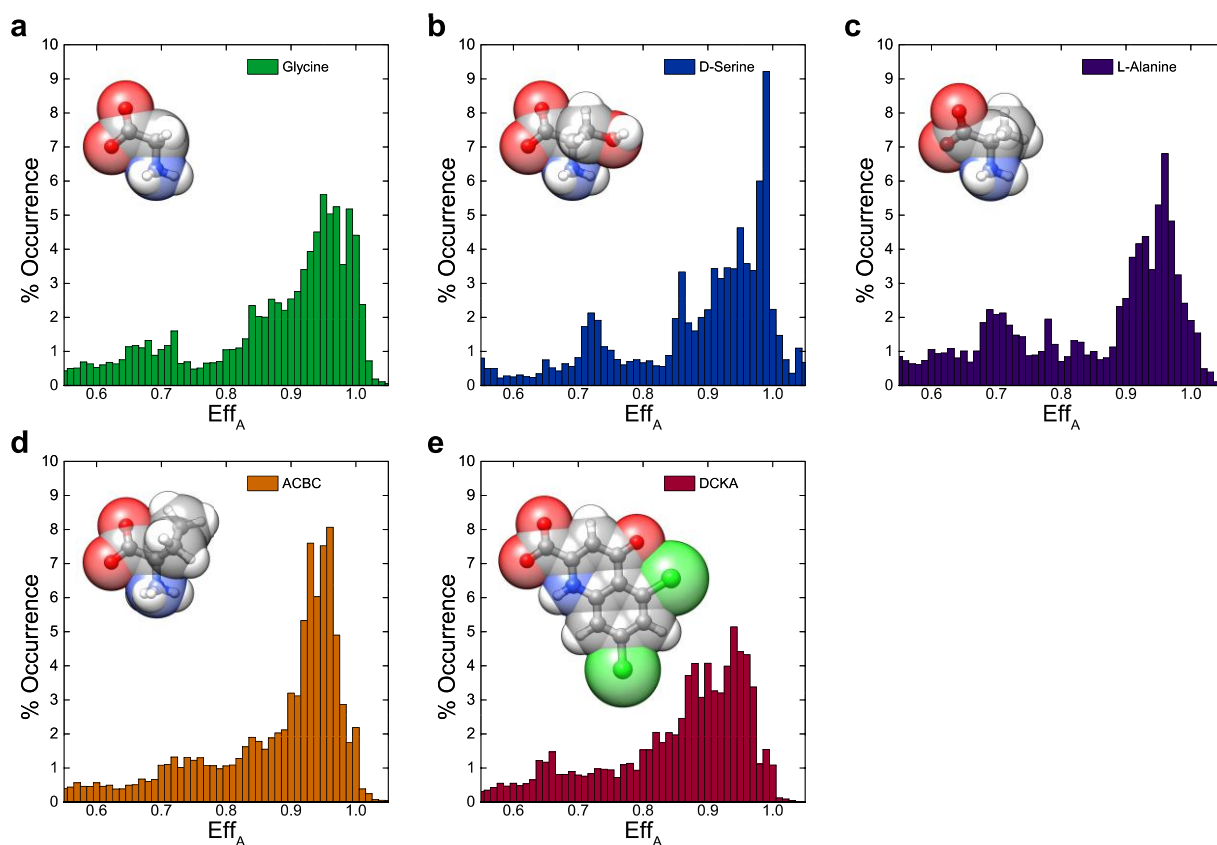


Figure 6. Denoised smFRET histograms showing the population distribution of the GluN1 ligand-binding domain in various liganded states

Distribution of FRET values for the GluN1 LBD when bound to *A*, full agonist glycine (85 molecules), *B*, full agonist D-serine (28 molecules), *C*, partial agonist L-alanine (38 molecules), *D*, partial agonist ACBC (166 molecules), and *E*, antagonist DCKA (121 molecules).

The smFRET histograms of the different ligand-bound states show FRET efficiencies that range from 1 to 0.5 with a peak at 0.95. The FRET efficiency of 0.95 corresponds to a distance of 31 Å. This distance is similar to the 34 Å measured in the crystal structure between the C α of residue 507 and the C α of residue 701, which is in good agreement with the FRET data, given that the FRET distances are measured between the fluorophores (4). A smaller peak appears around an efficiency of 0.72, corresponding to a distance of 44 Å. This distance is comparable to the 41 Å distance measured in the apo crystal structure. The fact that the different liganded states show occupancy covering this entire range suggests that the protein probes both the “closed” and “open” cleft conformational states (135). The small fraction of occupancies (summing to less than 10%) at efficiencies below 0.6 reflect hyperextended open-cleft conformations that are most likely accessible due to the isolated nature of the LBD and the absence of the membrane and amino-terminal domain.

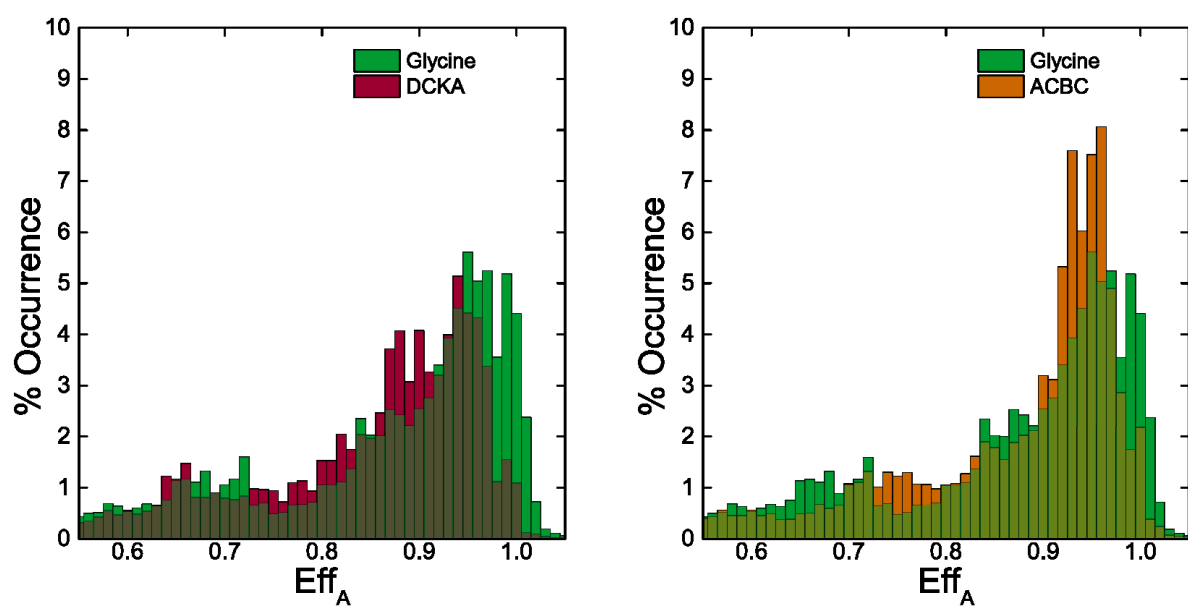


Figure 7. Comparison of the smFRET histograms

A, Comparison of the smFRET histogram for the LBD when bound to antagonist DCKA (dark red) or with the full agonist glycine (green). *B*, Comparison of the smFRET histograms for the GluN1 LBD when bound to full agonist glycine (green) or partial agonist ACBC (orange).

A shift toward lower efficiency states is seen when comparing the smFRET data of full agonists to that of the antagonist DCKA (**Figure 7a**). Specifically, the DCKA-bound form of the protein has a reduced number of occurrences at 0.96 or higher efficiencies and a much larger fraction at 0.88 efficiency (37 Å) relative to the forms bound to the full agonists glycine or D-serine. This trend to lower efficiencies is again consistent with the crystal structures which show an open-cleft conformation for the antagonist-bound protein (4). Interestingly, the common 0.95 peak underlies the significant overlap in the smFRET data between the antagonist- and agonist-bound forms of the GluN1 LBD. This data is consistent with theoretical calculations of the apo state of the glycine-binding domains of the NMDA receptor, which show that the protein probes both open- and closed-cleft conformations (135). The smFRET data, however, do not show a clear appearance of a new, distinct population between the two liganded forms, but only a shift in the population from a more closed-cleft conformation in the full-agonist-bound state to a more open-cleft conformation in the antagonist-bound state (**Figure 7a**).

The histograms for the GluN1 LBD when bound to the partial agonists ACBC or L-alanine also show a peak FRET efficiency at 0.95, which corresponds to a distance of 31 Å (**Figure 6**). This distance is in agreement with the distance of 32 Å measured in the crystal structure of the ACBC-bound LBD between the C α of residue 507 and the C α of residue 701 (6). The LBD in complex with L-alanine has not been crystallized. The peak efficiency seen in the partial agonist-bound forms of the LBD is similar to that found in the glycine-bound state of the protein, again consistent with the crystal structures that show a similar closed-cleft conformation with all activating agonists.

Crucially, both of the partial agonist-bound forms of the LBD probe smaller ranges of conformations and are thus more rigid compared to the glycine-bound state of the protein (**Figure 7b**). Moreover, between the two partial agonists, the ACBC-bound form seems even more rigid than L-alanine, in line with ACBC being a less effective partial agonist than the latter (6, 138). This finding seems to be in direct contrast to the AMPA receptor, which shows a broader range of closed-cleft conformations when comparing partial agonist-bound forms to full agonist-bound forms (133).

Discussion

Here, we have shown that the mechanisms of agonist action at GluN1 are different from those of AMPA receptors due to the fact that the protein tends to occupy a much narrower spread of states in the full agonist-, partial agonist-, and antagonist-bound forms. The differences are more evident in the partial agonist- and antagonist-bound forms, as a decrease in agonism for the AMPA receptors is reflected by a large increase in the spread of cleft-closure states. In the GluN1 LBD the shifts are much less dramatic. The decreased spread in the cleft-closure states probed by the GluN1 LBD could be one of the reasons that no significant changes were observed in the extent of cleft closure in the crystal structures between the partial agonist- and full agonist-bound forms.

While the two receptors show differences in terms of dynamics of the LBD between the various ligand-bound states, there is still a linear dependence for the GluN1 LBD between activation and the fraction of protein exhibiting FRET efficiencies greater than 0.96 (**Figure 8**). This result is similar to what was observed in the AMPA

receptors where a similar linear dependence between the fraction of receptors in high-efficiency states versus activation was observed (133). Thus, while the dynamics are different for the two subtypes, the underlying mechanism wherein the extent of cleft closure controls extent of receptor activation still seems to be preserved.

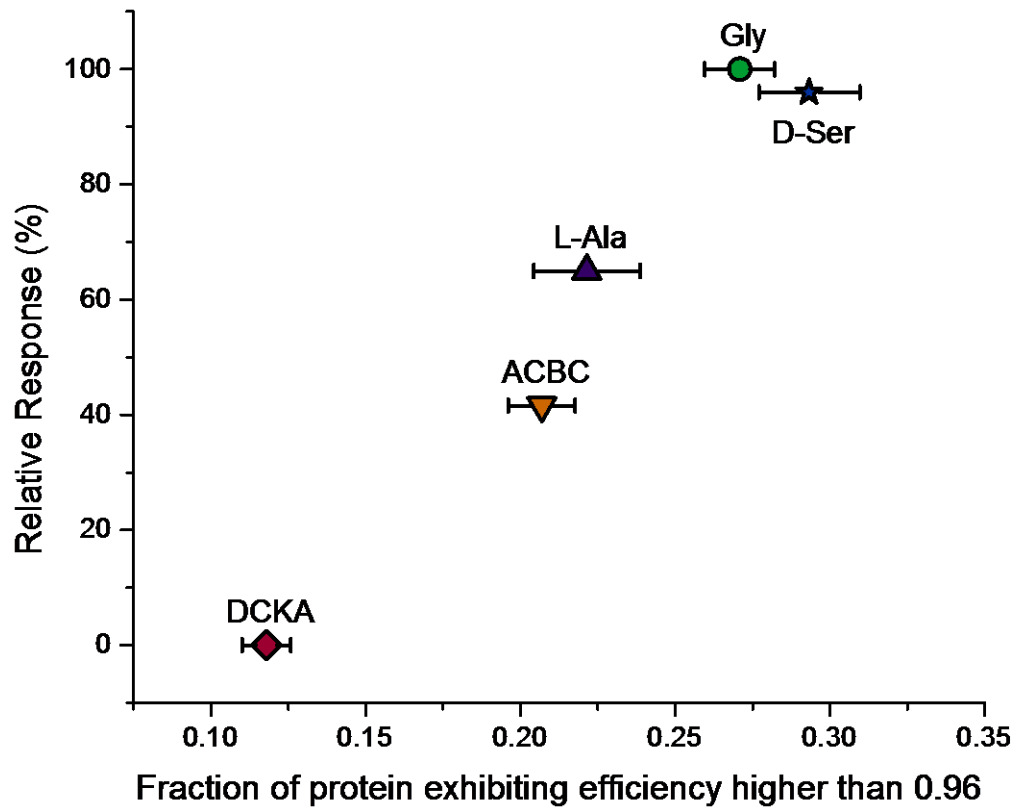


Figure 8. Cleft closure versus activation

Plot of the fraction of the LBD of the GluN1 subunit that exhibits FRET efficiencies higher than 0.96 versus normalized mean currents (6, 138) obtained with the corresponding ligands in full-length GluN1/GluN2B receptors.

Apart from the characterization of the GluNI LBD dynamics, the studies performed here show that unnatural amino acids can be used as a means to label proteins for smFRET. The ability to introduce amino acids with a unique ketone functional group allows for labeling of proteins with high specificity. Avoiding the conventional thiol-maleimide chemistry allows investigators to disregard any problems with cysteines native to the protein, as well as alleviating worries about the formation of disulfide bridges with the introduced cysteines. The commercial availability of *p*-acetyl-L-phenylalanine, as well as the commercial availability of various hydrazide-conjugated fluorescent labels, allows for the use of a wide variety of FRET fluorophore pairs with various distance ranges.

In conclusion, we have demonstrated here the use of ketone-containing unnatural amino acids for smFRET measurements to analyze the conformational dynamics of the GluNI LBD in complex with the full agonists glycine and D-serine, the partial agonists L-alanine and ACBC, and the antagonist DCKA. The use of unnatural amino acids allows for the specific labeling of proteins and has the flexibility of being used with a wide variety of fluorophores. The smFRET histograms of the GluNI LBD show a common high-efficiency peak, corresponding to a closed-cleft conformation accessible to all examined liganded forms of the protein. These data are consistent with previous theoretical results where the closed conformation was seen in both apo- and glycine-bound forms of GluNI. Additionally, the difference in efficacy appears to be correlated with the ability of the ligand to select specifically for the closed conformation.

Chapter 5: Probing NMDA Receptor Dynamics with Submillisecond Resolution

This chapter is based upon research originally published in *The Journal of Biological Chemistry*. Dolino, D. M., S. Rezaei Adariani, S. A. Shaikh, V. Jayaraman, and H. Sanabria. Conformational Selection and Submillisecond Dynamics of the Ligand-binding Domain of the *N*-Methyl-D-aspartate Receptor. *Journal of Biological Chemistry*. 2016; 291: 16175-16185. © the American Society for Biochemistry and Molecular Biology.

The previous chapter dealt with a first look at understanding the mechanism of partial agonism. To do so we used attached smFRET with cutting edge unnatural amino acid technology to provide the first experimental evidence of a partial agonist-dependent change in the conformational equilibrium of the GluN1 LBD; however, the time resolution for those experiments was limited to 10 ms. With the kinetic movements of the GluN1 LBD occurring faster than this resolution (139) and the lack of a clear conformational model, more robust experimental methods were needed to clarify this mechanism of partial agonism.

To probe the conformational landscape of the GluN1 LBD at faster time scales than previously studied, we used smFRET and multi-parameter fluorescence detection (MFD) to obtain a complete experimental investigation of the dynamics and conformational equilibrium of the GluN1 LBD. MFD experiments can be used as another method of obtaining smFRET data, but in contrast to obtaining the intensity-based FRET efficiency of individual molecules over a period of seconds, MFD experiments simultaneously measure a number of fluorescence parameters, including intensity, lifetime, and anisotropy of molecules, as they diffuse one at a time through a

small confocal volume. The use of time-correlated single-photon counting (TCSPC) allows for the exploration of dynamic motions in a broad range of time scales, down to picoseconds (123), making this method particularly well suited for observing the mechanism of partial agonism of the GluN1 LBD. The isolated GluN1 LBD was purified, and site-directed labeling with fluorescent dyes was performed to probe the distance across the LBD cleft (**Figure 9**) (90). The results presented here show that the GluN1 LBD exhibits a common closed cleft, active arrangement among a variety of agonists, with partial agonists showing less stability of the closed conformation and more dynamic conversions to the open conformations. Moreover, we find among the FRET states one conformation, which resembles within 2.8 Å the published crystallographic structure for the glycine-bound configuration, and another state that differs only by 1.6 Å from the DCKA-bound structure (4).

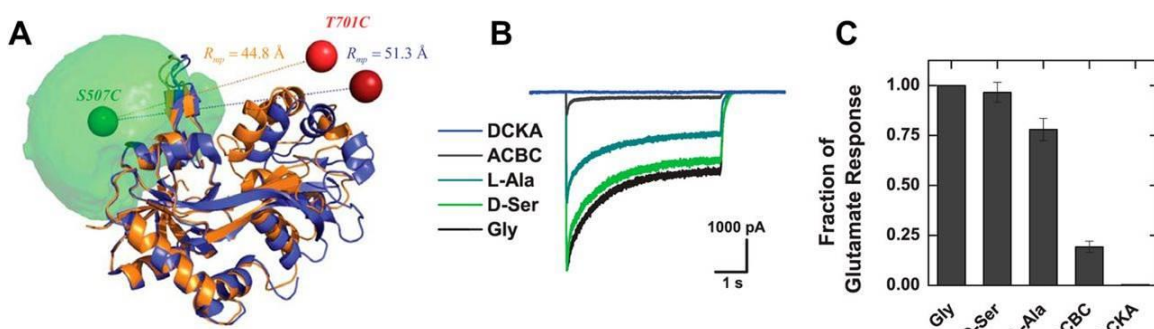


Figure 9. Experimental smFRET design and construct validation

A, Schematic representation of the glycine-bound (PDB code 1PB7, *orange*) and DCKA-bound (PDB code 1PBQ, *blue*) conformations of the GluN1 ligand-binding domain of the NMDA receptor. The accessible volume (AV) simulations were calculated to determine the available space that the fluorescent marker will occupy with the donor (Alexa 488) at Ser-507 and acceptor (Alexa 647) at Thr-701. The *green* “AV-cloud” represents all the locations the donor dye can access, and the *green* and *red* spheres represent the mean positions of the dyes for donor and acceptor, respectively, for each structure. The distance between the mean position at each conformation is $R_{mp} = 44.8$ and 51.3 Å for glycine and DCKA bound, respectively. Their corresponding expected mean FRET efficiency distances are $\langle R_{DA} \rangle_E = 48.7$ and 54.2 Å. B and C, whole cell electrophysiological recordings were performed to confirm retained functionality and efficacy of ligands with GluN1 S507C/T701C. B, a representative trace shows the reduced efficacy of the two partial agonists, ACBC and L-alanine, relative to the two full agonists, glycine and D-serine, as well as the antagonist DCKA. C, group data showing the relative efficacy of each ligand with respect to glycine. Glycine: 100%, D-serine: $94 \pm 1\%$, L-alanine: $84 \pm 6\%$, ACBC: $25 \pm 4\%$, DCKA: $0.3 \pm 0.1\%$.

Results

smFRET experimental design and construct validation

The GluNI LBD was mutated to cysteines at Ser-507 and Thr-701 (full-length sequence) on opposite sides of the cleft as has previously been described (89, 90), and then labeled using the FRET pair Alexa 488 and Alexa 647, with an R_0 of 52 Å. Based on crystallographic studies of the glycine-bound (PDB code IPB7, *orange*) and DCKA-bound (PDB code IPBQ, *blue*) conformations of the LBD, we performed *in silico* labeling and determined the expected mean FRET efficiency distance $\langle R_{DA} \rangle_E = 48.7$ and 54.2 Å, for both structures, respectively (**Figure 9a**). With this construct, one should be able to observe the clamshell closure due to the binding of different ligands.

To verify that these mutations (GluNI S507C/T701C) do not abolish the functionality and efficacy of ligands in the full receptor, we obtained whole cell electrophysiological recordings (**Figure 9b**). Ligand efficacy was determined by normalizing to the maximum amplitude in presence of the full agonist glycine. As expected, D-serine, also a full agonist, has similar efficacy to glycine, followed by L-alanine and ACBC. The last two are considered partial agonists (**Figure 9c**).

Construction of smFRET histograms

For single molecule experiments, we used pulsed interleaved excitation (PIE) of donor and acceptor fluorophores to excite the doubly labeled LBD. The emitted fluorescence photons were collected to measure various FRET efficiency indicators of single molecules of the LBD when in complex with different ligands (glycine, 1 mM; D-serine, 1 mM; L-alanine, 15 mM; ACBC, 10 mM; or DCKA 100 µM). FRET efficiency was

measured simultaneously through both intensity measurements and donor lifetime measurements in the presence of the acceptor (**Figure 10**). The resulting single-molecule events or burst histograms are presented in a multidimensional representation, where each event was preselected according to a 1:1 donor to acceptor stoichiometry. The cleaned FRET signal is shown as contours on two-dimensional histograms and as filled histograms over the one-dimensional $\langle\tau_{D(A)}\rangle_f$ and F_D/F_A projections. The green sigmoidal line over the two-dimensional histogram represents the static FRET line (Equation 13 (see Appendix), Table 1), which is the theoretical relationship between the two FRET indicators: the donor fluorescence average lifetime $\langle\tau_{D(A)}\rangle_f$ and the ratio of donor-to-acceptor fluorescence (F_D/F_A). Populations that lie on the line indicate FRET states that are “static” (123), *i.e.* populations with dynamic interconversion rates that are slower than the burst duration.

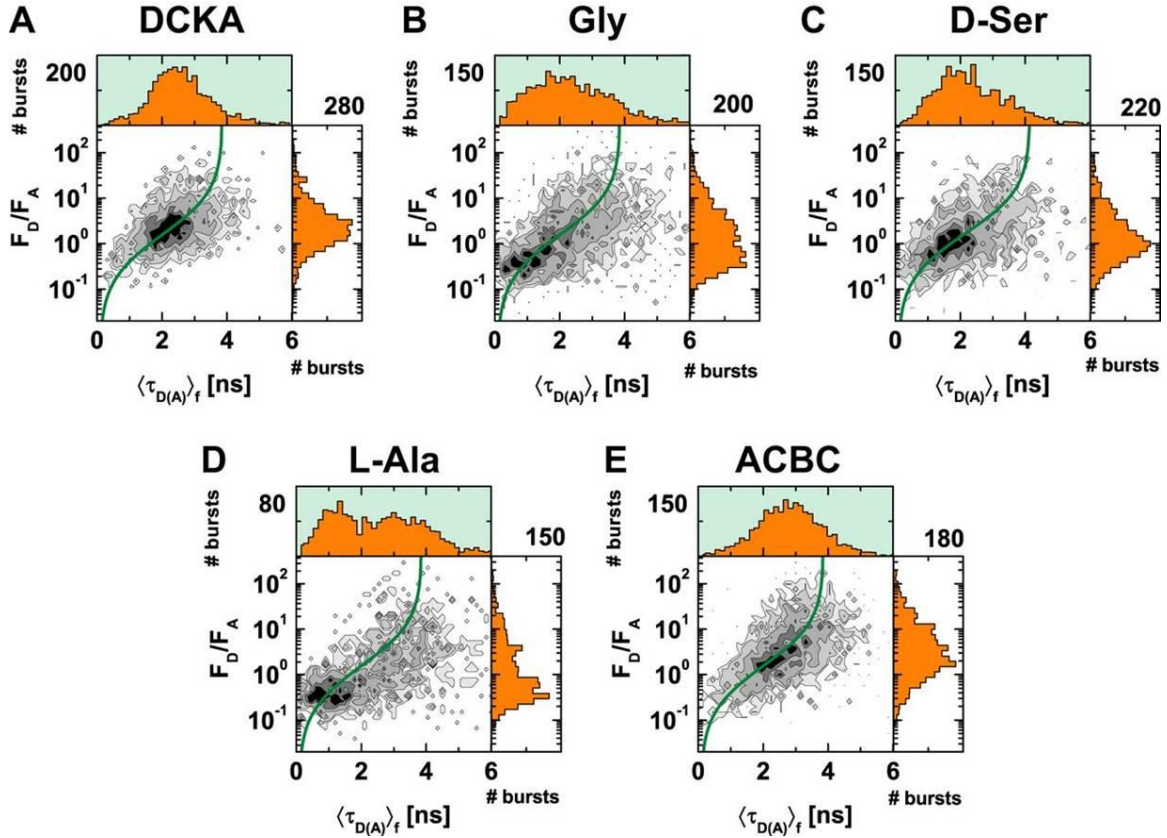


Figure 10. MFD histograms of labeled GluN1 LBD with multiple ligands

Two-dimensional single molecule FRET histograms using burst analysis of F_D/F_A distribution versus fluorescence averaged lifetime ($\langle \tau_{D(A)} \rangle_f$). The green line is the static FRET line, which describes the relationship between F_D/F_A and fluorescence averaged lifetime ($\langle \tau_{D(A)} \rangle_f$). The GluN1 LBD of the NMDA receptor was diluted to picomolar concentrations in the present of various ligands. A, 0.1 mM DCKA; B, 1 mM glycine; C, 1 mM D-serine; D, 15 mM L-alanine; and E, 10 mM ACBC. The following parameters were used: $\langle B_G \rangle$ Gly = 0.93, $\langle B_R \rangle$ Gly = 0.51, $\langle B_G \rangle$ D-Ser = 0.93, $\langle B_R \rangle$ D-Ser = 0.532, $\langle B_G \rangle$ L-Ala = 0.842, $\langle B_R \rangle$ L-Ala = 0.502, $\langle B_G \rangle$ ACBC = 0.955, $\langle B_R \rangle$ ACBC = 0.518, $\langle B_G \rangle$ DCKA = 0.94 $\langle B_R \rangle$ DCKA = 0.522, β = 0.02 (fraction of direct excitation of acceptor with donor excitation laser), α = 0.017, and g_G/g_R = 3.7.

Table 1. FRET Lines

Equation B3 was used for each different experiment.

Sample	Static FRET Line
Gly	$\frac{(0.7732/0.4240)}{((3.8660/((-0.0405*\langle\tau_{D(A)}\rangle_f^3)+(0.2914*\langle\tau_{D(A)}\rangle_f^2)+0.4891*\langle\tau_{D(A)}\rangle_f-0.0422))-1)}$
D-Ser	$\frac{(0.8286/0.4290)}{((4.1430/((-0.0348*\langle\tau_{D(A)}\rangle_f^3)+(0.2676*\langle\tau_{D(A)}\rangle_f^2)+0.4977*\langle\tau_{D(A)}\rangle_f-0.0443))-1)}$
L-Ala	$\frac{(0.8426/0.4130)}{((4.2130/((-0.0335*\langle\tau_{D(A)}\rangle_f^3)+(0.2622*\langle\tau_{D(A)}\rangle_f^2)+0.4998*\langle\tau_{D(A)}\rangle_f-0.0448))-1)}$
ACBC	$\frac{(0.7990/0.3810)}{((3.9950/((-0.0377*\langle\tau_{D(A)}\rangle_f^3)+(0.2799*\langle\tau_{D(A)}\rangle_f^2)+0.4932*\langle\tau_{D(A)}\rangle_f-0.0432))-1)}$
DCKA	$\frac{(0.8498/0.3960)}{((4.2490/((-0.0329*\langle\tau_{D(A)}\rangle_f^3)+(0.2594*\langle\tau_{D(A)}\rangle_f^2)+0.5008*\langle\tau_{D(A)}\rangle_f-0.0451))-1)}$

These MFD histograms show clear differences in the conformational landscapes probed by the GluNI LBD in complex with various ligands. As expected, with the antagonist DCKA, mostly medium to low FRET states are explored, with a longer donor fluorescence lifetime and a larger donor-to-acceptor fluorescence ratio ($F_D/F_A = 3.3$) (**Figure 10a**). This is consistent with the stabilization of an open cleft conformation. When in complex to the full agonist glycine, the FRET states shift toward higher FRET efficiencies, indicated by lower donor fluorescence lifetimes and smaller donor to acceptor fluorescence ratios (**Figure 10b**). This is also consistent

with the stabilization of the closed cleft conformation. A second full agonist, D-serine, shows a similar trend (**Figure 10c**), although not as pronounced. To assess the LBD conformational space and dynamics across a variety of activation states we examined two partial agonists (L-alanine and ACBC). Between the two, the more effective partial agonist L-alanine (**Figure 10d**) resembled more the two full agonists, and the less effective partial agonist ACBC (**Figure 10e**) resembled more the antagonist histogram, similarly to the whole cell recordings (**Figure 9b**). Of note, the histograms for the two partial agonists seemed to spread across a wider variety of conformational states, though these states must be to some extent static because they lie along the green FRET line. Altogether, it is then evident that none of the ligands trap a single state of the LBD, but rather ligand binding redistributes the population of the conformational states consistent with the mechanism of conformational selection.

Probability Distribution Analysis reveals three distinct conformations

To quantitatively analyze the conformational space and dynamic effects induced by ligand binding, we used probability distribution analysis (PDA) (140, 141). We used various models to fit the one-dimensional fluorescence ratio histograms with multiple time windows ($\Delta t = 5, 2, \text{ and } 0.5 \text{ ms}$). In addition, we use PDA to identify the mean FRET efficiency distance ($\langle R_{D(A)} \rangle_E$) between the donor and acceptor for each limiting state. For each conformational state, we use Gaussian distributions that represent the interdyne donor-acceptor distance distributions. In PDA analysis, the width (hw_{DA}) of each distribution is given by acceptor photophysics (142). To identify the model that best represents the experimental data, we carry out a systematic

approach of identifying the minimum number of shot-noise limited states (no Gaussian distribution of states). We reached a reasonable convergence with three different FRET states based on visual inspection of the weighted residuals (w. res) and the figure of merit χ^2 . To improve the fit, we added the contribution of the donor-only population due to acceptor bleaching. Although we have burst selection with 1:1 donor-to-acceptor stoichiometry, the presence of donor-only population indicates that a significant fraction of the acceptor is photobleached within the duration of the time window. To identify and remove this artifact further, we used the ratio of the prompt signal corresponding to the TCSPC channels of donor excitation (S_{prompt}) and total uncorrected signal of donor and acceptor emission over all TCSPC channels (S_{Total}) (donor and acceptor excitation in PIE experiments) (**Figure 11a**). It is worth mentioning that the stoichiometry parameter is corrected for quantum yield and detection efficiencies; however, the raw detected signal (S) does not require additional corrections. Therefore, this selection serves as an additional identification of events that smear toward the donor only population due to photobleaching. We ruled out the possibility of a very low FRET state due to very long interdye distances because after the $S_{\text{prompt}}/S_{\text{Total}}$ (**Figure 11a**) selection there were no remaining bursts with high enough F_D/F_A ratio and 1:1 stoichiometry.

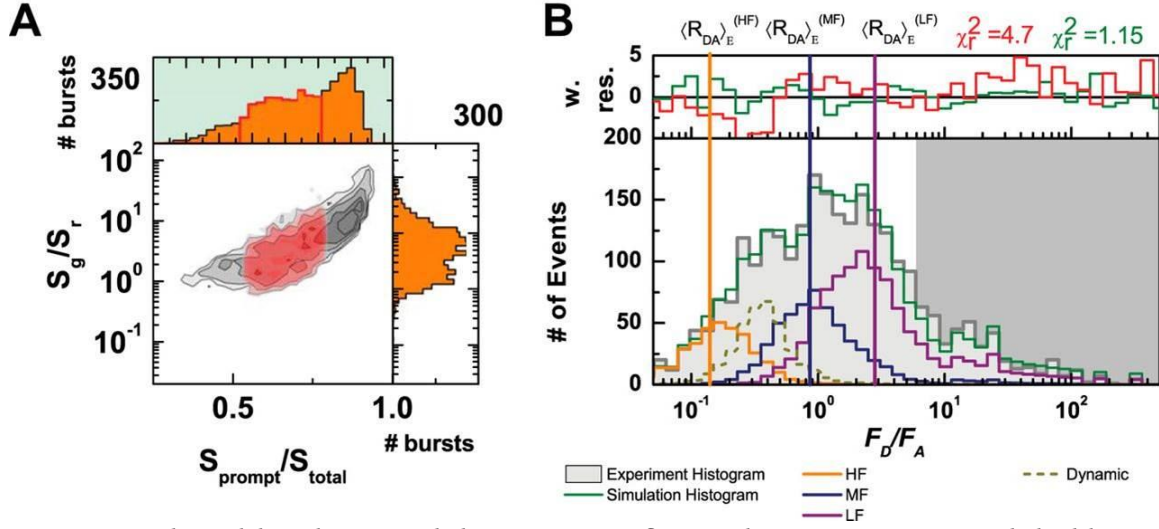


Figure 11. Photobleaching and description of F_D/F_A histograms as modeled by PDA

A, Removing all acceptor photobleaching due to incorrect signal of prompt channel over all data ($0.5 < S_{Prompt}/S_{Total} < 0.8$). B, Experimental and PDA-modeled F_D/F_A histogram distributions at $\Delta t = 5$ ms for the LBD in the presence of glycine. Three limiting states were depicted as Gaussian distributions, each with a different color (high FRET, *orange*, medium FRET, *navy*, and low FRET, *wine*). The mean F_D/F_A value of each distribution is shown as a vertical line with the same color code. Each line correlates to the experimentally determined interdyne distance per state or $\langle R_{DA} \rangle_E$. One dynamic transition is shown as Gaussian (dashed *dark yellow* line).

After identifying the minimum number of FRET-related conformations, we increased the level of complexity in the fitting model. For example, we know that intensity-based FRET parameters are determined by fluctuations on the integrated acquisition time. PDA is particularly susceptible for capturing the blinking behavior of dyes, which produces additional broadening of the distribution beyond the shot noise limit. This behavior has been well characterized (142). It is known that broadening is caused mostly due to acceptor blinking and it follows a monotonic relationship with respect to the interdye separation distance (142). Thus, each FRET-related conformational state will have its own distribution of distances with a particular width (hw_{DA}) and mean interdye distance $\langle R_{DA} \rangle_E$. Note that R_{mp} and $\langle R_{DA} \rangle_E$ represent different distances (see accessible volume in Appendix). Benchmark studies (121, 143) have shown that 6% of the interdye distance $\langle R_{DA} \rangle_E$ is a typical effective width per state. Thus, we fixed the distribution width to 6% of each $\langle R_{DA} \rangle_E$. Broadening beyond this limit would be considered to emerge from dynamic processes.

To exemplify this representation, we show in **Figure 11b** the experimental and PDA modeled F_D/F_A histogram distributions at $\Delta t = 5$ ms for the LBD in presence of glycine. Here, we identify three limiting states depicted as Gaussian distributions, each with different color (high FRET *orange*, medium FRET *navy*, and low FRET *wine*). The mean F_D/F_A value of each distribution is shown as a *vertical line* with the same color code. Each line correlates to the experimentally determined interdye distance per state or $\langle R_{DA} \rangle_E$. In addition to three limiting states, one dynamic transition, also shown as Gaussian (*dark yellow*), is added to statistically improve the fitting quality. For example, in this case χ^2 decreases from 4.7 to 1.15, when dynamics is included at

$\Delta t = 5$ ms. Weighted residuals (w. res.) are shown on top layer for visual representation of the goodness of the fit. In a simplified representation it is possible to only show the model distribution as compared with the experimental histogram and the *vertical lines* for representing the mean F_D/F_A value per state. Hereafter, this simplified representation will be used.

Time window analysis reveals submillisecond dynamics

To study if there were any dynamic processes involved in the submillisecond to millisecond time scale between states, the experimental F_D/F_A distributions were globally fit using three time windows ($\Delta t = 5, 2$, and 0.5 ms). If all states were static within the time window, the static model would roughly fit all time windows equally well and the probability distribution would not change. This was the case for the LBD bound to DCKA and ACBC, suggesting slow kinetics with those ligands (**Figure 12** for DCKA and ACBC). The figure of merit χ^2 and the modeled F_D/F_A distribution are shown in *red* when the states are treated as static and it is shown in *green* when the model includes a dynamic transition. If during the selected time window, a molecule switches multiple times between states, the fluorescence bursts of the interconverting molecules will show different degrees of mixing between states; thus changing the probability distribution. This is only true if the dynamic interconversion occurs at time scales that are smaller or comparable to the selected time window. The need for a dynamic state was noticeable for the glycine, D-serine, and L-alanine bound states (**Figure 12**), whereas for DCKA and ACBC χ^2 increases with the addition of a dynamic state.

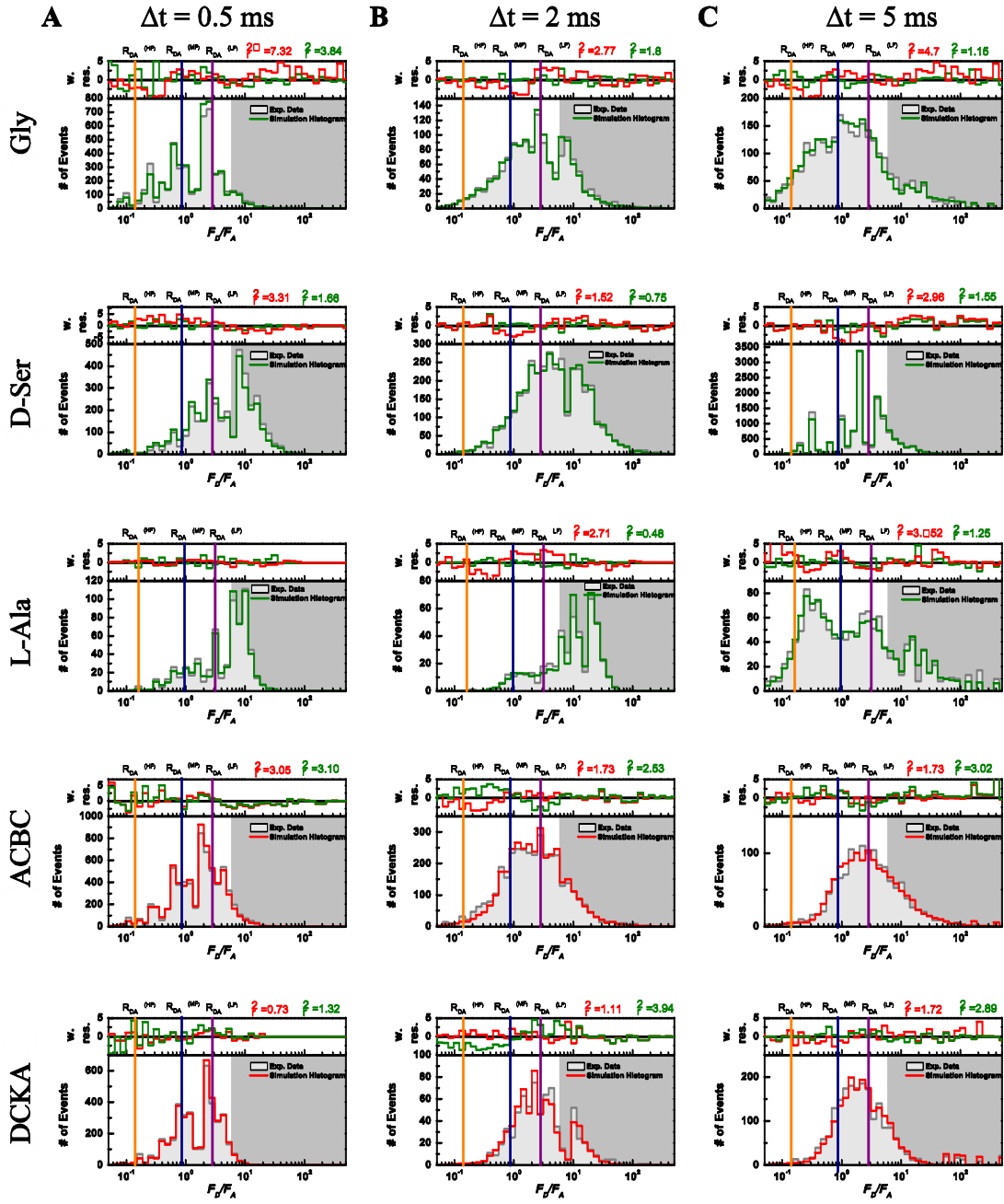


Figure 12. Time window and PDA comparison of F_D/F_A histograms of the LBD with the various ligands

Time window (Δt) analysis for 0.5, 2, and 5 ms (A–C, respectively). The same F_D/F_A correction parameters are used as described in the legend to Figure 10. The dynamic PDA model consists of three static FRET states (HF, MF, and LF) plus a single two-state kinetic transition between HF and MF. Fractions are renormalized to consider only FRET populations. We observe that glycine has a faster relaxation time compared with L-alanine as glycine equilibrates within the selected time windows. A similar result is seen with D-serine. Splitting of populations occur in the case of L-alanine. Relaxation times are shown in Table 2. Vertical lines correspond to the mean FRET efficiency distance of the three limiting states (HF, *orange*; MF, *blue*; and LF, *magenta*; Table 2). Donor only or acceptor photobleaching region has a dark gray background. Tables 2, 3, 6, and 7 summarize the results from PDA.

The larger differences comparing multiple time windows in the distribution for L-alanine are indicative of intermediate kinetics in the millisecond to submillisecond time scales. It is obvious in this case that there is a split of states with an increase in population of the higher FRET states. Faster kinetics equilibrates the distribution at shorter time windows as seen in the case of glycine because there is no split of states. However, there is evidence of population redistribution toward higher FRET efficiencies or lower F_D/F_A ratios. Therefore, the static model use of three FRET states is no longer valid. To include the dynamic component we tested the addition of a single two-state transition between any FRET states. Remember that the mean F_D/F_A value of each state is shown as a vertical line with the same color code and the relationship to distance can be readily determined (**Tables 2 and 3**).

Table 2. $\langle R_{DA} \rangle_E$ determined by PDA analysis

Sample	High-FRET (HF) [Å]	Medium-FRET (MF) [Å]	Low-FRET (LF) [Å]
All	33.9	45.8	55.8

Table 3. F_D/F_A ratio for each given mean FRET distance

Sample	High-FRET (HF)	Medium-FRET (MF)	Low-FRET states (LF)
Gly	0.14	0.86	2.8
D-Ser	0.15	0.9	2.9
L-Ala	0.16	1.0	3.1
ACBC	0.16	1.0	3.2
DCKA	0.16	1.0	3.2
$F_D/F_A = (\text{Quantum Yield Donor}/\text{Quantum Yield Acceptor}) * (R_{DA}/R_0)^6 \quad (R_0=52 \text{ \AA})$			

We observed that the single two-state kinetic state ($HF \rightleftharpoons MF$) was needed to significantly improve our figure of merit (χ^2) across time windows for the LBD bound to the full agonists and to the partial agonist L-alanine. In summary, for all cases, we identified three FRET states with the following interdyer distances: the high FRET (HF) ($\langle R_{DA} \rangle_E = 33.9 \text{ \AA}$), medium FRET (MF) ($\langle R_{DA} \rangle_E = 45.8 \text{ \AA}$), and low FRET states (LF) ($\langle R_{DA} \rangle_E = 55.8 \text{ \AA}$) (**Table 2**).

These distances were determined with the assumption that $\kappa^2 = 2/3$. To validate this assumption, the κ^2 distribution for these conditions was determined using the wobble in a cone model (**Figure 13**). For this, we assume that the residual anisotropies can be approximated in the worst case scenario to the average steady state anisotropy per burst, or $\langle r_{ss} \rangle \cong r_\infty$, for D -only (donor), A (acceptor), and $A(D)$

(the sensitized by FRET emission of acceptor) from single molecule experiments (Table 4). As the observed κ^2 value will be dynamically averaged among all possible values within this distribution, we then use the mean value, $\langle \kappa^2 \rangle$, to calculate distance and observe that the maximum error introduced by this assumption is 2.5% (Table 5), thus, validating our assumption.

Table 4. Average steady state anisotropy (r_{ss}) per burst for the dyes on the ligand-binding domain at the conditions

r_{ss}	Gly	D-Ser	L-Ala	ACBC	DCKA
D-only	0.15	0.13	0.1	0.15	0.11
A	0.36	0.06	0.04	0.06	0.07
D(A)	0.18	0.18	0.13	0.18	0.15
A(D)	0.03	0.04	0.03	0.04	0.05

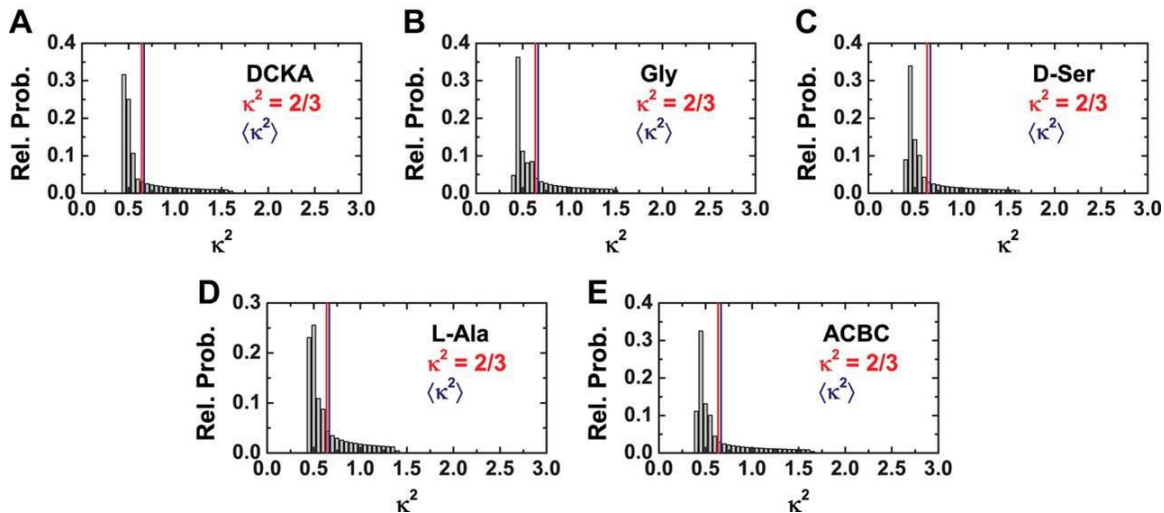


Figure B. κ^2 distribution for LBD bound to: A, DCKA; B, Gly; C, D-Ser; D, L-Ala; and E, ACBC

The line for $\kappa^2 = 2/3$ is shown in red for each distribution. Mean κ^2 is shown in blue.

Table 5. Mean κ^2 and estimated error $\left(\frac{R_{DA}^{(\kappa^2)}}{R_{DA}^{(\kappa^2=2/3)}}\right) \%$ on distances by using the assumption of $\kappa^2 = 2/3$

Sample	$\langle \kappa^2 \rangle$	% Error
Gly	0.636	2.2
D-Ser	0.631	2.5
L-Ala	0.637	1.8
ACBC	0.634	2.5
DCKA	0.641	2.0

The addition of a two-state kinetic transition ($HF \rightleftharpoons MF$) occurring in the submillisecond time scales indicate that D-serine exerted the fastest exchange dynamics ($t_R = 3.5 \mu\text{s}$; **Table 6**), followed by glycine ($t_R = 7.6 \mu\text{s}$) and L-alanine exhibited slower kinetics with $t_R = 50 \mu\text{s}$ (**Table 6**).

Table 6. Fastest relaxation time observed with PDA

Sample	t_R [ms]
Gly	0.0076
D-Ser	0.0035
L-Ala	0.050

The dynamic analysis overall suggests that the full agonists glycine and D-serine have rapid dynamic motions specifically associated with the LBD rapidly fluctuating between the MF and HF states, whereas the partial agonist L-alanine has slower dynamics with occasional visits to the HF state. ACBC and DCKA appear static in the millisecond time scale as shown in **Figure 14**. ACBC has a slightly higher fraction in the HF state relative to DCKA. Note that static populations represent slow exchange at time scales longer than the burst duration, or trapped states. These data, when correlated to the activation profile, suggest that the visits of the LBD to the HF states are critical for the agonist to activate the channel. This is also consistent with the previously published single channel recordings where it has been shown that partial agonists tend to have longer closed times, which would be consistent with the slower kinetics observed for the partial agonists (B9). In addition, when combining the contribution of the static populations and the two-state kinetics between the HF and MF states, we observe that L-alanine is found more often exchanging over these two states more than the two full agonists glycine and D-serine and thus spends less time in the active state. The summary of all population analysis is presented in **Table 7**.

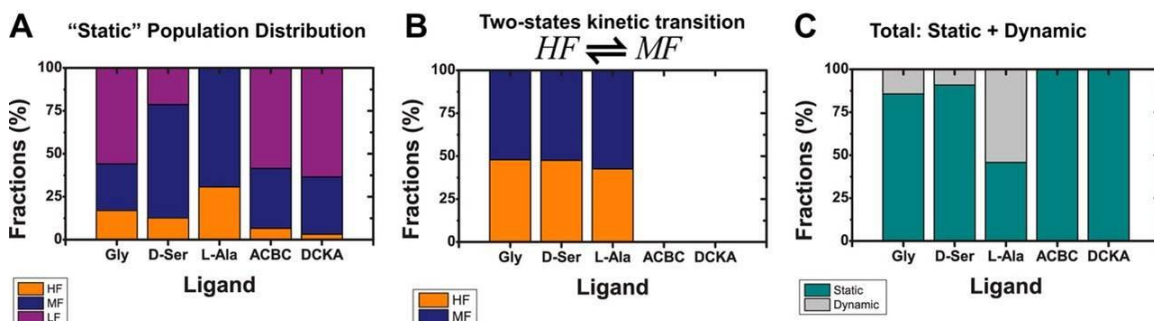


Figure 14. Redistribution of population fractions

A, The population of the static contribution of FRET states. B, A single two-state kinetic state ($HF \rightleftharpoons MF$) was used to model the additional dynamics observed. The bar plot shows the distribution of populations of the HF and MF states. The derived distances for high FRET, medium FRET, and low FRET states are $\langle R_{DA} \rangle_E = 33.9 \text{ \AA}$ (HF), $\langle R_{DA} \rangle_E = 45.8 \text{ \AA}$ (MF), and $\langle R_{DA} \rangle_E = 55.8 \text{ \AA}$ (LF) and are shown by *orange*, *blue*, and *purple*, respectively (**Table 2**). Dynamics fractions were obtained by globally fitting 3 time windows ($\Delta t = 0.5, 2.0$, and 5 ms). DCKA and ACBC do not have dynamic contributions. C, separation of static and dynamic populations that contribute to the overall scheme. L-Alanine is found more often exchanging at submillisecond time scales.

Table 7. Overall fractions of PDA analysis including the donor only (bleached fraction)

Sample	High-FRET (HF)	Medium-FRET (MF)	Low-FRET (LF)	Donor only/ Acceptor bleaching
Gly	59.4	14.4	5.5	20.7
D-Ser	9.7	37	11.1	42.2
L-Ala	13.6	22.8	0.0	63.6
ACBD	3.40	18	30.2	48.4
DCKA	2.0	21.4	40.8	35.8

Discussion

To investigate the mechanism of partial agonism in the GluN1 subunit of the NMDA receptor, we have measured the cleft opening and closing motion of the LBD of the NMDA receptor in the presence of the full agonists glycine and D-serine, the partial agonists L-alanine and ACBC, and the antagonist DCKA. The presence of the ligands redistributed the state populations, indicative of the conformational selection and preferred state. Even in the presence of ligands the LBD showed dynamic sampling of at least three different FRET conformations that could be separated with our FRET measurements. To quantify the dynamics, we used PDA and time window analysis to provide population analysis and relaxation times of exchange rates between

the MF and HF populations. These results show that the LBD when bound to an antagonist spends much of its time in the open-cleft conformation leading to a closed channel. Although there is a significant fraction of the MF state shared in all ligands, it seems that this conformation does not directly lead to activation of the channel.

When comparing the measured FRET distance with the expected distances computed from the AV modeling using the crystallographic structure (PDB code 1PB7) we obtain the experimentally determined MF distances as $\langle R_{DA} \rangle_E = 45.8 \text{ \AA}$, whereas the AV expected distance is $\langle R_{DA} \rangle_E = 48.7 \text{ \AA}$. Thus, we can clearly see that the MF population resembles within 2.8 \AA the crystallographic structure in the presence of ligand. For the DCKA state (PDB code 1PBQ) we experimentally determined a LF distance $\langle R_{DA} \rangle_E = 55.8 \text{ \AA}$ compared with the expected distance of $\langle R_{DA} \rangle_E = 54.2 \text{ \AA}$ from AV simulations. Again, excellent agreement is found with a 1.6 \AA difference.

Moreover, in **Figure 14** one could also observe that, although there are significant changes between various partial agonists and the full agonists, faster kinetics are observed for the full-agonist bound LBD. The relaxation time (t_R) of the glycine-bound LBD is almost an order of magnitude faster than the t_R observed when the LBD is bound to the partial agonist L-alanine. These findings are in good agreement with single-channel recordings that showed longer closed times when bound to partial agonists (139), and faster kinetics is observed for the receptor in the presence of glycine than in the presence of L-alanine. Additionally, the primary three closed states seen in single channel recordings appear to correlate with the three states observed in the smFRET data here, with the HF state being the one more likely leading to channel activation. Thus, the data presented here nicely joins the

experimental structural data seen in x-ray crystallography with the experimental functional data of single-channel electrophysiological recordings to create a unified explanation of the mechanism of partial agonism at the GluN1 LBD.

Chapter 6: Investigation of the Gating Movements of the NMDA Receptor

The previous two chapters discussed the conformational change that occur at the ligand-binding domain that eventually result in channel opening; however, what, if any, are the conformational movements that actually occur at the channel segment itself? For over 30 years, single ion channel recordings have suggested that channel proteins exist in multiple closed and open conformations. As electrophysiological techniques have advanced, the set of ion channel states and our ability to distinguish them have grown to encompass a multitude of long-lived and short-lived shut states (144, 145). Despite the advances in single channel recording approaches, the ability to distinguish transitions between shut states is limited by the fact that these shut states are all electrophysiologically silent. The multiplicity of closed states is not restricted only to single-channel data but has also become increasingly prominent with the rise of cryo-electron microscopy. States previously assumed to be homogenous are increasingly revealed to reflect a variety of underlying conformations (11, 146).

Single molecule FRET of surface-immobilized molecules is uniquely suited to probing of the conformational heterogeneity associated with these predicted closed and open states. NMDA receptors are an ideal candidate for such smFRET studies as they have a rich history of single channel studies with several sound reaction mechanisms involving discrete shut states across multiple time scales (139, 147, 148). Further, there exist a number of full-length structures of NMDA receptors in apo (unliganded), antagonist-bound, and allosteric modulator-bound states (9-12, 149), and NMDA receptor channel gating is relatively slow and thus approaches the temporal resolution of smFRET (120, 150).

Though the available structural information provides excellent insight into the structure-function relationships within the extracellular domains of the NMDA receptor; the transmembrane segments which comprise the ion channel pore itself are less well-resolved, especially in the open-channel configuration. Consequently, structure-function analysis of this region has been more challenging. Past functional studies probing the transmembrane segments have focused primarily on conformational changes between the apo and open states (59, 62), and implicate the disordered linker region connecting the LBD and transmembrane segments as being crucial for coupling. Still unclear though, is whether desensitization or allosteric inhibition themselves induce any conformational rearrangements in the transmembrane segments, or how such conformational changes might be driven by the binding of extracellular agonists and allosteric ligands. Furthermore, most functional studies using macroscopic recordings have, out of necessity, treated the apo, desensitized, and inhibited states as discrete conformations, while single channel analysis reveals each of these classes to be a collection of interconverting states (94, 139, 151). To explore these issues, we have performed smFRET on full-length GluN1/GluN2A NMDA receptors labeled at residue 554 of the GluN1 linker region proximal to the first transmembrane segment, and examined this site in resting (apo), agonist-bound (open and desensitized), and zinc-bound (allosterically inhibited) conditions. This method revealed conformational changes in the transmembrane domain that are associated with channel opening. In addition, we also observed that the receptor occupies multiple closed states that have different kinetic and structural properties under apo, desensitized, and inhibited conditions. These data provide the

first experimental evidence for the range of transmembrane conformations that the receptor adopts and moreover shed light on the structural landscape associated with the functional data. The data also provide the first evidence for differences in the closed channel conformations adopted by apo, agonist-bound, and allosterically inhibited receptors.

Results and Discussion

Functional characterization of the smFRET construct.

To investigate the conformational changes of the NMDA receptor transmembrane domain in various functional states using smFRET, we introduced a fluorophore-labeling site using the mutation F554C in GluN1. Residue 554, found within the linker region connecting the LBD to the first transmembrane segment of the transmembrane domain, was chosen for its accessibility to labeling as well as for minimal expected perturbation of receptor function (**Figure 15a**). To minimize non-specific labelling by donor and acceptor fluorophores (Alexa 555 maleimide and Alexa 647 maleimide, respectively) the accessible cysteines Cys15 and Cys22 in GluN1 and Cys231, Cys399, and Cys460 in GluN2A were mutated to serines, and the resulting background constructs are referred to hereafter as GluN1* and GluN2A*(71-73, 92). Electrophysiological characterization of labeled GluN1*F554C/GluN2A* receptors show that activation, desensitization, and inhibition (**Figure 15b**) are all preserved. Specifically, responses to a 1-ms pulse of 1 mM glutamate with constant glycine in outside-out patches deactivated with a weighted time constant of 43 ± 6 ms ($n = 11$, **Figure 15b**, left). In response to a 5-second long 1 mM glutamate application, the

smFRET construct showed rapid activation (10-90% rise-time, 7 ± 1 ms, $n = 11$) and desensitized to $20. \pm 3\%$ of the peak response with a weighted time constant of 110 ± 20 ms ($n = 11$, **Figure 15b**, left). Furthermore, the channel block by both MK-801 (1 μ M, $93 \pm 2\%$ steady-state inhibition, $n = 8$, **Figure 15b**, middle) and inhibition by Zn^{2+} (10 μ M, $83 \pm 5\%$ steady-state-inhibition, $n = 5$, **Figure 15b**, right) were intact in whole cell recordings.

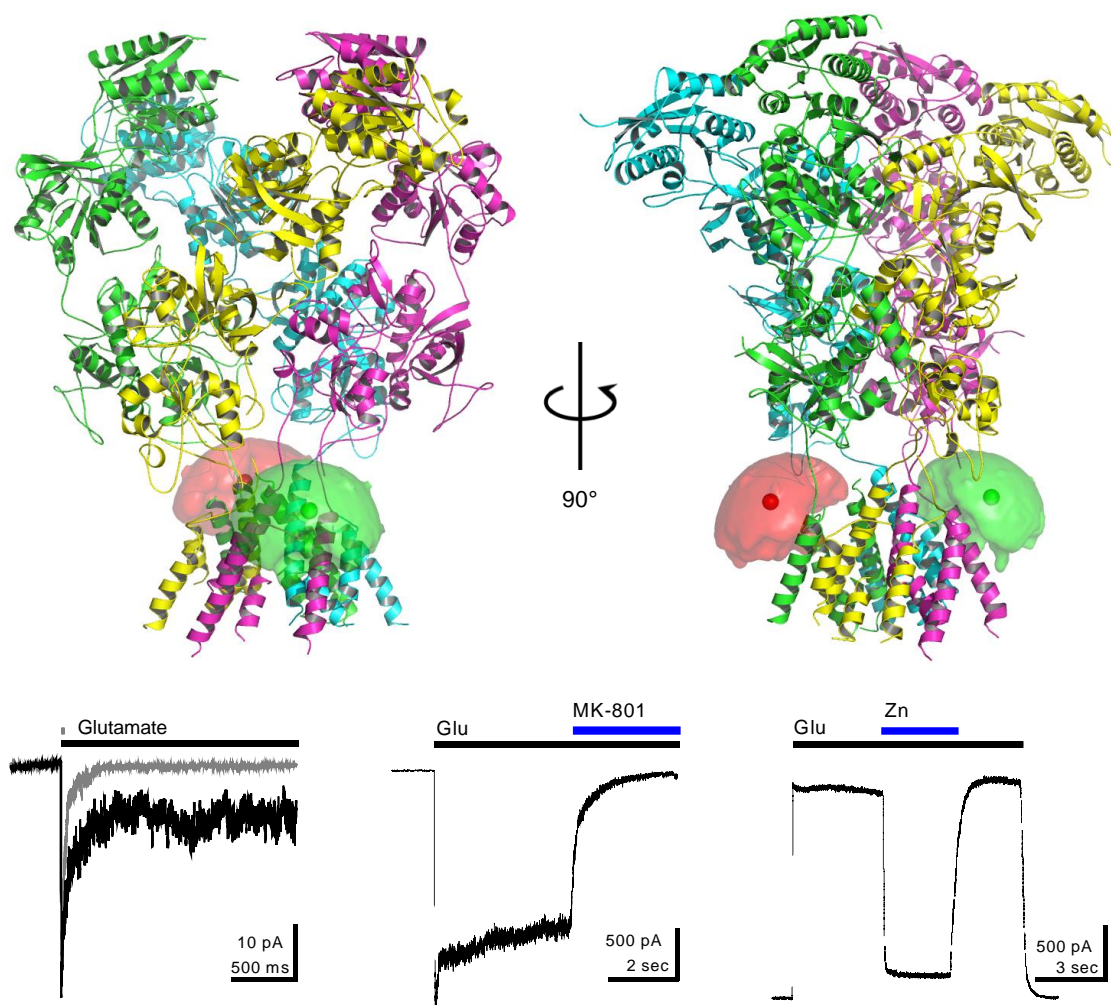


Figure 15. TMD smFRET constructs and characterization

A, GluN1*F554C/GluN2A* NMDA receptors were labeled with donor and acceptor fluorophores at site 554 of GluN1, proximal to the first transmembrane segment of GluN1 (mean fluorophore positions shown as green or red hard spheres surrounded by a fluorophore cloud). B, Representative electrophysiological responses from the smFRET construct showing deactivation (gray) and desensitization (black) (left), inhibition by 1 μ M MK-801 (middle), and by 10 μ M Zn^{2+} (right, recorded at +50 mV).

smFRET identified distinct and stable states.

For smFRET experiments, GluN1*F554C/GluN2A* receptors were recombinantly expressed in HEK cells, labelled with donor and acceptor fluorophores, and purified using *in situ* immunopurification on prepared coverslips (152) (see Appendix). As with prior experiments using soluble iGluR domains (89, 90, 132, 133), sample scanning confocal microscopy showed clearly resolved single spots on these coverslips which were not present when unmutated GluN1*/GluN2A* was used (**Figure 16**). Single molecule FRET trajectories were collected from these full-length labelled GluN1*F554C/GluN2A* receptors under various liganded conditions, and the resulting ensemble-averaged denoised FRET efficiency histograms are shown in **Figure 17**. The raw trajectories were denoised using wavelet decomposition and specific states were identified using Step Transition and State Identification (STaSI) analysis (89, 153, 154) (**Table 8**, **Figure 17** insets). STaSI analysis was performed independently per ligand dataset, and the discrete states identified through STaSI were supported by fitting the ensemble observed FRET efficiencies to a sum of Gaussians corresponding to those states (89)(**Figure 18**).

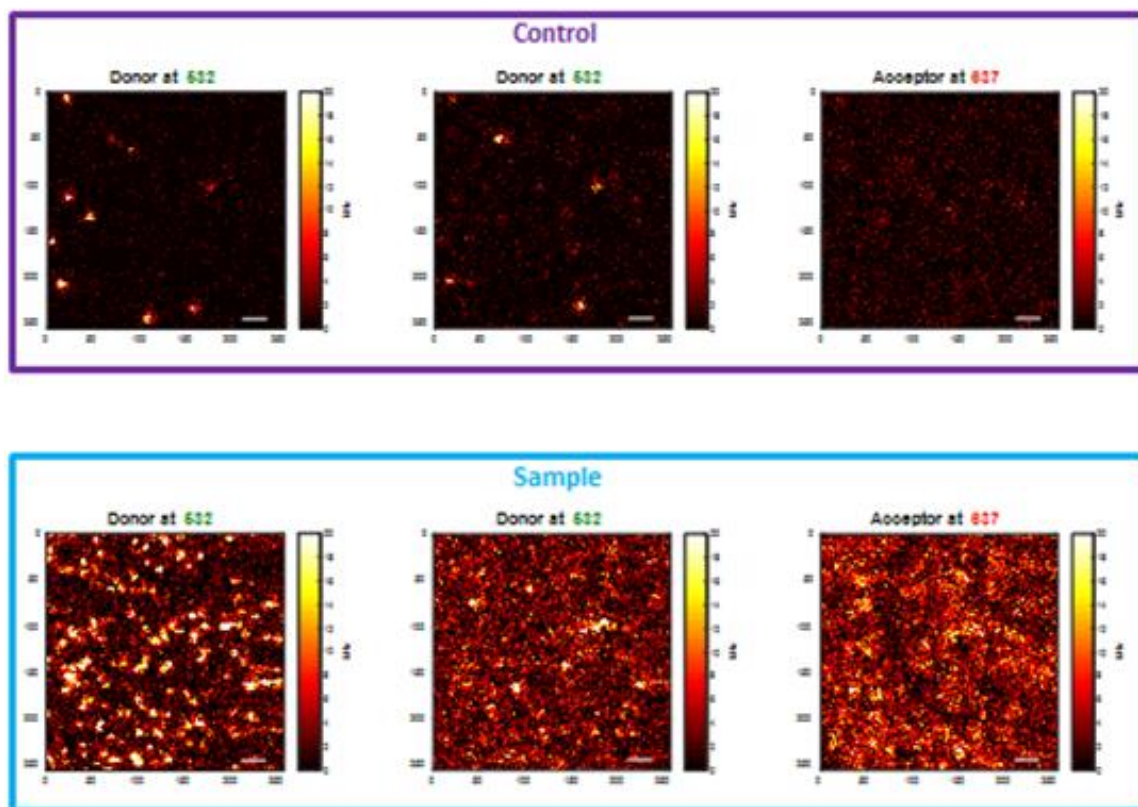


Figure 16. Attached-FRET of full-length NMDA receptors shows specific pulldown

Control slides showing minimal fluorescent protein when labeling cells expressing background NMDA receptors (top panel) and with FRETting single molecules with the F554C construct.

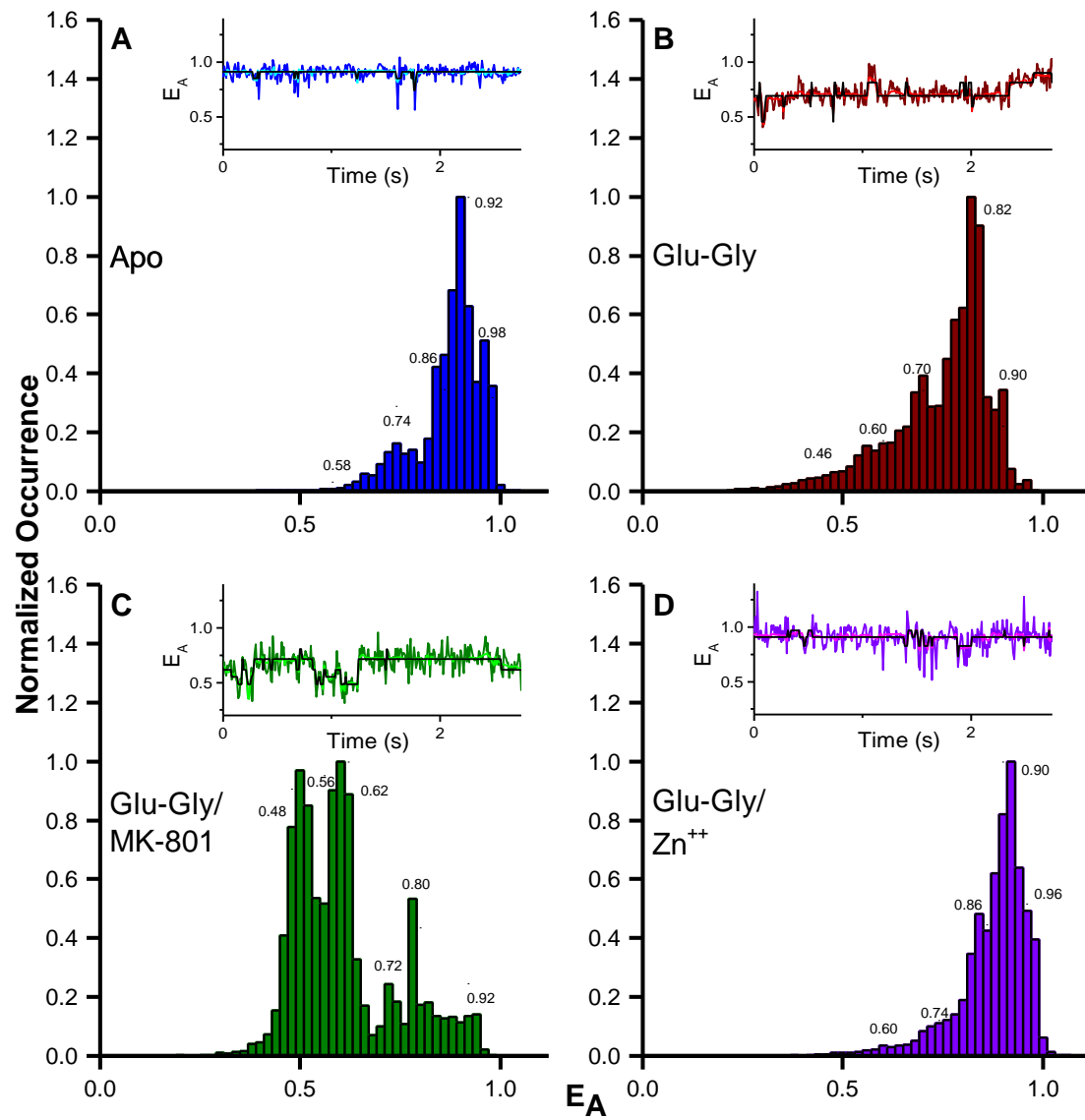


Figure 17. Denoised smFRET histograms of the NMDA receptor

smFRET data of the NMDA receptor were obtained under varying ligand conditions, denoised via wavelet decomposition (154, 155), and used to generate smFRET efficiency histograms. STaSI analysis was performed to reveal the underlying conformational states. Peaks corresponding to each STaSI state are labeled with the state efficiency. The STaSI states represented by Gaussian noise fitting to the observed FRET histogram can be seen in **Figure 18**. Shown in an inset above each histogram is a representative observed efficiency trace, the denoised trace (lighter shade), and the STaSI fit (black). The different conditions studied were *A*, the apo, unliganded receptor *B*, the agonist-bound (Glu-Gly) receptor *C*, the agonist-bound receptor in the presence of the open-channel blocker MK-801, and *D*, the agonist-bound receptor inhibited by the allosteric inhibitor zinc. The high-efficiency state seen in *A* indicates a closed-channel conformation for an apo receptor not seen with the agonist-bound receptor. The increased populations of the low efficiency states in *C* identify those states as representing open-channel conformations. The reappearance of the high-efficiency state in *D* implies that zinc modulation proceeds not simply by stabilizing desensitized conformations, but by decoupling the cleft-closure of the agonist-binding domain to conformational changes of the transmembrane segments.

Table 8. Conformational states sampled by the NMDA receptor under various liganded conditions.

Conformational states were identified using Step Transition and State Identification analysis (89, 153). Distances for the states were calculated with an R_0 of 51 Å. There is a high degree of similarity among the states seen, as may be expected of a conformational selection model sampling the same states at different populations.

Functional Assignment	Apo			Glutamate-Glycine			Glutamate-Glycine/MK-801			Glutamate-Glycine/Zn ²⁺		
	States	Percent Occurrence	FRET distance (Å)	States	Percent Occurrence	FRET distance (Å)	States	Percent Occurrence	FRET distance (Å)	States	Percent Occurrence	FRET distance (Å)
Open				0.46 ± 0.02	7.1	52 ± 1	0.48 ± 0.02	23.6	52 ± 1			
Open							0.56 ± 0.02	24.8	49 ± 1			
Open	0.58 ± 0.02	1.6	48 ± 1	0.60 ± 0.02	9.2	48 ± 1	0.62 ± 0.02	26.0	47 ± 1	0.60 ± 0.02	4.3	48 ± 1
Closed	0.74 ± 0.02	14.6	43 ± 1	0.70 ± 0.02	18.4	44 ± 1	0.72 ± 0.02	8.0	44 ± 1	0.74 ± 0.02	5.6	43 ± 1
Closed	0.86 ± 0.02	17.4	38 ± 1	0.82 ± 0.02	53.4	40 ± 1	0.80 ± 0.02	11.3	40 ± 1	0.82 ± 0.02	20.5	40 ± 1
Closed	0.92 ± 0.02	50.3	34 ± 2	0.90 ± 0.02	11.8	35 ± 1	0.92 ± 0.02	6.4	34 ± 2	0.90 ± 0.02	45.9	35 ± 1
Closed	0.98 ± 0.02	16.0	27 ± 5							0.96 ± 0.02	23.7	30 ± 3

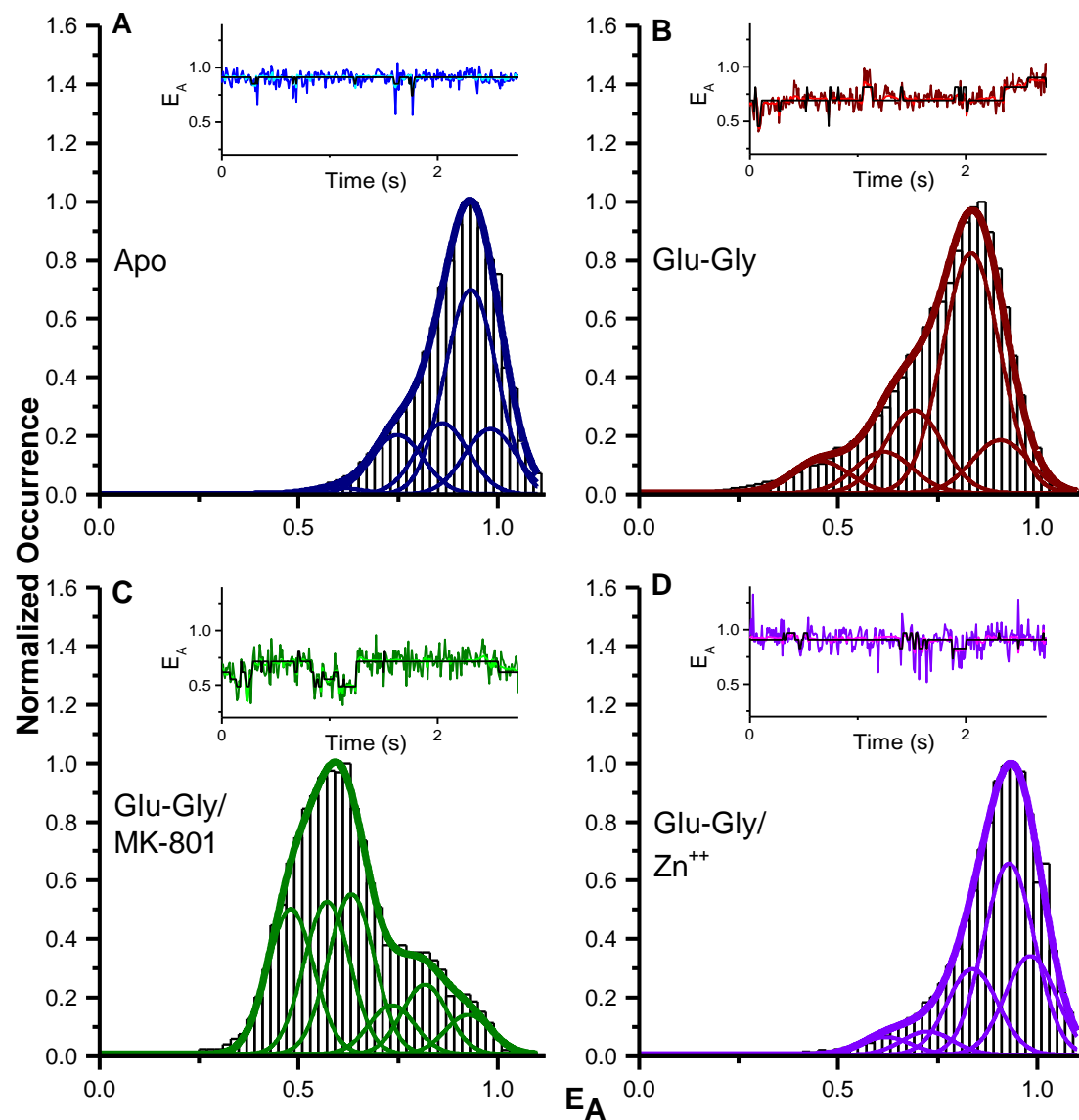


Figure 18. Observed smFRET histograms of the NMDA receptor

Ensemble histograms of the observed data are shown. The STaSI states are shown here, represented as Gaussian noise, whose sum fits well with the observed histogram. *A*, Apo receptor *B*, agonist-bound receptor *C*, agonist-bound receptor with MK-801, *D*, zinc-inhibited receptor.

The conformational landscape associated with open and closed channel states.

To evaluate the difference between closed and open channels, we compared the histogram obtained in apo conditions with the histogram obtained under saturating concentrations of agonist (1 mM glutamate and 1 mM glycine, **Figure 19a and b**). The histogram of the apo NMDA receptor (**Figure 17a**) shows five discrete states, with the predominant state (50.3% occupancy) at a FRET efficiency of 0.92 ± 0.02 . The glutamate-glycine bound histogram (**Figure 17b**) also shows five states; however, the receptor occupancy distribution is shifted toward the lower efficiency states. In particular, the glutamate-glycine states with FRET efficiencies of 0.46 ± 0.02 and the 0.60 ± 0.02 states are rarely observed with the apo receptor (1.6% occupancy at 0.58 ± 0.02 with no observed population corresponding to the 0.46 ± 0.02 state). This shift toward lower efficiencies when glutamate-glycine are bound suggests that channel opening is accompanied by a widening of the top of the transmembrane domain. Given that unliganded, apo receptors show no spontaneous channel opening in the absence of ligands, we assigned the FRET efficiency states at 0.46 ± 0.02 and 0.60 ± 0.02 to open channel conformations with the rest of the states corresponding to closed conformations. To validate this assignment, we employed MK-801, an open-channel blocker that binds to and stabilizes the channel's open conformation (156). Inclusion of MK-801 along with glutamate and glycine should increase the relative proportion of the open-channel conformational states and reduce the relative proportion of the closed-channel conformational states. Consistent with this, the ensemble smFRET histograms show a notable shift toward lower FRET efficiencies (**Figure 17c, Figure 19c-f, Table 8**). STaSI analysis of the data revealed six states with

MK-801, five of which align with the states for the glutamate-glycine bound receptor (**Table 8**). Of these five states, the 0.48 ± 0.02 and the 0.62 ± 0.02 states seen with MK-801 have higher relative occupancies compared to their counterparts in the glutamate-glycine-bound receptor. MK-801 also stabilizes an additional state at 0.56 ± 0.02 , which is unexplored or highly transient in its absence. This smFRET-based assignment of states as functionally open is reinforced further by the agreement between the smFRET 'open' state occupancy (16.3% in the liganded condition, **Table 8**) and the residual steady-state current after desensitization ($20 \pm 3\%$ of peak response, $n = 11$) in our electrophysiological measurements of the smFRET construct (**Figure 15b**).

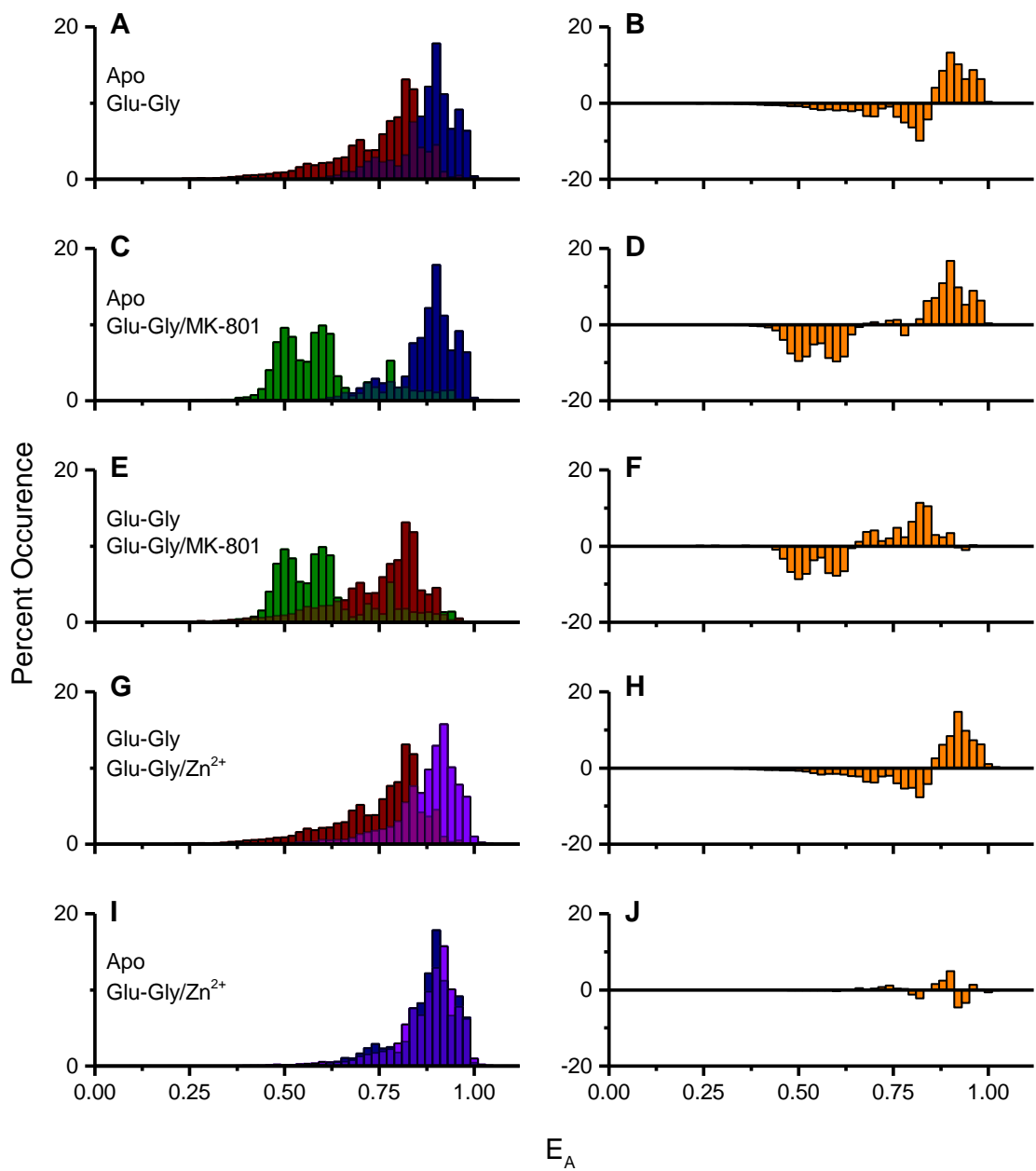


Figure 19. Difference histograms clarify the changing conformational landscape of the NMDA receptor as it shifts between inactive and active conditions

Parent denoised FRET efficiency distribution histograms were paired and subtracted from one another to generate difference histograms. The positive/negative value of the difference histogram signifies higher/lower relative abundance of one condition as compared to the other. Shown are the parent and difference histograms for *A,B*, apo vs. glutamate-glycine-bound receptor, *C,D*, apo vs. glutamate-glycine with MK-801, *E,F*, glutamate-glycine vs. glutamate-glycine with MK-801, *G,H*, glutamate-glycine vs. glutamate-glycine with zinc, and *I,J*, and Apo vs. glutamate-glycine with zinc.

Consequently, the three higher-efficiency states explored by the glutamate-glycine-bound receptor (0.70 ± 0.02 , 0.82 ± 0.02 , 0.90 ± 0.02) can be assigned to closed-channel conformations. Their distances of $44.3 \pm 0.7 \text{ \AA}$, $39.6 \pm 0.9 \text{ \AA}$, and $35 \pm 1 \text{ \AA}$, respectively, between the fluorophores are in good agreement with the X-ray and EM-based structures of the closed-channel receptor, which show a C α -C α distance of 30 \AA . Additionally, the distance change of $17 \pm 1 \text{ \AA}$ between the most closed state (0.90 ± 0.02) and the more open state (0.46 ± 0.02 efficiency, $52.4 \pm 0.7 \text{ \AA}$) is similar to the 22 \AA change at the M3 helix between the closed-channel EM structure and the low-resolution EM structure thought to represent the open receptor(11).

The apo receptor additionally explores an additional high-efficiency state at 0.98 ± 0.02 ($27 \pm 5 \text{ \AA}$) (**Figure 17a, Table 8**). This closed state has no corresponding equivalent in the glutamate-glycine bound receptor or with the glutamate-glycine receptor with MK-801, but rather this state is unique to the apo, unliganded state. Because cleft closure of the LBD leads to channel opening at the transmembrane domain *via* the linker between them (59), this high-efficiency state of the apo receptor most likely arises from a lack of tension at that linker due to the absence of ligand in the agonist-binding cleft. That this state is not the predominantly populated closed state is reflective of the ability of LBD to dynamically sample closed-cleft conformations in apo and even antagonist-bound conditions (90, 91, 135).

Comparison of desensitized and inhibited NMDA Receptor.

To obtain a fuller understanding of the gating motions of the NMDA receptor, we also examined the accessible conformational states of the transmembrane domain

in the presence of the divalent cation zinc, which acts as an allosteric inhibitor (71, 73, 151). Like other allosteric inhibitors, zinc binds to the amino-terminal domain of GluN2 subunits, inducing cleft closure and a reduction in channel activity (11, 12, 71, 73, 149, 151, 157), though the precise nature of the conformational changes that occur at the transmembrane segments upon zinc binding are still unknown. **Figure 17d** shows the ensemble histogram of the denoised FRET data, which are primarily shifted toward more closed states as compared to the state of the agonist-bound receptor alone (**Figure 19g and h**). However, in addition to stabilizing the agonist-bound closed states, another high-efficiency, more closed state is observed at 0.96 ± 0.02 (**Figure 17d, Table 8**), which is structurally distinct from the closed states probed with glutamate and glycine. The efficiency of this more closed state in the presence of zinc is similar to the 0.98 ± 0.02 state observed in the apo form of the receptor (**Figure 17a, Table 8**), and in fact their histograms are remarkably similar (**Figure 19i and j**). Thus, rather than simply shifting the conformational equilibrium of the glutamate-glycine-bound receptor toward its closed states, as has been previously suggested, the binding of zinc results in the more compact “apo-like” state of the receptor’s transmembrane segments. These data suggest that allosteric inhibition by zinc may occur through a mechanism in which amino-terminal domain cleft closure allows for the decoupling of the extracellular domains from the transmembrane segments, permitting the transmembrane segments to move to more closed conformations.

Dynamics of the NMDA receptor.

Beyond providing the conformational landscape that the NMDA receptor probes, our smFRET data also provide insight into the dynamics of the receptor. The smFRET traces under apo conditions were relatively static (**Figure 17a, inset**), whereas the traces of the liganded receptor were much more dynamic (**Figure 17b, inset**). To quantify the differences in transition frequency, we first examined the average number of transitions occurring in time-windows of varying length for each condition (**Figure 20a**), which confirm that the apo condition indeed exhibited a much lower average number of transitions than receptors in other conditions. Interestingly, the allosterically inhibited zinc-bound form of the receptor exhibits a comparable number of transitions to the other liganded conditions, despite being electrically less active and with an overall histogram reminiscent of the apo condition. These transitions of the inhibited receptor, however, are primarily between the highest-efficiency closed states, as discussed later. Such behavior is reminiscent of single-channel recordings, which display long-lived shut states interspersed with clusters of electrical activity (158). As a second measure of conformational fluctuation, the cumulative probability plot of the coefficient of variation (CV) of each single molecule trajectory is shown in **Figure 20b**. Static, stable traces exhibit low CV, whereas dynamic traces exhibit a higher CV. As with the average transitions over time, apo receptors show much less variation and the cumulative probability rises quickly at a low CV value. In contrast, a much larger portion of the agonist-bound and MK-801-bound traces show higher variation and so the rise is slower. Zinc-inhibited receptors, on the other hand, though they undergo as many transitions as do the other liganded

receptors (**Figure 20a**), show a steeper rise, intermediate between the glutamate-glycine and the apo receptors. As described below, this behavior is consistent with the zinc-bound receptors exhibiting transitions between a smaller range of states, fluctuating mainly among the closed states, and rarely visiting open states.

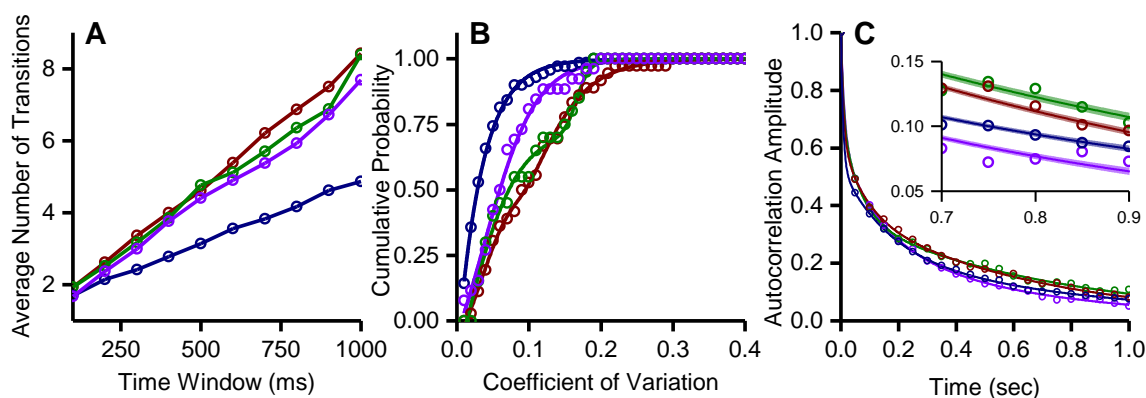


Figure 20. Dynamics of the NMDA receptor show differences in transitional behavior under different ligand conditions

A, The average number of transitions seen per time window show that unliganded apo receptors exhibit notably fewer transitions than any of the liganded receptors. B, The cumulative probability plot of the coefficient of variation shows that the apo receptor is the most unvarying of the receptors, with few transitions. Zinc-inhibited receptors show a higher level of variation, while the uninhibited glutamate-glycine bound receptors show a high degree of variation. **Figure 21** shows that this relationship is not due to effects of the length of the individual traces. C, Autocorrelation of the single molecule data fit to three-term exponential decay. The thickness of the lines represents the fitting errors (zoomed in for visibility in inset). The lifetimes show that uninhibited glutamate-glycine bound receptors have a higher amplitude of the longest-lived component, as well as a longer weighted average lifetime, as compared to the apo and inhibited receptors, indicating increased transitions for uninhibited receptors and increased rigidity for the apo and inhibited receptors.

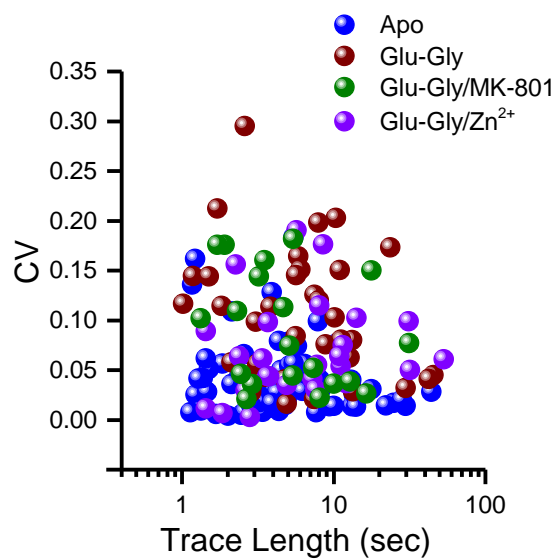


Figure 2I. The coefficient of variation (CV) of each smFRET efficiency trajectory versus that trajectory's length

Having various lengths of the smFRET trajectories does not affect the CV-ligand condition relationship.

As a final measure to examine the transmembrane domain rigidity, the autocorrelation of each of the smFRET trajectories was calculated to generate an average autocorrelation curve for each set of ligand conditions. The average autocorrelation curves were fit to a three-term exponential decay, and the exponential fits yielded three different fluctuation timescales for each receptor condition: short (τ_1), intermediate (τ_2), and long (τ_3) (**Figure 20c and Table 9**). Short autocorrelation decay times indicate a more rigid nature of the molecules, whereas longer decay times indicate the opposite (132). The process associated with the longest timescale (τ_3) can be attributed to conformational transitions or protein fluctuation events (159). As expected, apo and inhibited receptors have smaller amplitudes for this timescale, whereas agonist-bound NMDA receptors have the greatest amplitude for this timescale. Furthermore, the trend in overall weighted average fluctuation timescales indicates that the liganded receptors exhibit a longer overall decay compared to the apo and inhibited receptors, again reflecting the greater stability of electrically inactive receptors under these conditions.

Table 9. Autocorrelation data under the various ligated conditions.

The average autocorrelation decay of the single molecule FRET data was fit to a three-term exponential decay, resulting in short, intermediate and long timescale decays for each condition. The longest timescale decay was most prevalent for uninhibited liganded receptors, and was least prevalent for the apo and inhibited receptor. These data indicate that uninhibited receptors exhibit the most transitions, indicative of a shallow energy barrier into channel opening, whereas apo and inhibited receptors are the most rigid, with a high energy barrier preventing transitions into channel opening.

Ligand	Short timescale τ_1 (ms)	Amplitude (%)	Intermediate timescale τ_2 (ms)	Amplitude (%)	Long timescale τ_3 (ms)	Amplitude (%)	Weighted average lifetime τ (ms)
Apo	8 ± 1	46.4 ± 0.7	170 ± 10	30 ± 1	860 ± 60	23 ± 2	250 ± 20
Glu-Gly	9 ± 3	37 ± 1	82 ± 6	24.3 ± 0.9	650 ± 10	38.9 ± 0.7	275 ± 6
Glu-Gly/ MK-801	9 ± 1	309 ± 2	65 ± 5	34 ± 2	740 ± 20	35.9 ± 0.6	292 ± 9
Gly-Gly/ Zn^{2+}	13 ± 1	39 ± 1	150 ± 10	34 ± 2	640 ± 40	26 ± 2	220 ± 20

Transitions among the open and closed states.

The smFRET trajectories further allow us to determine the transitions between and among the closed and open states. Transition maps showing the relative number of transitions from one state to the other are shown in **Figure 22a-d**. The data show that transitions primarily occur between states of nearest FRET efficiency, whereas transitions between non-adjacent states are less common. More importantly, the transition maps for the receptors that show significant open-channel states (**Figure 22b and 22c**) suggest that channel opening occurs from a single closed state—a pre-open state—which has the lowest FRET efficiency among the closed states. The two other closed states, which have a higher FRET efficiency and thus more closed transmembrane segments, do not show significant direct transitions into an open channel state. Thus, a linear mechanism connecting the three closed states to the two open states best describes the observed transition maps. Such a mechanism has a striking similarity to the mechanism proposed based on single channel analysis which show several closed states interconverting, but a single closed state transitioning to an open state (151). Based on the present results, we can say that this ‘pre-open’ closed state is structurally more open than the other closed states. Additionally, due to the dynamics and the fact that both glutamate and glycine are present, the two other closed states for the glutamate-glycine bound receptor can be assigned to the slower closed states observed in single-channel recordings (151). Thus our data are able to provide the first direct correlation between structural changes in the transmembrane segments and functional changes previously reported using single-channel methods. Furthermore, our results allow us to place these states along a plausible structural

reaction coordinate corresponding to the functionally relevant distinction between open and closed.

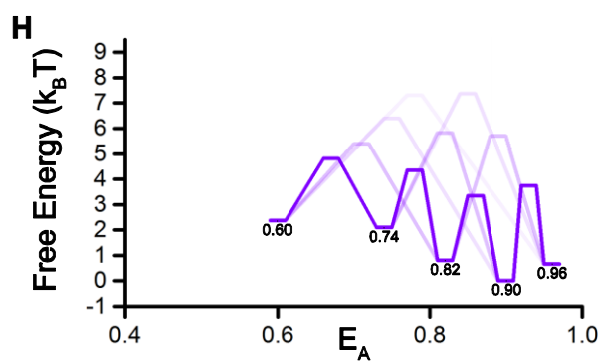
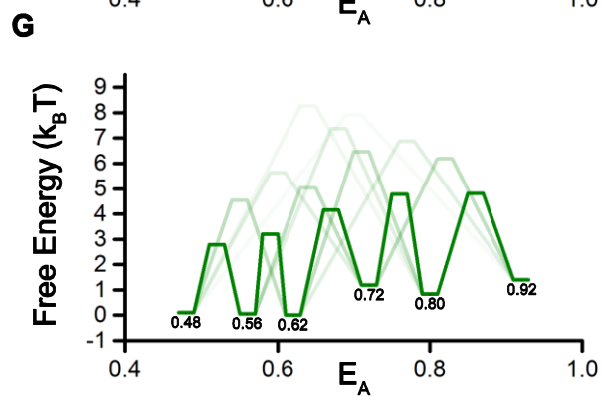
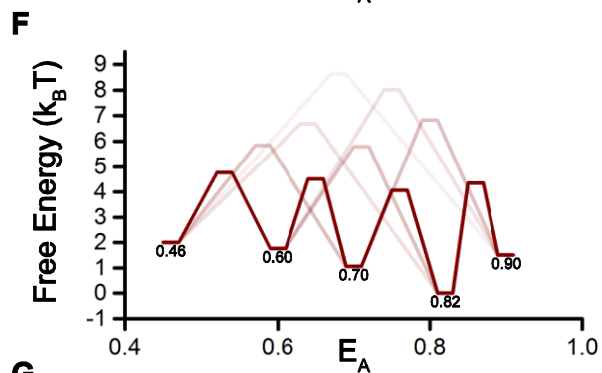
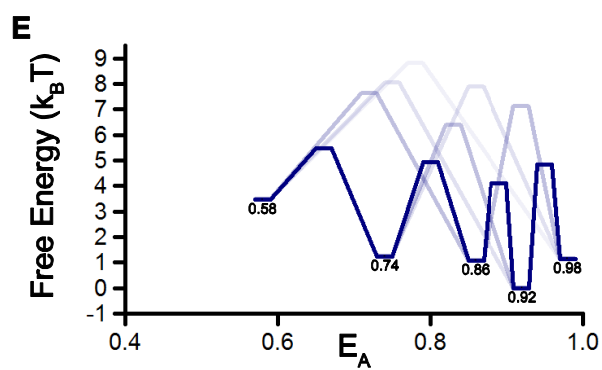
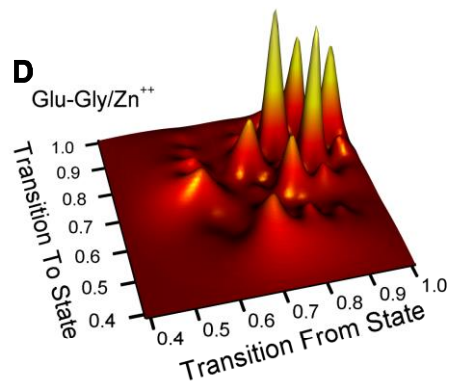
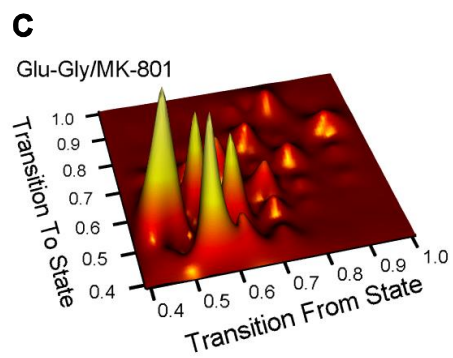
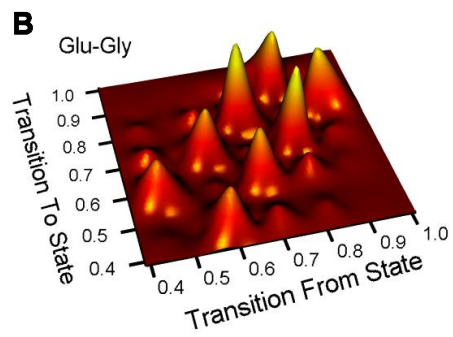
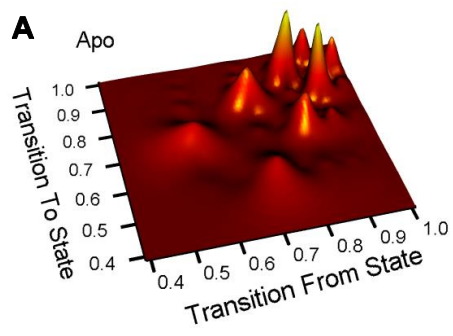


Figure 22. Transition maps and free energy diagrams of the NMDA receptor smFRET data

Examination of the individual single molecule traces show primarily transitions between adjacent states, portrayed here in terms of the normalized number of transitions for *A*, apo, *B*, glutamate-glycine bound, *C*, glutamate-glycine-bound with MK-801, and *D*, glutamate-glycine-bound zinc-inhibited NMDA receptors. This pattern indicates an ordered movement from closed to open conformations. *E-H*, Data from these transition maps were used to generate free energy diagrams. These energy diagrams explain the kinetic behavior we see in the receptor, with stabilization of the open states for agonist-bound receptors and a high activation energy barrier for apo receptors.

Energetics of the NMDA receptor.

Based on the distribution of states (**Figure 17a-d, Table 8**) and the transition maps (**Figure 22a-d**), the relative free energies of open and closed states along with the relative free energy barriers for transitions between pairs of states were calculated (160) (**Figure 22e-h**). These smFRET-derived data are again strikingly similar to the free energy profiles proposed based on functional single-channel recordings (151), though with our data showing a higher free energy for the open states of the agonist-bound receptor, consistent with the desensitization profile of our smFRET construct (**Figure 15b**). These energy profiles support our conclusion that the resting apo receptor remains primarily in closed conformational states with a high activation energy between states and thus fewer transitions. The zinc-inhibited receptor also occupies primarily closed states, but the relative lower activation energy between the states allows the zinc-inhibited receptor to exhibit more transitions than apo. The ability of uninhibited agonist-bound receptors to activate the ion channel can be seen by the lower activation energies between the pre-open closed states and the open states, facilitating transitions between them.

Concluding remarks.

Here we have used single molecule FRET to examine the conformational landscape of full-length intact NMDA receptors under various liganded conditions. Our analysis revealed a multiplicity of FRET states in each dataset. The smFRET data show similar efficiencies between different liganded conditions but with different occupancies, consistent both with functional studies using single channel recordings

and with the model of conformational selection at the level of the transmembrane domain. Agonist binding lowers the energy barrier preventing the transitions of the apo receptor, allowing the glutamate-glycine bound receptor to explore the open-state conformations whilst destabilizing the tightest closed-state arrangement. Our studies also show for the first time that the binding of the allosteric modulator zinc inhibits the NMDA receptor by lowering the energy barrier of the glutamate-glycine bound receptor leading into the apo-like tightest closed-state arrangement, essentially decoupling the closed-cleft tension of the LBDs from the transmembrane segments.

Chapter 7: Conclusions and Future Directions

The work presented in this dissertation has made great strides toward understanding the mechanisms of action of the NMDA receptor. Prior to this work, the mechanism of partial agonism of the NMDA receptor glycine-binding domain was unknown. Here, we combined cutting edge unnatural amino acid technology along with single molecule FRET in order to reveal a variant of the graded cleft closure seen with AMPA receptors (90). Due to the lower temporal resolution of the attached-FRET technique used, we pushed the boundary even further to achieve submillisecond resolution of the dynamics of the glycine-binding domain (91). The data we obtained are highly consistent with work from other groups, showing broad energy wells for the apo LBD (135) and higher energy barriers relative to glycine for partial agonists (139). Moreover, we were able to confirm a conformational selection-based mechanism of the GluN1 LBD wherein the LBD can choose among three distinct conformational states, with two of these states being consistent with crystal structures (4). Where our work has stood out, though, is the revelation of the third state, hitherto unknown, that we propose would lead directly into channel activation. Similarly, we have made unprecedented advances in exploring the conformational dynamics of the transmembrane domain of the NMDA receptor. Again, our data shows great consistency with previous work (151), but the insight revealed by our studies has allowed us to put forth a new mechanism by which NMDA receptors are allosterically regulated.

This type of biophysical understanding of the NMDA receptor is of critical importance. As discussed in Chapter 1, NMDA receptors play a whole host of roles

within, and even outside of, the central nervous system. Physiological function is tied to almost every cognitive process, and pathological dysfunction can be seen in a whole host of disorders. In order to treat these disorders, a complete biophysical understanding of these receptors is necessary for the development of better therapies that can target aberrant receptors whilst minimally affecting those that are properly functioning. Work from our lab has already made some ground toward this goal (161), as has the work of others (56). With the knowledge gained from the studies presented in this dissertation, such progress can be made again.

Future Directions

Despite the great progress made here, there is still much more work to do. The NMDA receptor still hides many mysteries, and the abilities and techniques of our lab are uniquely poised to address and answer some of the most critical among them.

Further investigations into the LBD

The works performed here on the LBD were performed on isolated domains; however, recent technological advancements in the field and in our own lab have made single molecule investigations of full-length proteins an achievable goal. As discussed in their chapters, the flexibility seen in an isolated domain may not be realized in the context of a full-length receptor, and so the dynamics observed for the LBD may be quite different when approached in this manner. Indeed many LBD interactions and properties depend on the presence of the rest of the protein, such as desensitization, allosteric modulation, and intersubunit cooperativity (162). With our

new ability to study the full-length receptor, the dynamics of the ligand-binding domain must be revisited to see how the domain changes and reacts to a variety of different conditions.

Dynamics of the Amino-Terminal Domain

The amino-terminal domain is unique among the iGluRs for its rich allosteric potential, and the recent full-length structures have given insight into why, with its extensive interface with the LBD (9, 10). Our work has already begun on this, with the revelation of a zinc-mediated decoupling of the LBD to the TMD, but now a more targeted look at the ATDs is essential. Does ifenprodil act in the same way? And how does spermine potentiate—if the inhibitors decouple, what would be the opposite of that? Moreover, even beyond allosteric ligands, the ATDs themselves impart different properties on the receptor. A look at the dynamics of chimeric receptors would reveal a great number of insights into how these domains exert their effects.

A closer look at the pore

The work presented here was a great leap forward, but now many smaller steps need to be taken. Probing the TMD via the GluN2 subunits is a logical next step, as is looking at the movements from the intracellular side. To really make the greatest progress forward, however, two future goals should be strived for. The first is single molecule patch-clamp FRET microscopy, and the second is single-molecule FRET guided molecular dynamics. With single molecule patch-clamp FRET microscopy, entailing the simultaneous acquisition of electrophysiology and single molecule FRET

data, the distinct conformational states that we saw in Chapter 6 can now mapped to the different functional kinetic states. Temporal resolution of the attached-FRET studies performed in that chapter have been the limiting factor, but the ability to probe submillisecond ranges as described in Chapter 5 show that this is not an insurmountable barrier. Certain technological advances and innovations may need to be developed before such a union can be reliably called upon, the gain that will be obtained from it will be immense.

Molecular dynamics and single-molecule FRET seem to me to be a natural marriage of two techniques. Single molecule FRET can provide experimental verification and guidance, while molecular dynamics will be able to provide atomic-level insight into the motions of the protein. Such a marriage becomes especially with proteins such as the NMDA receptor because, due to its sheer size, modeling of the entire receptor would be a great computational burden. Single molecule FRET data can thus provide constraints and an idea of the forces needed to direct a protein to undergo a particular transition the experimenter wants to see. Conversely, the necessity of labeling makes visualizing certain areas quite difficult via smFRET, *e.g.* the inner lining of the pore. By combining our single molecule FRET data with steered MD, I suspect a visualization of the permeation pathway, as well as the molecular determinants of conductance, permeability, uncompetitive blocking, etc., are not far off.

The Carboxyl-Terminal Domain

The CTD is like the red-headed stepchild of the iGluR domains. It is the least well-studied structurally, but despite that, or perhaps even because of it, the CTD in recent years has come to be known to harbor many surprising and unexpected secrets. CTD-mediated metabotropic activity of the NMDA receptor is an exciting, if controversial, field that needs to be explored much more thoroughly. The intrinsically disordered nature of the domain may provide problems for crystallographers and cryo-EM microscopists, but it fits right into the wheelhouse of smFRET. Indeed, FRET has already been used to explore these CTD motions (115), albeit with lower precision due to the use of fluorescent proteins rather than dyes. Insights from single-molecule studies can greatly clear up the mechanism of CTD-mediated non-ionotropic function.

Better technologies to study membrane proteins

Membrane proteins like the NMDA receptor make up about 30% of the proteome and over 50% of drug targets, but structural and biophysical characterization of these proteins are often hindered by that very membrane that makes them so important. Current purification methods of membrane proteins typically consist of ripping those proteins from the membrane and transferring them into an unstable detergent micelle. Even if purified protein is subsequently reconstituted into a lipid vesicle or a membrane scaffold protein (MSP) nanodisc, there is often no guarantee that the lipids the protein is reconstituted in is representative of the lipids in which the protein natively. Recently, styrene-maleic acid copolymers have come into use as a means by which to solubilize membrane proteins.

Rather than simply removing the lipids from the protein, these SMA copolymers extract nanodiscs from lipid bilayers, taking any embedded membrane proteins along with them (163). The advantage of these “native nanodiscs” over MSP-based nanodiscs would be that the native annular lipids that surround the protein would be intact. Because the proteins have not been ripped away from lipids, proteins in these native nanodiscs are more thermostable (164, 165) and retain function (164, 166). Not only can individual proteins be purified, but complexes as well (167). Finally, a crystal structure of an SMA-solubilized protein has recently been published, proving the ability of SMA copolymers in the use structural work. The authors note no obvious differences between the SMA-solubilized and traditional detergent-solubilized structures, but take care to state that the use of SMA may obviate the necessity for detergent screening and may facilitate working with more difficult membrane proteins (168). In all, the advent of the SMA copolymer has made this is an exciting time for membrane proteins and those who study them.

Final Thoughts

NMDA receptors are fascinating proteins that play pivotal roles in cognitive function. The work presented in this dissertation has made great headway into understanding the structure-function relationships of this protein, but much more remains to be done. Fortunately, new technological advances and approaches are coming out every day to help us delve into the mysteries that underlie, not only the NMDA receptor, but life itself.

Appendix: Materials and Methods

Parts of this section are based upon research originally published in *The Journal of Biological Chemistry*. Dolino, D. M., D. Cooper, S. Ramaswamy, H. Jaurich, C. F. Landes, and V. Jayaraman. Structural Dynamics of the Glycine-binding Domain of the *N*-Methyl-D-Aspartate Receptor. *Journal of Biological Chemistry*. 2015; 290: 797-804. © the American Society for Biochemistry and Molecular Biology. and Dolino, D. M., S. Rezaei Adariani, S. A. Shaikh, V. Jayaraman, and H. Sanabria. Conformational Selection and Submillisecond Dynamics of the Ligand-binding Domain of the *N*-Methyl-D-aspartate Receptor. *Journal of Biological Chemistry*. 2016; 291: 16175-16185. © the American Society for Biochemistry and Molecular Biology.

Generation of site-directed isolated GluN1 LBD mutants

A pET22B vector encoding the rat GluN1 isolated LBD was provided by Eric Gouaux (Oregon Health and Science University, OR) (4). Sites were chosen based on accessibility and distance across the cleft. S507 and T701 (**Figure 3**) were mutated to cysteines or to amber TAG codons using standard site-directed mutagenesis with *Pfu Turbo* (Agilent). The original stop codon of this construct was also mutated from the amber stop codon to encode an opal stop codon (UAA) to allow for successful translation termination.

LBD protein expression

Mutant plasmid was co-transformed into Origami B (DE3) cells (Novagen) along with the pEVOL plasmid containing the genes for the suppressor tRNA and

aminoacyl-tRNA synthetase needed to incorporate *p*-acetyl-L-phenylalanine (pEVOL plasmid was provided by Peter Schulz, Scripps Research Institute, CA) (136). 1-liter liquid cultures were grown in LB broth, Miller (Fisher) supplemented with 50 µg/ml ampicillin (Sigma), 15 µg/ml kanamycin (Fisher), 12.5 µg/ml tetracycline (CalBioChem), and 50 µg/ml chloramphenicol (Acros) until they reached an OD₆₀₀ of 0.8. Then, protein expression was induced by adding IPTG (Fisher) to a final concentration of 0.5 mM. If needed, the unnatural amino acid machinery was simultaneously induced by adding 0.02% arabinose (Sigma) and 1 mM AcF (RSP Amino Acids). Induction was carried out at 20°C for 20-24 hours. The cultures were then pelleted down, and the pellets were stored at -80°C until use.

LBD Protein purification

Pellets were thawed and lysed with a cell disruption vessel (Parr Instruments). Then, cell debris was pelleted by spinning at 185,000 × *g* for 1 hr at 4°C. For large scale purification with cysteine mutants, the GluN1 SIS2 in the supernatant was loaded onto an immobilized metal affinity chromatography column that had been previously charged with nickel sulfate (HiTrap HP, GE Healthcare) using fast protein liquid chromatography (AKTA, GE Healthcare). Purified GluN1 SIS2 was then eluted using a linear gradient of imidazole (Sigma). With smaller scale purification of the double unnatural amino acid constructs, the supernatant was collected and purified by binding with 1 ml of Ni-NTA agarose resin (Qiagen). Protein was then eluted with 200 mM imidazole (Sigma), concentrated down, and then brought to 500 µl in PBS, pH 7, supplemented with 1 mM glycine (Fisher). Western blots of the purified mutant

protein confirm expression of the full 35 kDa His-tagged LBD only upon induction of the unnatural amino acid machinery, showing successful incorporation and utilization of the unnatural amino acid (**Figure 23a**).

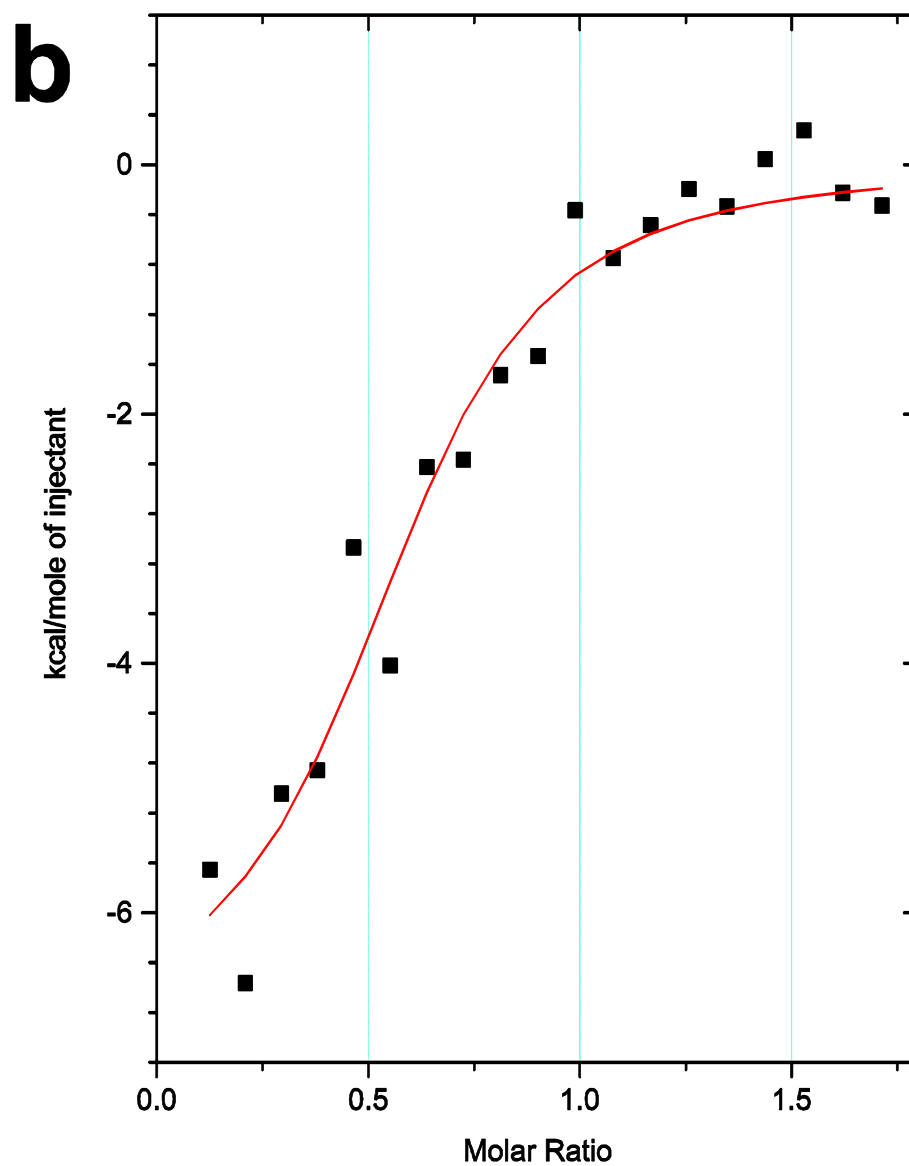
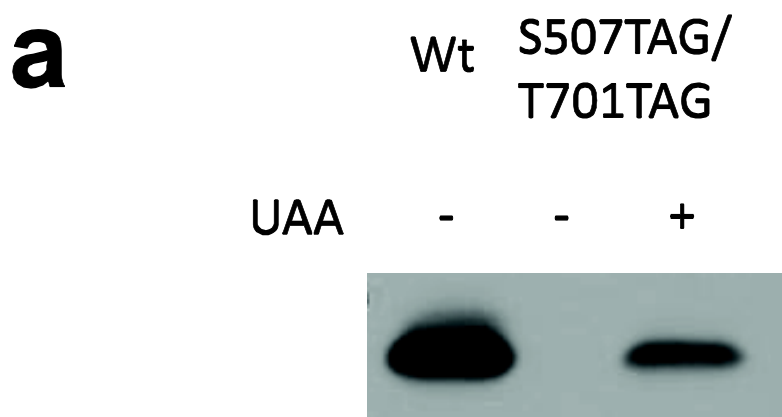


Figure 23. Characterization of the GluN1 agonist-binding domain after incorporation of *p*-acetyl-L-phenylalanine

A, Western blots showing lysates from IL cultures probed with an antibody against domain 2 of the GluN1 agonist-binding domain of wild-type protein and S507 and T701 double-mutant protein with or without induction of unnatural amino acid machinery (UAA). Wild-type protein was diluted ten times to prevent oversaturation of the blot. *B*, Isothermal titration calorimetry data from the GluN1 agonist-binding domain having incorporated *p*-acetyl-L-phenylalanine. The K_d for binding MDL 105,519 is $7 \pm 3 \times 10^{-8}$ M, similar to the K_d determined previously with wild-type agonist-binding domain (4).

Labeling of LBD for FRET

Fluorescent dyes were added to the above protein sample. Alexa 555 and Alexa 647 (Invitrogen) were used as the donor and acceptor, respectively, for attached-FRET experiments, whereas Alexa 488 was used as the donor for diffusing-FRET. For cysteine labeling the maleimide derivatives were used. To label the unnatural amino acids, we used ketone-reactive, hydrazide-conjugated fluorescent dyes (**Figure 4**). Donor and acceptor dyes were pre-mixed, then added such that dye:protein molar ratios were 1:1 for donor and 4:1 for acceptor, in order to minimize proteins labeled with only donor fluorophores. Unnatural amino acid protein was labeled overnight at 4°C. The following day, excess dye was removed from the protein by dialysis in 2L of PBS for 6 hours, changing the dialysis buffer every 2 hours. Glycine was added to the dialysis buffer up to 1 mM for the glycine samples. With cysteine mutations, labeling was performed for only 30 minutes before removing excess label by purifying the protein onto a nickel affinity column (nickel-nitrilotriacetic acid-agarose, Qiagen). Imidazole was used for elution and it was removed using a PD-10 desalting column equilibrated with PBS buffer (GE Healthcare). For samples liganded to D-serine (Acros Organics), L-alanine (Acros Organics), ACBC (Aldrich), or DCKA (abcam), the appropriate ligand was added to the sample before and after each exchange if dialysis was performed (1 mM, 15 mM, 10 mM and 1 mM, respectively, based on differential affinities for each ligand). This type of ligand substitution was also performed for glycine. No significant changes were noted and the glycine data was pooled for final analysis. For attached smFRET experiments, 1 µg of biotin-conjugated anti-His epitope antibody (Rockland) was added to a 500 µl sample.

Isothermal calorimetry

The functionality of the GluN1 LBD protein with unnatural amino acids tagged with fluorophores was determined using isothermal calorimetry (**Figure 23b**). For these experiments the protein was extensively dialyzed to the apo state in buffer containing 20 mM HEPES (pH 7), 150 mM NaCl, 1 mM EDTA, and 10% glycerol. Calorimetric titrations were performed with VP-ITC (MicroCal) using 1 μ M protein with twenty 10 μ L injections of 15 μ M (*E*)-4,6-dichloro-3-(2-phenyl-2-carboxyethenyl)indole-2-carboxylic acid (MDL 105,519) (Sigma) at 23°C. Data analysis was performed using Origin (OriginLab).

Attached-smFRET LBD sample preparation (132)

For all single molecule measurements in this study, plasma-cleaned 22x22 mm micro glass coverslips (VWR) were immersed in a VECTABOND-acetone solution (1% w/v, Vector Laboratories, Burlingame, CA) for 5 minutes, rinsed with molecular-biology grade water, dried with nitrogen, and stored under vacuum to prevent contamination. A silicon template was placed on the VECTABOND-functionalized slide to allow filling of the future chamber area with PEG solution (5 kDa biotin-terminated PEG (2.5% w/w in MB water, NOF Corporation) and sodium bicarbonate (Sigma)) and the filled slide was allowed to dry in the dark for 4-6 hours. Excess PEG was washed off with 10-12 ml MB water and, after nitrogen-drying the slide, a custom HybriWell chamber (Grace Bio-Labs) fitted with an inlet and outlet port (press-fit tubing connectors, Grace Bio-Labs) was arranged precisely over the PEGylated area.

After filling the chamber with PBS buffer, a control image was taken to ensure a clean sample, followed by insertion of 0.2 mg/ml streptavidin (Invitrogen) in PBS buffer. Biotin-streptavidin binding was allowed to progress for 10 minutes. The protein of interest, with the biotin-conjugated anti-His-antibody for streptavidin association, was added to the chamber at an approximate concentration of 20 nM and incubated for 20 min. Unbound protein was washed out by flushing the chamber with an excess of PBS buffer.

Measurements of attached-FRET LBD data

The sample chamber was secured to a closed-loop x-y-z piezo stage (P-517.3CL; Physik Instrumente) with 100 x 100 x 20 μm travel range and 1 nm specificity (SPM 1000, RHK Technology) to allow for precise movement of the sample area. In order to extend the lifetimes of the fluorophores, an oxygen scavenging buffer solution of 33% w/w β -D-(+)-glucose (Sigma), 1% w/w glucose oxidase, 0.1% v/v catalase (Sigma), 1 mM methyl viologen (Sigma), and 1 mM ascorbic acid (Sigma) in PBS was continuously pumped through the chamber using a syringe-pump flow system at a rate of 1 $\mu\text{l}/\text{min}$ (169). Additionally, the above concentrations of the specific LBD ligand, depending on the experimental conditions, was included in the buffer solution. The custom-built confocal microscope (Zeiss Axiovert 200 M) described previously was used for all smFRET measurements (137, 170). A 532 nm diode-pumped solid-state laser (Coherent, Compass 315M-100 SL) focused through a FLUAR 100x 1.3 NA oil immersion microscope objective lens (Carl Zeiss, GmbH) to a power density of 50 W/cm^2 at the sample was used to excite the sample. Emitted light was collected back

through the same objective and was passed through a notch filter (zet532nf, Chroma Technology) and towards the detector box. The fluorescence emission light was separated by a 640 nm high-pass dichroic mirror (Chroma 640 DCXR) and collected by two corresponding avalanche photodiode detectors (SPCM AQR-15, Perkin Elmer) set to 570 nm and 670 nm using band-pass filters (NHPF-532.0, Kaiser Optical and ET585, Chroma Technology) for donor and acceptor signal collection. An area of 10x10 μm was raster scanned to locate individual molecules. After a single molecule was chosen for observation, the stage was moved to focus the laser on the particular molecule and then the donor and acceptor fluorescence signals were collected until photobleaching of the fluorophores occurred.

Data analysis of attached-FRET LBD

A 1 ms time resolution was used to record the emission intensity trajectories and then binned up to 10 ms frames during data processing to improve the signal-to-noise ratio. The data analysis was performed by an in house script using Matlab (R2009b, Mathworks) which processed the signals via the wavelet denoising technique (154, 155). The denoised signal was then used to calculate the FRET efficiency at each time point, using Equation 6 (Chapter 3). (132, 133). From this FRET efficiency, the distance was determined through Equation 1, the Förster equation. The Förster radius is 51 Å for the Alexa 555-Alexa 647 fluorophore pair used for these experiments. Error in FRET efficiencies was set at 0.03 based on measurements under the same conditions performed with a rigid DNA double strand. The standard error of the mean for the fraction of proteins with FRET efficiencies higher than 0.96 was

calculated using the above error in FRET efficiency and determining the fractions at the two extremes in error and by dividing by the square root of the number of molecules studied for each ligand-bound state.

After processing the data, the traces were further filtered for single molecule verification and excluded if they showed criteria of multistep bleaching or exceptionally high background adapted from a normal distribution.

Electrophysiology for testing the LBD mutants

HEK-293T cells were transfected using jetPRIME® Polyplus with GluN1 S507C/T701C, wild-type GluN2A, and enhanced GFP at a microgram ratio of 1:3:1, respectively, with 5 µg of total DNA/10 ml of medium. After a 10–12-h incubation with transfection reagents, cells were plated at low density onto tissue culture dishes. 300 µM DL-APV and 30 µM DCKA were present in the medium during and after transfection. Whole cell patch clamp recordings were performed 24–48 h after transfection using borosilicate glass pipettes with 3–5 megohm resistance, coated with dental wax, fire-polished, and filled with the following solution: 135 mM CsF, 33 mM CsOH, 2 mM MgCl₂, 1 mM CaCl₂, 11 mM EGTA, and 10 mM HEPES, pH 7.4. The external solution was: 140 mM NaCl, 2.8 mM KCl, 1 mM CaCl₂, 10 mM HEPES, pH 7.4. Solutions were locally applied to isolated cells using a stepper motor system (SF-77B; Warner Instruments) with triple barrel tubing. External solution alone was applied as a control, and the cells were then pulsed with glutamate (1 mM) and with a GluN1 ligand for 5 s with a 3-s interval between pulses. The GluN1 ligands tested were glycine, 1 mM; D-serine, 1 mM; L-alanine, 15 mM; ACBC, 10 mM; and DCKA, 100 µM to match the MFD

experiments. Cells were held at –60 mV. All recordings were performed using an Axopatch 200B amplifier (Molecular Devices), acquired at 10 kHz using pCLAMP10 software (Molecular Devices) and filtered online at 5 kHz. All experiments were performed at room temperature.

Accessible Volume (AV) simulations to estimate measured distance

The accessible volume considers the dyes as hard sphere models connected to the protein via flexible linkers (modeled as a flexible cylindrical pipe) (121, 143, 171, 172). The overall dimension (width and length) of the linker is based on their chemical structures. For Alexa 488 the five-carbon linker length was set to 20 Å, the width of the linker is 4.5 Å, and three dye radii 5.0, 4.0, and 1.5 Å. Similarly, for Alexa 647 the dimensions used were: length = 22 Å, width = 4.5 Å and the three dye radii 11.0, 3.0, and 1.5 Å.

To account for dye linker mobility we generated AVs for donor and acceptor dyes attached to the LBD by *in silico* labeling at Ser-507 and Thr-701. For this pair of AVs, we calculated the distance between dye mean positions (R_{mp}),

$$R_{mp} = |\langle \vec{R}_{D(i)} \rangle - \langle \vec{R}_{A(j)} \rangle| = \left| \frac{1}{n} \sum_{i=1}^n \vec{R}_D^{(i)} - \frac{1}{m} \sum_{j=1}^m \vec{R}_A^{(j)} \right| \quad (11)$$

where $\vec{R}_D^{(i)}$ and $\vec{R}_A^{(j)}$ are all the possible positions that the donor and acceptor fluorophores can take. However, in intensity based measurements, the mean donor-acceptor distance is determined by the integration time and R_{mp} cannot be experimentally determined; thus, the effective and experimentally determined distance becomes,

$$\langle R_{DA} \rangle_E = R_0 (\langle E \rangle^{-1} - 1)^{1/6} \quad \text{with}$$

$$\langle E \rangle = \frac{1}{nm} \sum_{i=1}^n \sum_{j=1}^m \left(\frac{R_0}{R_0 + \left| \vec{R}_D^{(i)} - \vec{R}_A^{(j)} \right|^6} \right) \quad (12)$$

the relationship between R_{mp} and $\langle R_{DA} \rangle_E$ can be derived empirically following a third order polynomial from many different simulations.

MFD for smFRET experiments

MFD for confocal smFRET studies of single molecules was done using PIE (173) with two diode lasers (model LDH-D-C-485 at 485 nm and laser LDH-D-C-640 at 640 nm; PicoQuant, Germany) operating at 40 MHz with 25-ns interleaved time. The power at objective was set for 120 microwatts for the 485-nm laser line and 39 microwatts for the 640 nm excitation. Freely diffusing doubly labeled LBD molecules are excited as they pass through the focal point of a $\times 60$, 1.2 NA collar (0.17) corrected Olympus objective. The emitted fluorescence signal was collected through the same objective and spatially filtered using a 70- μm pinhole to define an effective confocal detection volume. The emitted fluorescence was divided into parallel and perpendicular polarization components at two different spectral windows (“green” and “red”) through band pass filters, ET525/50 and ET720/150, for green and red, respectively (Chroma Technology Co.). In total, four photon detectors are used: two for green (PMA hybrid model 40 PicoQuant) and two for red channels (PMA hybrid model 50, PicoQuant). A TCSPC module (HydraHarp 400, PicoQuant) with time-tagged time-resolved mode and 4 synchronized input channels were used for data registration.

For smFRET measurements donor-acceptor (DA)-labeled LBD samples were diluted to a picomolar concentration in PBS buffer (50 mM sodium phosphate, pH 7.5, 150 mM NaCl), which had been charcoal filtered to remove residual impurities. At picomolar concentrations we assure that we observe ~ 1 molecule/s. To prevent adsorption artifacts, NUNC chambers (Lab-Tek, Thermo Scientific, Germany) were pre-coated with a solution of 0.01% Tween 20 (Thermo Scientific) in water for 30 min and then rinsed with ddH₂O. Collection time varied from several minutes up to 2 h. Standard controls consisted of measuring water to determine the instrument response function, buffer for background subtraction and the nanomolar concentration of green and red standard dyes (Rhodamine 110, Rhodamine 101, and Alexa 647) in water solutions for calibration of green and red channels, respectively. To calibrate the detection efficiencies we used a mixture solution of double labeled DNA oligonucleotides with known distance separation between donor and acceptor dyes. Ligands used were glycine, 1 mM; D-serine, 1 mM; L-alanine, 15 mM; ACBC, 10 mM; or DCKA 100 μ M.

MFD histograms and FRET lines

Bursts were selected by 2σ criteria out of the mean background value with cut-off times that vary from sample to sample with a minimum of 60 photons for each burst (174). Each burst was then processed and fitted using a maximum likelihood algorithm and previously developed programs (LabVIEW, National Instruments Co.) (175). Bursts were selected according to the following rules: the difference in burst duration on green channels given donor excitation (T_{GX}) and burst duration on red

channels given direct acceptor excitation (T_{RR}) was $-1.5 \text{ ms} < T_{GX} - T_{RR} < 1.5 \text{ ms}$; and bursts satisfy the FRET stoichiometry (S_{PIE}) parameter of $0.13 < S_{PIE} < 0.6$, which selects for bursts with both fluorophores present. Fluorescent bursts were plotted in two-dimensional histograms (Origin 8.6, OriginLab Co.).

The relationship between the ratio of the donor fluorescence over the acceptor fluorescence F_D/F_A and the fluorescence-weighted lifetime obtained in burst analysis $\langle \tau_{D(A)} \rangle_f$ depends on specific experimental parameters such as fluorescence quantum yields of the dyes ($\Phi_{FD(0)}$ and Φ_{FA} for donor and acceptor, respectively), background ($\langle B_G \rangle$ and $\langle B_R \rangle$ for green and red channels, respectively), detection efficiencies (g_G and g_R for green and red, respectively), and cross-talk (α). The parametric line that relates two FRET indicators (F_D/F_A and $\langle \tau_{D(A)} \rangle_f$) was introduced by Seidel's group and is defined as,

$$\left(\frac{F_D}{F_A} \right)_{static} = \frac{\Phi_{FD(0)}}{\Phi_{FA}} \cdot \left(\frac{\tau_{D(0)}}{\sum_{i=0}^3 A_i (\langle \tau_{D(A)} \rangle_{f,L})^i} - 1 \right)^{-1} \quad (13)$$

Where A_i are the coefficients of an empirical polynomial function that takes into account the intrinsic linker dynamics of the dyes. FRET lines are used to identify static or slowly exchanged limiting populations.

Quantum yields

The donor and acceptor quantum yields were corrected due to the presence of different ligands and need to be corrected accordingly. We assumed that only dynamic quenching takes place and that $\Phi_{FD(0)}$, Φ_{FA} are proportional to the species-averaged fluorescence lifetime $\langle \tau_{D(A)} \rangle_x$ of donor or acceptor, respectively. As reference samples we used Alexa 488-labeled DNA $\langle \tau_{D(0)} \rangle_x = 4.0 \text{ ns}$, $\Phi_{FD(0)} = 0.8$ and for the

acceptor we used Cy5-labeled DNA with $\langle\tau_A\rangle_x = 1.17$ ns and $\Phi_{FA} = 0.32$ (176). The obtained donor and acceptor quantum yields are presented in **Table 10**. This FRET pair has a reduced Förster distance of 52 Å where we assumed isotropic reorientation of the dyes using $\kappa^2 = 2/3$ due to the long linkers.

Table 10. Quantum Yields were estimated as described in Appendix

Sample	$\Phi_{FD(0)}$	Φ_{FA}
Gly	0.773	0.42
D-Ser	0.828	0.43
L-Ala	0.843	0.41
ACBC	0.799	0.38
DCKA	0.850	0.40

$\kappa^2 = 2/3$ Assumption, $\langle\kappa^2\rangle$, and κ^2 Distributions

Experimentally, one can test whether assuming $\kappa^2 = 2/3$ is justifiable or not. Considering that fluorophores follow the “wobble in a cone” model (177), it is possible to calculate a distribution of all possible values of κ^2 . For that, we determined the residual anisotropies (r_∞) (D only, donor; A, acceptor, and A(D), the sensitized by

FRET emission of acceptor) from single molecule experiments. We consider the extreme limit when $\langle r_{ss} \rangle \cong r_{\infty}$. Then, all κ^2 values will follow (143),

$$\begin{aligned} \kappa^2 = & \frac{2}{3} + \frac{2}{3} S_D^{(2)} S^{(2)}(\beta_1) + \frac{2}{3} S_A^{(2)} S^{(2)}(\beta_2) \\ & + \frac{2}{3} S_D^{(2)} S_A^{(2)} \left(\frac{S^{(2)}(\delta) + 6S^{(2)}(\beta_1)S^{(2)}(\beta_2)}{+1 + 2S^{(2)}(\beta_1) + 2S^{(2)}(\beta_2)} \right. \\ & \left. - 9 \cos \beta_1 \cos \beta_2 \cos \delta \right) \end{aligned} \quad (14)$$

where, β_1 and β_2 are the angles between the symmetry axes of the dyes rotations, and δ is the angle between the symmetry. The necessary second-rank order parameters $S^{(2)}$ are defined by,

$$\begin{aligned} S^{(2)}(\delta) &= \frac{1}{2} (3 \cos^2 \delta - 1) = \frac{r_{ss,A(D)}}{r_0 S_D^{(2)} S_A^{(2)}} \\ S^{(2)}(\beta_1) &= \frac{1}{2} (3 \cos^2 \beta_1 - 1) \\ S^{(2)}(\beta_2) &= \frac{1}{2} (3 \cos^2 \beta_2 - 1) \end{aligned} \quad (15)$$

where r_0 is the fundamental anisotropy of the dyes whose values were 0.38 and 0.39 for the donor and acceptor fluorophores, respectively. The dye motions are characterized by the second-rank order parameters $S_D^{(2)}$ and $S_A^{(2)}$ by Equation 16

$$\begin{aligned} \text{Donor} \quad & \frac{1}{2} \cos^2 \theta_{disk} = \sqrt{\frac{r_{ss,D-only}}{r_0}} = -S_D^{(2)} \\ \text{Acceptor} \quad & \frac{1}{2} \cos \theta_{cone} (1 + \cos \theta_{cone}) = \sqrt{\frac{r_{ss,A}}{r_0}} = S_A^{(2)} \end{aligned} \quad (16)$$

From all possible orientations and combinations a κ^2 - distribution and its corresponding arithmetic mean ($\langle \kappa^2 \rangle$) can be determined and compared with the assumed to $\kappa^2 = 2/3$.

Probability distribution analysis (PDA)

To model the shape of the F_D/F_A distributions we use probability distribution analysis or PDA (140, 178). In short, the measured fluorescence signal (S), consisting of fluorescence (F), and background (B) photons are expressed in photon count numbers per time window (Δt) of a fixed length. In multiparameter fluorescence detection the signal is split into two spectral windows termed “green” and “red” each with two polarization components (parallel “ \parallel ” and perpendicular “ \perp ”). The probability of observing a certain combination of photon counts in two detection channels 1 and 2 (*e.g.* 1 = green and 2 = red) and measured by two or more single-photon counting detectors, $P(S_1, S_2)$, is given by a product of independent probabilities,

$$P(S_1, S_2) = \sum_{F_1+B_1=S_1; F_2+B_2=S_2} P(F) P(F_1, F_2|F) P(B_1) P(B_2) \quad (17)$$

$P(F)$ describes the fluorescence intensity distribution, *i.e.* the probability of observing exactly F fluorescence photons per time window (Δt). $P(B_1)$ and $P(B_2)$ represent the background intensity distributions. $P(F_1, F_2|F)$ is the conditional probability of observing a particular combination of F_1 and F_2 , provided the total number of fluorescence photons is F . This can be expressed as,

$$P(F_1, F_2|F) = \frac{F!}{F_1! F_2!} p_1^{F_1} p_2^{F_2} = \frac{F!}{F_1! (F - F_1)!} p_1^{F_1} (1 - p_1)^{F - F_1} \quad (18)$$

where p_1 stands for the probability of a detected photon to be registered by the first detector (*e.g.* green in a FRET experiment). For smFRET, p_1 is unambiguously related to the FRET efficiency E according to,

$$p_1 = \left(1 + \alpha + \frac{E\Phi_{FA}}{(1-E)G\Phi_{FD(0)}} \right)^{-1} \quad (19)$$

$$p_2 = 1 - p_1$$

here, G stands for the ratio of the detection efficiencies in the spectral windows ($G = g_G/g_R$). The quantum yields ($\Phi_{FD(0)}$ and Φ_{FA}) were previously defined, and α is the spectral cross-talk.

The distribution $P(F)$ in Equation 17 is not directly measurable; instead, the total signal intensity distribution $P(S)$ is measured, which is given by,

$$P(S) = P(F) \otimes P(B) \quad (20)$$

where $P(B)$ is the distribution probability of background counts. Details on the deconvolution procedure are described elsewhere (140). Finally, Equation 19 can be extended for multiple species with the brightness correction used in this work (179). Each species distribution has a half-width (hw_{DA}), which depends mostly in shot noise and photophysical properties of the acceptor fluorophore, and it was fixed to 6% of the $\langle R_{DA} \rangle_E$.

Generation of smFRET constructs for TMD measurements

Wild-type GluN1-1a and GluN2A plasmids in pcDNA3.1 were kindly provided by Shigetada Nakanishi (Osaka Bioscience Institute, Osaka, Japan). All mutations were introduced using standard PCR-based mutagenesis methods. To create the background constructs, non-disulfide-bonded cysteines at sites 15 and 22 in GluN1 and 231, 399, and 460 in GluN2A were mutated to serines, resulting in GluN1* and GluN2A*. In order to label these receptors, a reactive cysteine was mutated to replace the native phenylalanine at site 554 in GluN1*.

Electrophysiology for TMD measurements

HEK293T cells were plated into 30 mm dishes and transfected (jetPrime, PolyPlus) with GluN1*F554C and GluN2A* constructs at a mass ratio of 1.5:4.5 μg per 20 ml of media. 300 μM DL-AP5 (abcam) and 30 μM DCKA (abcam) were present in the media and recordings were performed 24 to 48 hours post-transfection. Prior to recording, cells were incubated in 150 nM Alexa 555 maleimide (ThermoFisher) and 600 nM Alexa 647 maleimide (ThermoFisher) for at least 1 hour to mimic smFRET labelling conditions. Outside-out patches were excised and piezo-driven solution exchange was performed as outlined elsewhere (180). The external solution was (in mM) 150 NaCl, 20 HEPES, 10 Tricine, 1 CaCl_2 , and 0.1 glycine, pH 7.4 (NaOH). The pipette solution was 135 CsF, 33 CsOH, 11 EGTA, 10 HEPES, 2 MgCl_2 and 1 CaCl_2 , pH 7.4. Lifted whole cell recordings were performed as described elsewhere (122) using the same solutions as above with the addition of 2.5 mM KCl to the external solution.

Single molecule FRET sample preparation for TMD measurements

HEK293T cells were transiently transfected with GluN1*F554C and GluN2A* DNA at a mass ratio of 2.5:7.5 μg per 10 cm dish. 300 μM DL-AP5 (abcam) and 30 μM DCKA (abcam) were present during transfection to limit excitotoxicity. One day post-transfection, cells from two 10-cm dishes were harvested and labeled for 1 hour at room temperature with 150 nM of donor fluorophore Alexa 555 maleimide (ThermoFisher) and 600 nM of acceptor fluorophore Alexa 647 maleimide (ThermoFisher) in 3 mL extracellular buffer. After washing, labeled cells were then

solubilized for 1 hour at 4°C in buffer containing phosphate-buffered saline, 1% lauryl maltose neopentyl glycol (Anatrace), 2 mM cholesteryl hydrogen succinate (MP Biomedicals), and protease inhibitor (Pierce). Unsolubilized debris were then spun down for 1 hour at $100,000 \times g$ at 4°C, and the supernatant used as the smFRET sample.

Flow chamber preparation for TMD measurements

Plasma cleaned glass coverslips (22 × 22 mm No. 1) were aminosilanized through Vectabond treatment (Vectabond in acetone 2% v/v; Vector Laboratories, Burlingame, CA). Silicone templates (Grace bio-Labs) were used to treat a small section of the coverslips with a PEG solution containing 5kDa biotin-terminated PEG (2.5% w/w in molecular biology grade (MB) water, NOF Corp.), and 5kDa mPEG succinimidyl carbonate (25% w/w in MB water, Laysan Bio Inc.) in 0.1M sodium bicarbonate (Sigma-Aldrich). The coverslips were then left to incubate in a dark and moist environment overnight. On the day of the experiment, the coverslips were treated with another round of PEGylation with a short chain 333 Da NHS-ester PEG (Thermo Scientific) and incubated for 2-3 hrs. After washing off excess PEG, the coverslips were dried with a mild flow of nitrogen. Custom hybriwell chambers (Grace bio-Labs) with dual silicon press-fit tubing connectors (Grace bio-Labs) were placed atop the coverslips to construct a flow chamber.

Protein preparation and attachment to coverslips for TMD measurements

Streptavidin in buffer solution containing Phosphate Buffered Saline (PBS), 1mM DDM (*n*-dodecyl- β -D-maltoside) and 0.2 mM CHS (cholesteryl hemisuccinate), were introduced through the flow chamber and incubated for 10 minutes. 10 nM of biotinylated goat Anti-Mouse IgG (H+L) secondary antibody (Jackson Immuno Research Laboratories, Inc.) was then flowed into the chamber and incubated for 20-30 minutes. Next, 10 nM of anti-NMDAR mouse monoclonal primary antibody (Abcam Inc.) was flowed in. After each antibody addition, the chamber was flushed with buffer to get rid of the unbound antibodies. All dilutions were made in PBS buffer with 1 mg/mL Bovine serum albumin (Sigma-Aldrich).

Meanwhile, whole cells expressing NMDA receptors were labeled with donor and acceptor fluorophores for 1 hour at room temperature. The cells were then lysed and the membrane proteins solubilized with 1% MNG-3. Intact NMDA receptors were then attached to a glass slide for FRET data acquisition using in situ immunoprecipitation (SiMPull (152)) by passing the solubilized protein through the chamber in three 60 μ L shots and incubating for 20-30 minutes before flushing the chamber with buffer containing Phosphate Buffered Saline (PBS), 1mM DDM (*n*-dodecyl- β -D-maltoside) and 0.2 mM CHS (cholesteryl hemisuccinate). Control slides using unmutated GluN1*/GluN2A* receptors showed minimal background labeling, while slides prepared with GluN1*F554C/GluN2A* showed isolatable single molecules exhibiting fluorescence and energy transfer (**Figure 16**).

smFRET data acquisition for TMD measurements

Acquisition was performed as above; however, ligands—1 mM glutamate, 1 mM glycine, 1 μ M MK-801, and/or 10 μ M Zn²⁺—were added to the ROXS to achieve the liganded conditions necessary for each TMD experiment. Additionally, 10 mM tricine was included to chelate any unbound zinc ions under the apo, desensitized, and open-stabilized conditions. Step Transition and State Identification (STaSI) analysis (89, 153) was run for each sample to obtain an unbiased determination of number and the identification of discrete conformational states within each sample (89, 90, 132, 133, 137, 152, 153).

Free energy calculations

For each liganded condition, the free energy of the most populated STaSI-identified state was set to 0 $k_B T$. The STaSI determined occupancies were then used to calculate the equilibrium constant K_{eq} between each pair of states, and the free energy of every state relative to the most populated state was determined via the equation:

$$\Delta G^0 = -k_b T \ln K_{eq} \quad (21)$$

The transition probabilities between each pair of states, given our 10 ms bin time, was used to determine the reaction rate for each transition, and the heights of the energy of activation barriers were calculated assuming a first-order reaction rate and the Arrhenius equation:

$$\begin{aligned} rate &= k[\text{starting state}] \\ k &= A e^{-E_a/k_B T} \end{aligned} \quad (22)$$

Concentration of the starting state was taken as the STaSI-derived fractional occupancy of that state, and the value of the pre-exponential was chosen to be $(10 \text{ ms})^{-1}$. Forward and reverse energies of activation were averaged in the final figure.

Bibliography

1. Traynelis, S. F., L. P. Wollmuth, C. J. McBain, F. S. Menniti, K. M. Vance, K. K. Ogden, K. B. Hansen, H. Yuan, S. J. Myers, and R. Dingledine. 2010. Glutamate Receptor Ion Channels: Structure, Regulation, and Function. *Pharmacological Reviews* 62: 405-496.
2. Paoletti, P., C. Bellone, and Q. Zhou. 2013. NMDA receptor subunit diversity: Impact on receptor properties, synaptic plasticity and disease. *Nature Reviews Neuroscience* 14: 383-400.
3. Johnson, K. A., P. J. Conn, and C. M. Niswender. 2009. Glutamate receptors as therapeutic targets for Parkinson's disease. *CNS & neurological disorders drug targets* 8: 475-491.
4. Furukawa, H., and E. Gouaux. 2003. Mechanisms of activation, inhibition and specificity: crystal structures of the NMDA receptor NR1 ligand-binding core. *The EMBO journal* 22: 2873-2885.
5. Furukawa, H., S. K. Singh, R. Mancusso, and E. Gouaux. 2005. Subunit arrangement and function in NMDA receptors. *Nature* 438: 185-192.
6. Inanobe, A., H. Furukawa, and E. Gouaux. 2005. Mechanism of partial agonist action at the NR1 subunit of NMDA receptors. *Neuron* 47: 71-84.
7. Karakas, E., N. Simorowski, and H. Furukawa. 2009. Structure of the zinc-bound amino-terminal domain of the NMDA receptor NR2B subunit. *The EMBO journal* 28: 3910-3920.

8. Karakas, E., N. Simorowski, and H. Furukawa. 2011. Subunit arrangement and phenylethanolamine binding in GluN1/GluN2B NMDA receptors. *Nature* 475: 249-253.
9. Lee, C.-H., W. Lu, J. C. Michel, A. Goehring, J. Du, X. Song, and E. Gouaux. 2014. NMDA receptor structures reveal subunit arrangement and pore architecture. *Nature* 511: 191-197.
10. Karakas, E., and H. Furukawa. 2014. Crystal structure of a heterotetrameric NMDA receptor ion channel. *Science (New York, N.Y.)* 344: 992-997.
11. Tajima, N., E. Karakas, T. Grant, N. Simorowski, R. Diaz-Avalos, N. Grigorieff, and H. Furukawa. 2016. Activation of NMDA receptors and the mechanism of inhibition by ifenprodil. *Nature* 534: 63-68.
12. Zhu, S., Richard A. Stein, C. Yoshioka, C.-H. Lee, A. Goehring, Hassane S. McHaourab, and E. Gouaux. 2016. Mechanism of NMDA Receptor Inhibition and Activation. *Cell* 165: 704-714.
13. Bean, B. P. 2007. The action potential in mammalian central neurons. *Nature reviews. Neuroscience* 8: 451-465.
14. Mayer, M. L., G. L. Westbrook, and P. B. Guthrie. 1984. Voltage-dependent block by Mg^{2+} of NMDA responses in spinal cord neurones. *Nature* 309: 261-263.
15. Nowak, L., P. Bregestovski, P. Ascher, A. Herbert, and A. Prochiantz. 1984. Magnesium gates glutamate-activated channels in mouse central neurones. *Nature* 307: 462-465.

16. Dingledine, R., K. Borges, D. Bowie, and S. F. Traynelis. 1999. The glutamate receptor ion channels. *Pharmacol Rev* 51: 7-61.
17. Monyer, H., R. Sprengel, R. Schoepfer, A. Herb, M. Higuchi, H. Lomeli, N. Burnashev, B. Sakmann, and P. H. Seeburg. 1992. Heteromeric NMDA receptors: molecular and functional distinction of subtypes. *Science (New York, N.Y.)* 256: 1217-1221.
18. Vicini, S., J. F. Wang, J. H. Li, W. J. Zhu, Y. H. Wang, J. H. Luo, B. B. Wolfe, and D. R. Grayson. 1998. Functional and Pharmacological Differences Between Recombinant N-Methyl-D-Aspartate Receptors. *Journal of Neurophysiology* 79: 555-566.
19. Wyllie, D. J., P. Behe, and D. Colquhoun. 1998. Single-channel activations and concentration jumps: comparison of recombinant NR1a/NR2A and NR1a/NR2D NMDA receptors. *The Journal of physiology* 510 (Pt 1): 1-18.
20. Johnson, J. W., and P. Ascher. 1987. Glycine potentiates the NMDA response in cultured mouse brain neurons. *Nature* 325: 529-531.
21. Wolosker, H., S. Blackshaw, and S. H. Snyder. 1999. Serine racemase: a glial enzyme synthesizing D-serine to regulate glutamate-N-methyl-D-aspartate neurotransmission. *Proceedings of the National Academy of Sciences of the United States of America* 96: 13409-13414.
22. Lüscher, C., and R. C. Malenka. 2012. NMDA Receptor-Dependent Long-Term Potentiation and Long-Term Depression (LTP/LTD). *Cold Spring Harbor Perspectives in Biology* 4.

23. Lisman, J., H. Schulman, and H. Cline. 2002. The molecular basis of CaMKII function in synaptic and behavioural memory. *Nature reviews. Neuroscience* 3: 175-190.
24. Bliss, T. V. P., and G. L. Collingridge. 1993. A synaptic model of memory: long-term potentiation in the hippocampus. *Nature* 361: 31-39.
25. Malenka, R. C., Nicoll, and R. A. 1999. Long-Term Potentiation--A Decade of Progress? *Science (New York, N.Y.)* 285: 1870-1874.
26. Salter, M. W., and L. V. Kalia. 2004. Src kinases: a hub for NMDA receptor regulation. *Nature reviews. Neuroscience* 5: 317-328.
27. Sweatt, J. D. 2004. Mitogen-activated protein kinases in synaptic plasticity and memory. *Current Opinion in Neurobiology* 14: 311-317.
28. Ehlers, M. D. 2000. Reinsertion or Degradation of AMPA Receptors Determined by Activity-Dependent Endocytic Sorting. *Neuron* 28: 511-525.
29. Benke, T. A., A. Luthi, J. T. R. Isaac, and G. L. Collingridge. 1998. Modulation of AMPA receptor unitary conductance by synaptic activity. *Nature* 393: 793-797.
30. Derkach, V., A. Barria, and T. R. Soderling. 1999. Ca²⁺/calmodulin-kinase II enhances channel conductance of α -amino-3-hydroxy-5-methyl-4-isoxazolepropionate type glutamate receptors. *Proceedings of the National Academy of Sciences* 96: 3269-3274.
31. Lisman, J. 1989. A mechanism for the Hebb and the anti-Hebb processes underlying learning and memory. *Proceedings of the National Academy of Sciences* 86: 9574-9578.

32. Carroll, R. C., E. C. Beattie, M. von Zastrow, and R. C. Malenka. 2001. Role of ampa receptor endocytosis in synaptic plasticity. *Nature reviews. Neuroscience* 2: 315-324.
33. Mulkey, R. M., S. Endo, S. Shenolikar, and R. C. Malenka. 1994. Involvement of a calcineurin/ inhibitor-1 phosphatase cascade in hippocampal long-term depression. *Nature* 369: 486-488.
34. Mulkey, R., C. Herron, and R. Malenka. 1993. An essential role for protein phosphatases in hippocampal long-term depression. *Science (New York, N.Y.)* 261: 1051-1055.
35. Markram, H., J. Lubke, M. Frotscher, and B. Sakmann. 1997. Regulation of synaptic efficacy by coincidence of postsynaptic APs and EPSPs. *Science (New York, N.Y.)* 275: 213-215.
36. Bi, G. Q., and M. M. Poo. 1998. Synaptic modifications in cultured hippocampal neurons: dependence on spike timing, synaptic strength, and postsynaptic cell type. *The Journal of neuroscience : the official journal of the Society for Neuroscience* 18: 10464-10472.
37. Celikel, T., V. A. Szostak, and D. E. Feldman. 2004. Modulation of spike timing by sensory deprivation during induction of cortical map plasticity. *Nature neuroscience* 7: 534-541.
38. Kampa, B. M., J. Clements, P. Jonas, and G. J. Stuart. 2004. Kinetics of Mg(2+) unblock of NMDA receptors: implications for spike-timing dependent synaptic plasticity. *The Journal of physiology* 556: 337-345.

39. Feldman, D. E. 2012. The spike timing dependence of plasticity. *Neuron* 75: 556-571.
40. Fedder, K., and S. Sabo. 2015. On the Role of Glutamate in Presynaptic Development: Possible Contributions of Presynaptic NMDA Receptors. *Biomolecules* 5: 3448.
41. Bouvier, G., C. Bidoret, M. Casado, and P. Paoletti. 2015. Presynaptic NMDA receptors: Roles and rules. *Neuroscience* 311: 322-340.
42. Garcia-Munoz, M., V. G. Lopez-Huerta, L. Carrillo-Reid, and G. W. Arbuthnott. 2015. Extrasynaptic glutamate NMDA receptors: Key players in striatal function. *Neuropharmacology* 89: 54-63.
43. Papouin, T., and S. H. R. Oliet. 2014. Organization, control and function of extrasynaptic NMDA receptors. *Philosophical Transactions of the Royal Society B: Biological Sciences* 369: 20130601.
44. Hardingham, G. E., and H. Bading. 2010. Synaptic versus extrasynaptic NMDA receptor signalling: implications for neurodegenerative disorders. *Nature reviews. Neuroscience* 11: 682-696.
45. Parsons, Matthew P., and Lynn A. Raymond. 2014. Extrasynaptic NMDA Receptor Involvement in Central Nervous System Disorders. *Neuron* 82: 279-293.
46. Hogan-Cann, A. D., and C. M. Anderson. Physiological Roles of Non-Neuronal NMDA Receptors. *Trends in pharmacological sciences* 37: 750-767.
47. Castillo, P. E. 2012. Presynaptic LTP and LTD of Excitatory and Inhibitory Synapses. *Cold Spring Harbor Perspectives in Biology* 4: a005728.

48. Fellin, T., O. Pascual, S. Gobbo, T. Pozzan, P. G. Haydon, and G. Carmignoto. 2004. Neuronal synchrony mediated by astrocytic glutamate through activation of extrasynaptic NMDA receptors. *Neuron* 43: 729-743.
49. Wang, Y., V. Briz, A. Chishti, X. Bi, and M. Baudry. 2013. Distinct Roles for μ -Calpain and m-Calpain in Synaptic NMDAR-Mediated Neuroprotection and Extrasynaptic NMDAR-Mediated Neurodegeneration. *The Journal of Neuroscience* 33: 18880-18892.
50. Stobart, J. L., L. Lu, H. D. Anderson, H. Mori, and C. M. Anderson. 2013. Astrocyte-induced cortical vasodilation is mediated by D-serine and endothelial nitric oxide synthase. *Proceedings of the National Academy of Sciences of the United States of America* 110: 3149-3154.
51. Faraci, F. M., and K. R. Breese. 1993. Nitric oxide mediates vasodilatation in response to activation of N-methyl-D-aspartate receptors in brain. *Circulation research* 72: 476-480.
52. Deng, A., J. M. Valdivielso, K. A. Munger, R. C. Blantz, and S. C. Thomson. 2002. Vasodilatory N-methyl-D-aspartate receptors are constitutively expressed in rat kidney. *Journal of the American Society of Nephrology : JASN* 13: 1381-1384.
53. Giardino, L., S. Armelloni, A. Corbelli, D. Mattinzoli, C. Zennaro, D. Guerrot, F. Tourrel, M. Ikehata, M. Li, S. Berra, M. Carraro, P. Messa, and M. P. Rastaldi. 2009. Podocyte glutamatergic signaling contributes to the function of the glomerular filtration barrier. *Journal of the American Society of Nephrology : JASN* 20: 1929-1940.

54. Lin, W., and S. C. Kinnamon. 1999. Physiological evidence for ionotropic and metabotropic glutamate receptors in rat taste cells. *J Neurophysiol* 82: 2061-2069.
55. Chaudhari, N., H. Yang, C. Lamp, E. Delay, C. Cartford, T. Than, and S. Roper. 1996. The Taste of Monosodium Glutamate: Membrane Receptors in Taste Buds. *The Journal of Neuroscience* 16: 3817-3826.
56. Yuan, H., Scott J. Myers, G. Wells, Katherine L. Nicholson, Sharon A. Swanger, P. Lyuboslavsky, Yesim A. Tahirovic, David S. Menaldino, T. Ganesh, L. J. Wilson, Dennis C. Liotta, James P. Snyder, and Stephen F. Traynelis. Context-Dependent GluN2B-Selective Inhibitors of NMDA Receptor Function Are Neuroprotective with Minimal Side Effects. *Neuron* 85: 1305-1318.
57. Moriyoshi, K., M. Masu, T. Ishii, R. Shigemoto, N. Mizuno, and S. Nakanishi. 1991. Molecular cloning and characterization of the rat NMDA receptor. *Nature* 354: 31-37.
58. Tichelaar, W., M. Safferling, K. Keinänen, H. Stark, and D. R. Madden. 2004. The Three-dimensional Structure of an Ionotropic Glutamate Receptor Reveals a Dimer-of-dimers Assembly. *Journal of molecular biology* 344: 435-442.
59. Kazi, R., J. Dai, C. Sweeney, H.-X. Zhou, and L. P. Wollmuth. 2014. Mechanical coupling maintains the fidelity of NMDA receptor-mediated currents. *Nature neuroscience* 17: 914-922.
60. Krupp, J. J., B. Vissel, S. F. Heinemann, and G. L. Westbrook. 1998. N-terminal domains in the NR2 subunit control desensitization of NMDA receptors. *Neuron* 20: 317-327.

61. Villarroel, A., M. P. Regalado, and J. Lerma. 1998. Glycine-independent NMDA receptor desensitization: localization of structural determinants. *Neuron* 20: 329-339.
62. Sobolevsky, A. I., C. Beck, and L. P. Wollmuth. 2002. Molecular rearrangements of the extracellular vestibule in NMDAR channels during gating. *Neuron* 33: 75-85.
63. Watanabe, J., C. Beck, T. Kuner, L. S. Premkumar, and L. P. Wollmuth. 2002. DRPEER: A Motif in the Extracellular Vestibule Conferring High Ca^{2+} Flux Rates in NMDA Receptor Channels. *The Journal of Neuroscience* 22: 10209-10216.
64. Yuan, H., K. B. Hansen, K. M. Vance, K. K. Ogden, and S. F. Traynelis. 2009. Control of NMDA Receptor Function by the NR2 Subunit Amino-Terminal Domain. *The Journal of Neuroscience* 29: 12045-12058.
65. Gielen, M., B. S. Retchless, L. Mony, J. W. Johnson, and P. Paoletti. 2009. Mechanism of differential control of NMDA receptor activity by NR2 subunits. *Nature* 459: 703-707.
66. Meddows, E., B. Le Bourdellès, S. Grimwood, K. Wafford, S. Sandhu, P. Whiting, and R. A. J. McIlhinney. 2001. Identification of Molecular Determinants That Are Important in the Assembly of N-Methyl-d-aspartate Receptors. *Journal of Biological Chemistry* 276: 18795-18803.
67. Takasu, M. A., M. B. Dalva, R. E. Zigmond, and M. E. Greenberg. 2002. Modulation of NMDA Receptor- Dependent Calcium Influx and Gene Expression Through EphB Receptors. *Science (New York, N.Y.)* 295: 491-495.

68. Dalva, M. B., M. A. Takasu, M. Z. Lin, S. M. Shamah, L. Hu, N. W. Gale, and M. E. Greenberg. 2000. EphB Receptors Interact with NMDA Receptors and Regulate Excitatory Synapse Formation. *Cell* 103: 945-956.
69. Masuko, T., K. Kashiwagi, T. Kuno, N. D. Nguyen, A. J. Pahk, J.-i. Fukuchi, K. Igarashi, and K. Williams. 1999. A Regulatory Domain (R₁-R₂) in the Amino Terminus of the *N*-Methyl-D-Aspartate Receptor: Effects of Spermine, Protons, and Ifenprodil, and Structural Similarity to Bacterial Leucine/Isoleucine/Valine Binding Protein. *Molecular Pharmacology* 55: 957-969.
70. Sobolevsky, A. I., M. P. Rosconi, and E. Gouaux. 2009. X-ray structure, symmetry and mechanism of an AMPA-subtype glutamate receptor. *Nature* 462: 745-756.
71. Sirrieh, R. E., D. M. MacLean, and V. Jayaraman. 2013. Amino-terminal domain tetramer organization and structural effects of zinc binding in the N-methyl-D-aspartate (NMDA) receptor. *The Journal of biological chemistry* 288: 22555-22564.
72. Sirrieh, R. E., D. M. MacLean, and V. Jayaraman. 2015. Subtype-dependent N-Methyl-d-aspartate Receptor Amino-terminal Domain Conformations and Modulation by Spermine. *The Journal of biological chemistry* 290: 12812-12820.
73. Sirrieh, R. E., D. M. MacLean, and V. Jayaraman. 2015. A conserved structural mechanism of NMDA receptor inhibition: A comparison of ifenprodil and zinc. *The Journal of General Physiology* 146: 173-181.

74. Kumar, J., and M. L. Mayer. 2013. Functional Insights from Glutamate Receptor Ion Channel Structures*. *Annual Review of Physiology* 75: 313-337.
75. Paoletti, P., A. M. Vergnano, B. Barbour, and M. Casado. 2009. Zinc at glutamatergic synapses. *Neuroscience* 158: 126-136.
76. Choi, Y.-B., and S. A. Lipton. 1999. Identification and Mechanism of Action of Two Histidine Residues Underlying High-Affinity Zn^{2+} Inhibition of the NMDA Receptor. *Neuron* 23: 171-180.
77. Low, C. M., F. Zheng, P. Lyuboslavsky, and S. F. Traynelis. 2000. Molecular determinants of coordinated proton and zinc inhibition of N-methyl-D-aspartate NR1/NR2A receptors. *Proceedings of the National Academy of Sciences of the United States of America* 97: 11062-11067.
78. Fayyazuddin, A., A. Villarroel, A. Le Goff, J. Lerma, and J. Neyton. 2000. Four residues of the extracellular N-terminal domain of the NR2A subunit control high-affinity Zn^{2+} binding to NMDA receptors. *Neuron* 25: 683-694.
79. Paoletti, P., F. Perin-Dureau, A. Fayyazuddin, A. Le Goff, I. Callebaut, and J. Neyton. 2000. Molecular Organization of a Zinc Binding N-Terminal Modulatory Domain in a NMDA Receptor Subunit. *Neuron* 28: 911-925.
80. Rachline, J., F. Perin-Dureau, A. Le Goff, J. Neyton, and P. Paoletti. 2005. The micromolar zinc-binding domain on the NMDA receptor subunit NR2B. *The Journal of neuroscience : the official journal of the Society for Neuroscience* 25: 308-317.
81. Perin-Dureau, F., J. Rachline, J. Neyton, and P. Paoletti. 2002. Mapping the binding site of the neuroprotectant ifenprodil on NMDA receptors. *The Journal*

- of neuroscience : the official journal of the Society for Neuroscience* 22: 5955-5965.
82. Williams, K. 1994. Mechanisms influencing stimulatory effects of spermine at recombinant N-methyl-D-aspartate receptors. *Mol Pharmacol* 46: 161-168.
 83. Traynelis, S. F., M. Hartley, and S. F. Heinemann. 1995. Control of proton sensitivity of the NMDA receptor by RNA splicing and polyamines. *Science (New York, N.Y.)* 268: 873-876.
 84. Mony, L., S. Zhu, S. Carvalho, and P. Paoletti. 2011. Molecular basis of positive allosteric modulation of GluN2B NMDA receptors by polyamines. *The EMBO journal* 30: 3134-3146.
 85. Schell, M. J., M. E. Molliver, and S. H. Snyder. 1995. D-serine, an endogenous synaptic modulator: localization to astrocytes and glutamate-stimulated release. *Proceedings of the National Academy of Sciences of the United States of America* 92: 3948-3952.
 86. Mothet, J.-P., A. T. Parent, H. Wolosker, R. O. Brady, D. J. Linden, C. D. Ferris, M. A. Rogawski, and S. H. Snyder. 2000. d-Serine is an endogenous ligand for the glycine site of the N-methyl-d-aspartate receptor. *Proceedings of the National Academy of Sciences* 97: 4926-4931.
 87. Papouin, T., L. Ladépêche, J. Ruel, S. Sacchi, M. Labasque, M. Hanini, L. Groc, L. Pollegioni, J.-P. Mothet, and Stéphane H. R. Oliet. 2012. Synaptic and Extrasynaptic NMDA Receptors Are Gated by Different Endogenous Coagonists. *Cell* 150: 633-646.

88. Le Bail, M., M. Martineau, S. Sacchi, N. Yatsenko, I. Radzishevsky, S. Conrod, K. Ait Ouares, H. Wolosker, L. Pollegioni, J.-M. Billard, and J.-P. Mothet. 2015. Identity of the NMDA receptor coagonist is synapse specific and developmentally regulated in the hippocampus. *Proceedings of the National Academy of Sciences* 112: E204-E213.
89. Cooper, D. R., D. M. Dolino, H. Jaurich, B. Shuang, S. Ramaswamy, C. E. Nurik, J. Chen, V. Jayaraman, and C. F. Landes. 2015. Conformational Transitions in the Glycine-Bound GluN1 NMDA Receptor LBD via Single-Molecule FRET. *Biophysical journal* 109: 66-75.
90. Dolino, D. M., D. Cooper, S. Ramaswamy, H. Jaurich, C. F. Landes, and V. Jayaraman. 2015. Structural Dynamics of the Glycine-binding Domain of the N-Methyl-d-Aspartate Receptor. *Journal of Biological Chemistry* 290: 797-804.
91. Dolino, D. M., S. Rezaei Adariani, S. A. Shaikh, V. Jayaraman, and H. Sanabria. 2016. Conformational Selection and Submillisecond Dynamics of the Ligand-binding Domain of the N-Methyl-d-aspartate Receptor. *The Journal of biological chemistry* 291: 16175-16185.
92. Rambhadran, A., J. Gonzalez, and V. Jayaraman. 2011. Conformational changes at the agonist binding domain of the N-methyl-D-aspartic acid receptor. *The Journal of biological chemistry* 286: 16953-16957.
93. Kussius, C. L., and G. K. Popescu. 2010. NMDA receptors with locked glutamate-binding clefts open with high efficacy. *The Journal of neuroscience : the official journal of the Society for Neuroscience* 30: 12474-12479.

94. Borschel, W. F., K. A. Cummings, L. K. Tindell, and G. K. Popescu. 2015. Kinetic Contributions to Gating by Interactions Unique to N-methyl-D-aspartate (NMDA) Receptors. *Journal of Biological Chemistry* 290: 26846-26855.
95. Hogner, A., J. S. Kastrup, R. Jin, T. Liljefors, M. L. Mayer, J. Egebjerg, I. K. Larsen, and E. Gouaux. 2002. Structural basis for AMPA receptor activation and ligand selectivity: crystal structures of five agonist complexes with the GluR2 ligand-binding core. *Journal of molecular biology* 322: 93-109.
96. Jin, R., M. Horning, M. L. Mayer, and E. Gouaux. 2002. Mechanism of activation and selectivity in a ligand-gated ion channel: structural and functional studies of GluR2 and quisqualate. *Biochemistry* 41: 15635-15643.
97. Jin, R., T. G. Banke, M. L. Mayer, S. F. Traynelis, and E. Gouaux. 2003. Structural basis for partial agonist action at ionotropic glutamate receptors. *Nature neuroscience* 6: 803-810.
98. Zhou, Y., J. H. Morais-Cabral, A. Kaufman, and R. MacKinnon. 2001. Chemistry of ion coordination and hydration revealed by a K⁺ channel-Fab complex at 2.0[thinsp][angst] resolution. *Nature* 414: 43-48.
99. Sommer, B., M. Kohler, R. Sprengel, and P. H. Seeburg. 1991. RNA editing in brain controls a determinant of ion flow in glutamate-gated channels. *Cell* 67: 11-19.
100. Bass, B. L. 2002. RNA editing by adenosine deaminases that act on RNA. *Annual review of biochemistry* 71: 817-846.
101. Burnashev, N., R. Schoepfer, H. Monyer, J. Ruppersberg, W. Gunther, P. Seeburg, and B. Sakmann. 1992. Control by asparagine residues of calcium

- permeability and magnesium blockade in the NMDA receptor. *Science (New York, N.Y.)* 257: 1415-1419.
102. Borschel, W. F., J. M. Myers, E. M. Kasperek, T. P. Smith, N. M. Graziane, L. M. Nowak, and G. K. Popescu. 2012. Gating reaction mechanism of neuronal NMDA receptors. *Journal of Neurophysiology* 108: 3105-3115.
 103. Vissel, B., J. J. Krupp, S. F. Heinemann, and G. L. Westbrook. 2001. A use-dependent tyrosine dephosphorylation of NMDA receptors is independent of ion flux. *Nature neuroscience* 4: 587-596.
 104. Scott, D. B., T. A. Blanpied, G. T. Swanson, C. Zhang, and M. D. Ehlers. 2001. An NMDA Receptor ER Retention Signal Regulated by Phosphorylation and Alternative Splicing. *The Journal of Neuroscience* 21: 3063-3072.
 105. Scott, D. B., T. A. Blanpied, and M. D. Ehlers. 2003. Coordinated PKA and PKC phosphorylation suppresses RXR-mediated ER retention and regulates the surface delivery of NMDA receptors. *Neuropharmacology* 45: 755-767.
 106. Hayashi, T., G. M. Thomas, and R. L. Huganir. 2009. Dual palmitoylation of NR2 subunits regulates NMDA receptor trafficking. *Neuron* 64: 213-226.
 107. Merrill, M. A., Z. Malik, Z. Akyol, J. A. Bartos, A. S. Leonard, A. Hudmon, M. A. Shea, and J. W. Hell. 2007. Displacement of alpha-actinin from the NMDA receptor NR1 Co domain By Ca²⁺/calmodulin promotes CaMKII binding. *Biochemistry* 46: 8485-8497.
 108. Ataman, Z. A., L. Gakhar, B. R. Sorensen, J. W. Hell, and M. A. Shea. 2007. The NMDA receptor NR1 C1 region bound to calmodulin: structural insights into

- functional differences between homologous domains. *Structure (London, England : 1993)* 15: 1603-1617.
109. Vissel, B., J. J. Krupp, S. F. Heinemann, and G. L. Westbrook. 2002. Intracellular Domains of NR2 Alter Calcium-Dependent Inactivation of *N*-Methyl-D-aspartate Receptors. *Molecular Pharmacology* 61: 595-605.
 110. Dore, K., J. Aow, and R. Malinow. 2016. The Emergence of NMDA Receptor Metabotropic Function: Insights from Imaging. *Frontiers in Synaptic Neuroscience* 8.
 111. Gray, J. A., K. Zito, and J. W. Hell. 2016. Non-ionotropic signaling by the NMDA receptor: controversy and opportunity. *Frontiers Research* 5.
 112. Nabavi, S., H. W. Kessels, S. Alfonso, J. Aow, R. Fox, and R. Malinow. 2013. Metabotropic NMDA receptor function is required for NMDA receptor-dependent long-term depression. *Proceedings of the National Academy of Sciences of the United States of America* 110: 4027-4032.
 113. Babiec, W. E., R. Guglietta, S. A. Jami, W. Morishita, R. C. Malenka, and T. J. O'Dell. 2014. Ionotropic NMDA receptor signaling is required for the induction of long-term depression in the mouse hippocampal CA1 region. *The Journal of neuroscience : the official journal of the Society for Neuroscience* 34: 5285-5290.
 114. Stein, I. S., J. A. Gray, and K. Zito. 2015. Non-Ionotropic NMDA Receptor Signaling Drives Activity-Induced Dendritic Spine Shrinkage. *The Journal of neuroscience : the official journal of the Society for Neuroscience* 35: 12303-12308.

115. Dore, K., J. Aow, and R. Malinow. 2015. Agonist binding to the NMDA receptor drives movement of its cytoplasmic domain without ion flow. *Proceedings of the National Academy of Sciences of the United States of America* 112: 14705-14710.
116. Stryer, L., and R. P. Haugland. 1967. Energy transfer: a spectroscopic ruler. *Proceedings of the National Academy of Sciences of the United States of America* 58: 719-726.
117. Stryer, L. 1978. Fluorescence energy transfer as a spectroscopic ruler. *Annual review of biochemistry* 47: 819-846.
118. Forster, T. 2012. Energy migration and fluorescence. 1946. *Journal of biomedical optics* 17: 011002.
119. Dolino, D. M., S. S. Ramaswamy, and V. Jayaraman. 2014. Luminescence Resonance Energy Transfer to Study Conformational Changes in Membrane Proteins Expressed in Mammalian Cells. e51895.
120. Roy, R., S. Hohng, and T. Ha. 2008. A practical guide to single-molecule FRET. *Nat Meth* 5: 507-516.
121. Kalinin, S., T. Peulen, S. Sindbert, P. J. Rothwell, S. Berger, T. Restle, R. S. Goody, H. Gohlke, and C. A. M. Seidel. 2012. A toolkit and benchmark study for FRET-restrained high-precision structural modeling. *Nat Meth* 9: 1218-1225.
122. Shaikh, S. A., D. M. Dolino, G. Lee, S. Chatterjee, D. M. MacLean, C. Flatebo, C. F. Landes, and V. Jayaraman. 2016. Stargazin Modulation of AMPA Receptors. *Cell reports* 17: 328-335.

123. Sisamakris, E., A. Valeri, S. Kalinin, P. J. Rothwell, and C. A. Seidel. 2010. Accurate single-molecule FRET studies using multiparameter fluorescence detection. *Methods Enzymol* 475: 455-514.
124. Armstrong, N., and E. Gouaux. 2000. Mechanisms for activation and antagonism of an AMPA-sensitive glutamate receptor: crystal structures of the GluR2 ligand binding core. *Neuron* 28: 165-181.
125. Ramanoudjame, G., M. Du, K. A. Mankiewicz, and V. Jayaraman. 2006. Allosteric mechanism in AMPA receptors: a FRET-based investigation of conformational changes. *Proceedings of the National Academy of Sciences of the United States of America* 103: 10473-10478.
126. Mankiewicz, K. A., A. Rambhadran, L. Wathen, and V. Jayaraman. 2008. Chemical interplay in the mechanism of partial agonist activation in alpha-amino-3-hydroxy-5-methyl-4-isoxazolepropionic acid receptors. *Biochemistry* 47: 398-404.
127. Gouaux, E. 2004. Structure and function of AMPA receptors. *The Journal of physiology* 554: 249-253.
128. Fenwick, M. K., and R. E. Oswald. 2008. NMR spectroscopy of the ligand-binding core of ionotropic glutamate receptor 2 bound to 5-substituted willardiine partial agonists. *Journal of molecular biology* 378: 673-685.
129. Maltsev, A. S., A. H. Ahmed, M. K. Fenwick, D. E. Jane, and R. E. Oswald. 2008. Mechanism of partial agonism at the GluR2 AMPA receptor: Measurements of lobe orientation in solution. *Biochemistry* 47: 10600-10610.

130. Ahmed, A. H., M. D. Thompson, M. K. Fenwick, B. Romero, A. P. Loh, D. E. Jane, H. Sondermann, and R. E. Oswald. 2009. Mechanisms of antagonism of the GluR2 AMPA receptor: structure and dynamics of the complex of two willardiine antagonists with the glutamate binding domain. *Biochemistry* 48: 3894-3903.
131. Ahmed, A. H., C. P. Ptak, M. K. Fenwick, C. L. Hsieh, G. A. Weiland, and R. E. Oswald. 2013. Dynamics of cleft closure of the GluA2 ligand-binding domain in the presence of full and partial agonists revealed by hydrogen-deuterium exchange. *The Journal of biological chemistry* 288: 27658-27666.
132. Landes, C. F., A. Rambhadran, J. N. Taylor, F. Salatan, and V. Jayaraman. 2011. Structural landscape of isolated agonist-binding domains from single AMPA receptors. *Nature chemical biology* 7: 168-173.
133. Ramaswamy, S., D. Cooper, N. Poddar, D. M. MacLean, A. Rambhadran, J. N. Taylor, H. Uhm, C. F. Landes, and V. Jayaraman. 2012. Role of conformational dynamics in alpha-amino-3-hydroxy-5-methylisoxazole-4-propionic acid (AMPA) receptor partial agonism. *The Journal of biological chemistry* 287: 43557-43564.
134. Hansen, K. B., N. Tajima, R. Risgaard, R. E. Perszyk, L. Jørgensen, K. M. Vance, K. K. Ogden, R. P. Clausen, H. Furukawa, and S. F. Traynelis. 2013. Structural Determinants of Agonist Efficacy at the Glutamate Binding Site of N-Methyl-d-Aspartate Receptors. *Molecular Pharmacology* 84: 114-127.
135. Yao, Y., J. Belcher, A. J. Berger, M. L. Mayer, and A. Y. Lau. 2013. Conformational analysis of NMDA receptor GluN1, GluN2, and GluN3 ligand-

- binding domains reveals subtype-specific characteristics. *Structure (London, England : 1993)* 21: 1788-1799.
136. Young, T. S., I. Ahmad, J. A. Yin, and P. G. Schultz. 2010. An enhanced system for unnatural amino acid mutagenesis in *E. coli*. *Journal of molecular biology* 395: 361-374.
 137. Nick Taylor, J., Q. Darugar, K. Kourentzi, R. C. Willson, and C. F. Landes. 2008. Dynamics of an anti-VEGF DNA aptamer: a single-molecule study. *Biochemical and biophysical research communications* 373: 213-218.
 138. Chen, P. E., M. T. Geballe, E. Katz, K. Erreger, M. R. Livesey, K. K. O'Toole, P. Le, C. J. Lee, J. P. Snyder, S. F. Traynelis, and D. J. Wyllie. 2008. Modulation of glycine potency in rat recombinant NMDA receptors containing chimeric NR2A/2D subunits expressed in *Xenopus laevis* oocytes. *The Journal of physiology* 586: 227-245.
 139. Kussius, C. L., and G. K. Popescu. 2009. Kinetic basis of partial agonism at NMDA receptors. *Nature neuroscience* 12: 1114-1120.
 140. Kalinin, S., S. Felekyan, M. Antonik, and C. A. Seidel. 2007. Probability distribution analysis of single-molecule fluorescence anisotropy and resonance energy transfer. *The journal of physical chemistry. B* 111: 10253-10262.
 141. Kalinin, S., A. Valeri, M. Antonik, S. Felekyan, and C. A. Seidel. 2010. Detection of structural dynamics by FRET: a photon distribution and fluorescence lifetime analysis of systems with multiple states. *The journal of physical chemistry. B* 114: 7983-7995.

142. Kalinin, S., E. Sisamakris, S. W. Magennis, S. Felekyan, and C. A. Seidel. 2010. On the origin of broadening of single-molecule FRET efficiency distributions beyond shot noise limits. *The journal of physical chemistry. B* 114: 6197-6206.
143. Sindbert, S., S. Kalinin, H. Nguyen, A. Kienzler, L. Clima, W. Bannwarth, B. Appel, S. Muller, and C. A. Seidel. 2011. Accurate distance determination of nucleic acids via Forster resonance energy transfer: implications of dye linker length and rigidity. *J Am Chem Soc* 133: 2463-2480.
144. Zhang, W., J. R. Howe, and G. K. Popescu. 2008. Distinct gating modes determine the biphasic relaxation of NMDA receptor currents. *Nature neuroscience* 11: 1373-1375.
145. Lape, R., D. Colquhoun, and L. G. Sivilotti. 2008. On the nature of partial agonism in the nicotinic receptor superfamily. *Nature* 454: 722-727.
146. Meyerson, J. R., J. Kumar, S. Chittori, P. Rao, J. Pierson, A. Bartesaghi, M. L. Mayer, and S. Subramaniam. 2014. Structural mechanism of glutamate receptor activation and desensitization. *Nature* 514: 328-334.
147. Popescu, G., A. Robert, J. R. Howe, and A. Auerbach. 2004. Reaction mechanism determines NMDA receptor response to repetitive stimulation. *Nature* 430: 790-793.
148. Banke, T. G., and S. F. Traynelis. 2003. Activation of NR1/NR2B NMDA receptors. *Nature neuroscience* 6: 144-152.
149. Romero-Hernandez, A., N. Simorowski, E. Karakas, and H. Furukawa. 2016. Molecular Basis for Subtype Specificity and High-Affinity Zinc Inhibition in the

- GluN1-GluN2A NMDA Receptor Amino-Terminal Domain. *Neuron* 92: 1324-1336.
150. Kim, J. Y., C. Kim, and N. K. Lee. 2015. Real-time submillisecond single-molecule FRET dynamics of freely diffusing molecules with liposome tethering. *Nature communications* 6: 6992.
 151. Amico-Ruvio, S. A., S. E. Murthy, T. P. Smith, and G. K. Popescu. 2011. Zinc effects on NMDA receptor gating kinetics. *Biophysical journal* 100: 1910-1918.
 152. Jain, A., R. Liu, B. Ramani, E. Arauz, Y. Ishitsuka, K. Ragunathan, J. Park, J. Chen, Y. K. Xiang, and T. Ha. 2011. Probing cellular protein complexes using single-molecule pull-down. *Nature* 473: 484-488.
 153. Shuang, B., D. Cooper, J. N. Taylor, L. Kisley, J. Chen, W. Wang, C. B. Li, T. Komatsuzaki, and C. F. Landes. 2014. Fast Step Transition and State Identification (STaSI) for Discrete Single-Molecule Data Analysis. *The journal of physical chemistry letters* 5: 3157-3161.
 154. Taylor, J. N., and C. F. Landes. 2011. Improved resolution of complex single-molecule FRET systems via wavelet shrinkage. *The journal of physical chemistry. B* 115: 1105-1114.
 155. Taylor, J. N., D. E. Makarov, and C. F. Landes. 2010. Denoising single-molecule FRET trajectories with wavelets and Bayesian inference. *Biophysical journal* 98: 164-173.
 156. Huettner, J. E., and B. P. Bean. 1988. Block of N-methyl-D-aspartate-activated current by the anticonvulsant MK-801: selective binding to open channels.

- Proceedings of the National Academy of Sciences of the United States of America*
85: 1307-1311.
157. Amico-Ruvio, S. A., M. A. Paganelli, J. M. Myers, and G. K. Popescu. 2012. Ifenprodil effects on GluN2B-containing glutamate receptors. *Mol Pharmacol* 82: 1074-1081.
 158. Mortensen, M., and T. G. Smart. 2007. Single-channel recording of ligand-gated ion channels. *Nat. Protocols* 2: 2826-2841.
 159. Wang, J., and P. Wolynes. 1996. Instantons and the Fluctuating Path Description of Reactions in Complex Environments. *The Journal of Physical Chemistry* 100: 1129-1136.
 160. Pirchi, M., G. Ziv, I. Riven, S. S. Cohen, N. Zohar, Y. Barak, and G. Haran. 2011. Single-molecule fluorescence spectroscopy maps the folding landscape of a large protein. *Nature communications* 2: 493.
 161. Lee, G., D. M. MacLean, H. Ulrich, X. Zhao, J. Aronowski, and V. Jayaraman. 2014. RNA based antagonist of NMDA receptors. *ACS chemical neuroscience* 5: 559-567.
 162. Regalado, M. P., A. Villarroel, and J. Lerma. 2001. Intersubunit cooperativity in the NMDA receptor. *Neuron* 32: 1085-1096.
 163. Dorr, J. M., S. Scheidelaar, M. C. Koorengel, J. J. Dominguez, M. Schafer, C. A. van Walree, and J. A. Killian. 2016. The styrene-maleic acid copolymer: a versatile tool in membrane research. *European biophysics journal : EBJ* 45: 3-21.
 164. Dorr, J. M., M. C. Koorengel, M. Schafer, A. V. Prokofyev, S. Scheidelaar, E. A. van der Crujisen, T. R. Dafforn, M. Baldus, and J. A. Killian. 2014. Detergent-

- free isolation, characterization, and functional reconstitution of a tetrameric K⁺ channel: the power of native nanodiscs. *Proceedings of the National Academy of Sciences of the United States of America* 111: 18607-18612.
165. Jamshad, M., J. Charlton, Y. P. Lin, S. J. Routledge, Z. Bawa, T. J. Knowles, M. Overduin, N. Dekker, T. R. Dafforn, R. M. Bill, D. R. Poyner, and M. Wheatley. 2015. G-protein coupled receptor solubilization and purification for biophysical analysis and functional studies, in the total absence of detergent. *Bioscience reports* 35.
 166. Prabudiansyah, I., I. Kusters, A. Caforio, and A. J. Driessen. 2015. Characterization of the annular lipid shell of the Sec translocon. *Biochimica et biophysica acta* 1848: 2050-2056.
 167. Paulin, S., M. Jamshad, T. R. Dafforn, J. Garcia-Lara, S. J. Foster, N. F. Galley, D. I. Roper, H. Rosado, and P. W. Taylor. 2014. Surfactant-free purification of membrane protein complexes from bacteria: application to the staphylococcal penicillin-binding protein complex PBP2/PBP2a. *Nanotechnology* 25: 285101.
 168. Broecker, J., B. T. Eger, and O. P. Ernst. 2017. Crystallogensis of Membrane Proteins Mediated by Polymer-Bounded Lipid Nanodiscs. *Structure (London, England : 1993)* 25: 384-392.
 169. Cooper, D., H. Uhm, L. J. Tauzin, N. Poddar, and C. F. Landes. 2013. Photobleaching lifetimes of cyanine fluorophores used for single-molecule Forster resonance energy transfer in the presence of various photoprotection systems. *Chembiochem : a European journal of chemical biology* 14: 1075-1080.

170. Darugar, Q., H. Kim, R. J. Gorelick, and C. Landes. 2008. Human T-cell lymphotropic virus type 1 nucleocapsid protein-induced structural changes in transactivation response DNA hairpin measured by single-molecule fluorescence resonance energy transfer. *Journal of virology* 82: 12164-12171.
171. Cai, Q., A. K. Kusnetzow, K. Hideg, E. A. Price, I. S. Haworth, and P. Z. Qin. 2007. Nanometer distance measurements in RNA using site-directed spin labeling. *Biophysical journal* 93: 2110-2117.
172. Muschielok, A., J. Andrecka, A. Jawhari, F. Bruckner, P. Cramer, and J. Michaelis. 2008. A nano-positioning system for macromolecular structural analysis. *Nature methods* 5: 965-971.
173. Kudryavtsev, V., M. Sikor, S. Kalinin, D. Mokranjac, C. A. Seidel, and D. C. Lamb. 2012. Combining MFD and PIE for accurate single-pair Forster resonance energy transfer measurements. *Chemphyschem : a European journal of chemical physics and physical chemistry* 13: 1060-1078.
174. Schaffer, J., A. Volkmer, C. Eggeling, V. Subramaniam, G. Striker, and C. A. M. Seidel. 1999. Identification of Single Molecules in Aqueous Solution by Time-Resolved Fluorescence Anisotropy. *The Journal of Physical Chemistry A* 103: 331-336.
175. Maus, M., M. Cotlet, J. Hofkens, T. Gensch, F. C. De Schryver, J. Schaffer, and C. A. M. Seidel. 2001. An Experimental Comparison of the Maximum Likelihood Estimation and Nonlinear Least-Squares Fluorescence Lifetime Analysis of Single Molecules. *Analytical Chemistry* 73: 2078-2086.

176. Woźniak, A. K., G. F. Schröder, H. Grubmüller, C. A. M. Seidel, and F. Oesterheld. 2008. Single-molecule FRET measures bends and kinks in DNA. *Proceedings of the National Academy of Sciences of the United States of America* 105: 18337-18342.
177. Dale, R. E., J. Eisinger, and W. E. Blumberg. 1979. The orientational freedom of molecular probes. The orientation factor in intramolecular energy transfer. *Biophysical journal* 26: 161-193.
178. Antonik, M., S. Felekyan, A. Gaiduk, and C. A. Seidel. 2006. Separating structural heterogeneities from stochastic variations in fluorescence resonance energy transfer distributions via photon distribution analysis. *The journal of physical chemistry. B* 110: 6970-6978.
179. Kalinin, S., S. Felekyan, A. Valeri, and C. A. M. Seidel. 2008. Characterizing Multiple Molecular States in Single-Molecule Multiparameter Fluorescence Detection by Probability Distribution Analysis. *The Journal of Physical Chemistry B* 112: 8361-8374.
180. MacLean, D. M., S. S. Ramaswamy, M. Du, J. R. Howe, and V. Jayaraman. 2014. Stargazin promotes closure of the AMPA receptor ligand-binding domain. *J Gen Physiol* 144: 503-512.

Vita

Drew Matthias Dolino was born in Houston, Texas on May 11, 1987, the son of Garvine Larrazabal Dolino and Woodrow Villarosa Dolino. After completing his work at Klein High School, Klein, Texas in 2005, he entered the University of St. Thomas in Houston, Texas. He received the degree of Bachelor of Science with a major in biochemistry from the University of St. Thomas in May, 2009. He spent the next two years, at UT Southwestern medical school as a medical student before realizing that his passions lay with basic science research. Then, in August 2012, he matriculated into The University of Texas MD Anderson Cancer Center UTHHealth Graduate School of Biomedical Sciences.

Permanent address:

16407 Augusta Ct.

Spring, Texas 77379